Collective quantum phenomena in the strong light - matter coupling regime

Vanik Shahnazaryan

Faculty of Physical Sciences
University of Iceland
2017

COLLECTIVE QUANTUM PHENOMENA IN THE STRONG LIGHT - MATTER COUPLING REGIME

Vanik Shahnazaryan

180 ECTS thesis submitted in partial fulfillment of a
PhD Scientiarum degree in Physics

Advisor
Ivan Shelykh

Faculty Representative
Oddur Ingólfsson

PhD committee
Viðar Guðmundsson
Snorri Ingvarsson

Opponents
Jerome Tignon
Alexander Poddubny

Faculty of Physical Sciences
School of Engineering and Natural Sciences
University of Iceland
Reykjavik, 10 2017

Collective quantum phenomena in the strong light - matter coupling regime
Collective quantum effects in the strongly coupled light-matter systems
180 ECTS thesis submitted in partial fulfillment of a PhD degree in Physics

Faculty of Physical Sciences
School of Engineering and Natural Sciences
University of Iceland
Dunhagi 3
IS-107, Reykjavik, Reykjavik
Iceland

Telephone: 525 4000

Bibliographic information:
Vanik Shahnazaryan, 2017, Collective quantum phenomena in the strong light - matter coupling regime, PhD thesis, Faculty of Physical Sciences, University of Iceland.

ISBN 978-9935-9320-2-0

Printing: Háskólaprent, Fálkagata 2, 107 Reykjavík
Reykjavik, Iceland, 10 2017

Abstract

The physics of light-matter interactions is a rapidly developing interdisciplinary research area, combining methods and phenomena both from condensed matter physics and quantum optics. One of the most common realizations of strong coupling regime implies an employment of various low-dimensional semiconductor structures i) embedded into a microcavity, ii) irradiated by a strong optical field. The latter leads to formation of hybrid quasiparticles — i) polaritons, ii) dressed states. In the current thesis we theoretically investigate various many body quantum effects in the mentioned systems, including

1) fluorescence spectra of an electromagnetically dressed asymmetric quantum dot;

2) terahertz lasing from an ensemble of asymmetric quantum dots in the presence of dressing electromagnetic field;

3) Bose-Einstein condensation of indirect excitons in a dipolariton setup;

4) interparticle interactions between excited excitonic states in quantum wells

5) interparticle interactions between excited excitonic states in transition metal dichalcogenide monolayers.

Útdráttur

Víxlverkun milli ljóss og efnis er ört vaxandi þverfræðilegt rannsóknarsvið sem sameinar aðferðir og fyrirbæri þéttefnifræðis og skammtaljósfræðis. Eitt algengasta fyrirkomulag kerfa til að öðlast sterka víxlverkun notfærir sér mismunandi hálfleiðarastrúktúra af lágum víddum sem annaðhvort i) eru settir inn í örholrými eða ii) eru settir í sterkt ljóssvið. Seinna fyrirkomulagið leiðir til myndum svokallaðra blandaðra einda, svo sem i) ljósskauteinda og ii) klæddra ástanda. Í þessari ritgerð eru mismunandi fjölhluta skammtaáhrif í fyrrnefndum kerfum skoðuð fræðilega en þau innihalda

1) flúrljómunarróf rafsegulklæddra ósamhverfra skammtapunkta

2) terariðsleysun frá samansafni ósamhverfra skammtapunkta í klæðningarsviði

3) Bose-Einstein þéttinga af óbeinum örveindum í uppsetningu tvíljósskauteinda,

4) víxlverkun milli örveinda í örvuðum ástöndum í skammtabrunnum

5) víxlverkun milli örveinda í örvuðum ástöndum í einföldum lögum af TMDC (e. transition metal dichalcogenides).

Аннотация

Физика взаимодействия излучения и вещества является быстро развивающейся междисциплинарной областью исследований, объединяющей методы и явления как физики конденсированных сред, так и квантовой оптики. Одной из наиболее распространенных реализаций режима сильной связи является использование различных низкоразмерных полупроводниковых структур a) встроенных в микрорезонатор, b) облученных сильным оптическим полем. Последнее ведет к формированию гибридных квазичастиц – a) поляритонов, b) одетых состояний. В рамках данной диссертации мы изучаем различные многочастичные явления в указанных системах, в том числе

1) спектр резонансной флуоресценции в асимметричной квантовой точке, одетой электромагнитным полем;

2) терагерцовое излучение из ансамбля асимметричных квантовых точек в присутствии одевающего электромагнитного поля;

3) Бозе-Эйнштейновская конденсация непрямых экситонов в диполяритонной системе;

4) межчастичные взаимодействия между возбужденными экситонными состояниями в квантовых ямах;

5) межчастичные взаимодействия между возбужденными экситонными со-

Acknowledgements

First of all, I would like to thank my academic supervisor Prof. Ivan Shelykh for the constant support, formulation of interesting scientific problems, stimulating discussions and sharing his deep understanding of physics. I highly appreciate all the knowledge and experience gained during my PhD studies.

The years I spent in Shelykh group were indeed unforgettable. It was a real pleasure to work next to my colleagues by the group. Particularly, I thank Skender Morina and Kevin Dini for faithful friendship, Helgi Sigurdsson, Ksenia Morina, Kristin Arnardottir, Kristinn Kristinsson, Alexandra Sheremet, Ivan Vrubel, Ivan Iorsh, Roman Polozkov, Dmitry Gulevich, Dmitry Yudin, Anastasiia Pervishko, Timothy Liew and Tania Espinosa-Ortega for all the teamwork and pleasant time spent together.

I would like especially thank Oleksandr Kyriienko (Niels Bohr Institute) for profound cooperation, careful advising, and non-standard way of thinking. I also express my gratitude to external scientific partners of our group Igor Chestnov (Vladimir State Univeristy), Prof. Oleg Kibis (Novosibirsk State Technical University), Prof. Gagik Kryuchkyan (Yerevan State University), Prof. Sergei Tarasenko (A. F. Ioffe Physico-Technical Institute), Prof. Alexander Alodjants (ITMO University), Vasil Saroka and Prof. Mikhail Portnoi (Univeristy of Exeter) for fruitful collaboration in various projects.

I am highly indebted to University of Iceland and all the staff for providing all necessary support for successful work. I am also grateful to ITMO University, Nanyang Technological University, and Niels Bohr Institute for hospitality. The time I spent in these institutions with my collaborators was very productive and pleasant at the same time.

I would like to gratefully acknowledge the financial support from the FP7 ITN NOTEDEV project for my PhD scholarship, and H2020 project CoExAn for funding the visits to collaborators.

Finally, I would like to thank my family for thorough support in all my beginnings.

Contents

1. Introduction

One of the rapidly developing areas of contemporary physics is the field of strong light-matter interactions - an interdisciplinary science, situated on the boundary of condensed matter physics and quantum optics. The reasons for this are various unique effects, appearing in the mentioned area, interesting from a pure scientific point of view, and simultaneously having a significant potential for applications in novel optoelectronic devices. The regime of strong light-matter coupling is achieved when the interaction rate between material subsystem and electromagnetic field exceeds all possible decay rates of the system. In this case the perturbative treatment of the irradiation impact on the system properties is non-reasonable and do not provide the proper understanding of the system. Instead, the correct treatment implies the consideration of matter-light system as a hybrid bound object. One efficient realization of the concept of strong light-matter coupling consists in embedding semiconductor structures of different dimensionality into a cavity, leading to resonant coupling between matter excitations and cavity eigenmode, resulting in appearance of hybrid quasiparticles. The latter, depending on whether the matter excitation is of bosonic or fermionic nature, is commonly referred as "polaritons" and "dressed states". The combination of properties inherited from their both counterparts, such as ultrasmall effective mass, strong interparticle interactions, and enhanced decoherence time, makes polaritons unique testbed for observation of various collective quantum phenomena, including Bose-Einstein Condensation (BEC), superfluidity, spin currents, optical spin Hall effect, quantum transport, etc.

The current thesis is devoted to the theoretical study of optical properties of semiconductor quantum wells and dots, being in the regime of strong light-matter coupling. In the *introductory chapter* the general description of the systems under consideration and the mathematical methods are presented. In particular, we provide a brief overview of size quantized semiconductor structures, focusing on excitonic states in quantum wells. Further, we describe the confinement of photonic mode in the cavity and the emergence of polaritonic states, as well as dipolaritons, appearing in double quantum well+microcavity system. In the end we present the theory of two-level quantum system irradiated by strong external electromagnetic field. We consider both semiclassical and full quantum approaches, and focus on the concept of dressed states, which provides relatively simple and accurate explanation of peculiarities of resonance fluorescence spectra from such a system.

Chapter 2 is devoted to the investigation of resonance fluorescence in two-level asym-

metric system, dressed into a bichromatic field. As a typical example we employ semiconductor quantum dot with giant piezoelectric effect, emerging from the properties of crystalline structure of wurtzite type. The presence of such an effect leads to the appearance of built-in dipole momentum aligned in the asymmetry axis direction. As a two-level system we consider the ground and excited states of size quantization, for which the dipole momentum appears to be inequivalent. We further consider the interaction of the described structure with a bichromatic dressing field, having near-resonant and far off-resonant components with different polarizations. The described configuration substantially modifies the spectrum of resonance fluorescence. In turns out, that in this case instead of conventional Mollow triplet it consists of infinite set of triplets, frequencies and amplitudes of which can be flexibly controlled tuning the characteristics of dressing field.

The efficient theoretical description of the above mentioned system requires the transition to the quasienergetic states (QES) representation. In the frameworks of QES representation we employ the density matrix formalism for two-level system to find the transition probabilities. Finally, the calculation of resonance fluorescence spectra is done by means of quantum regression theorem.

In the *third chapter* we consider the possibility of terahertz lasing based on the ensemble of asymmetric quantum dots in the presence of monochromatic dressing field. In this case the focus shifted to the level transitions between valence and conduction band, strongly coupled to dressing field. The presence of asymmetry opens the radiative transitions between neighboring dressed states, with typical frequency of terahertz range. The positive feedback is provided by embedding the system of quantum dots into a high Q-factor photonic crystal cavity.

The mathematical description of the presented phenomena involves a transition to the basis of dressed states. The collective dynamics is given by the master equation for density matrix, in the mean-field approximation leading to Maxwell-Bloch type equations for mode occupancies. However, besides conventional decoherence rates the effect strongly suffers from the presence of inhomogeneous broadening, rising from the inequivalence of quantum dots sizes. The correct inclusion of the impact of various defects in non-trivial task and requires numerical simulation of Langevin type stochastic equations.

Chapter 4 is devoted to the study of exciton Bose-Einstein condensation (BEC) in dipolariton system. While exciton condensation by direct optical addressing is still lacking due to technological obstacles, here we propose a scheme, consisting in separation of pump stage and condensation of excitons. The structure under consideration consists of two non-symmetric quantum wells, where the electron tunneling is allowed. Thus, at low temperatures the structure contains both direct and spatially indirect excitons, where electron and hole are in adjacent quantum wells. In this configuration the population rates between two constituents can be controlled by means of external electric field. Further the system is embedded into cavity, resonantly coupled to direct

exciton mode, leading to rice of three hybrid modes, referred as dipolaritons. The idea consists in an initial preparation of condensate of exciton-polaritons, which nowadays can be routinely obtained even by nonresonant pump, and consequent Landau-Zener type transition of coherent phase to the population of indirect exciton mode. The transition takes place due to reduction of indirect exciton energy by means of electric field. The mathematical description of the process can be done within the density matrix formalism.

In *chapter 5* the investigation of interparticle interactions of excited (Ryberg) excitonic states in quantum wells is presented. The latter represent themselves the solid-state analogues of Rydberg atoms. Unlike the ground state, Rydberg states are characterized by large spread of wave functions, strongly enhancing the interaction. While highly excited atomic systems were thoroughly investigated, the Rydberg excitonic states were lacking attention for a long time. The reason for this is the reduced addressability of such states, coming from the evidence that they are situated close to the conduction band, and therefore, for most of materials are experimentally indistinguishable. Luckily, recent advances in experimental techniques successfully solves this problem, and nowadays Rydberg excitonics is rapidly developing area of condensed matter physics.

The mathematical description consists in using the scattering theory formalism previously developed to describe the interaction of ground state excitons in quantum wells. We further sophisticate this theory to include the interaction of the excited states. The calculated interaction rates show quite unexpected behavior, in detail discussed in the corresponding section.

In *chapter 6* we apply the formalism of previous chapter to the transition-metal dichalcogenide monolayers. This novel materials attract a lot of attention due to the set of nontrivial properties, stemming from their lattice structure and unusual screening of interaction. In particular, from the point of view of excitonic applications they perfectly fit to the concept Rydberg states, since possess giant binding energy, making easily optically addressable wide range of excited states. The calculation of interactions unveiled significant differences with the case of interactions of conventional quantum well excitons, rising due to the effects of screening.

In the last chapter we present a brief summary of the thesis with concluding remarks, and outline the prospective for future applications of developed methods.

1.1. Low dimensional semiconductor structures

Semiconductors are class of materials the basic physical properties of which flexibly vary depending on external impacts. This evidence put semiconductors in the focus of scientific-technological revolution, created the basics of modern world. In particular, nowadays the whole industry of information storage and transfer devices is based on semiconducting materials. Sophistication of experimental techniques in 70-s allowed the creation of so called low-dimensional semiconductor structures, representing themselves systems, where the particle dynamics in one or more directions is confined in the area, linear size of which is comparable to the particle de Broglie wavelength. The latter effect, commonly referred as size quantization, opened the way to even more efficient control of physical properties of corresponding structures. Indeed, the effect of size quantization allows one to engineer semiconductor structures with predefined properties, such as particle wave function, energy spectrum and dipole momentum.

The physical realization of low dimensional structures consists in growth of semiconductor heterostructures, components of which differ from each other by the bandgap [1]. In the case when the structure is grown in the way that narrow gap semiconductor is between wide gap materials (so called sandwich structure), the band structure of described system plays a role of confinement potential for the electron in conduction band and hole in valence band (see Fig. 1.1). If the width of narrow gap material is of order of nm, that is, comparable to the radius of conduction electron, the motion of electron in the direction of heterostructure growth axis becomes quantized. Depending on the needs of the specific task altering the growth parameters and conditions it is possible to obtain size-quantized structures of different geometry, where the size quantization takes place in one or more directions. In particular, depending on dimensionality, they are commonly classified as quantum wells or films (quantization in one direction, effectively two dimensional structure), quantum wires (quantization in two directions, effectively one dimensional structure), and quantum dots (quantization in three directions, effectively zero dimensional structure). In the frameworks of current PhD thesis there are discussed various effects, taking place in quantum dots and wells. Below we present the description of excitonic states in quantum well. The

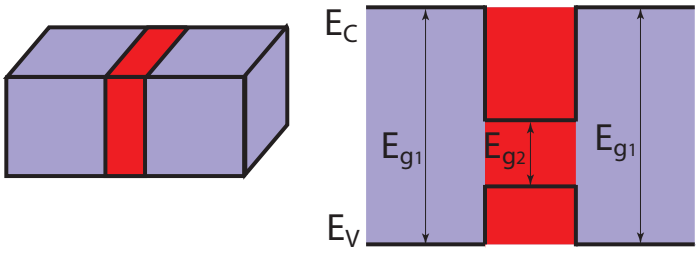

Figure 1.1: The sketch of semiconductor heterostructure.

quantum dot in the context of the thesis plays a role of effective two-level quantum system, suitable for obtaining strong-light matter interaction, that is why we shifted its discussion to the corresponding section.

1.1.1. Excitons in quantum wells: Rydberg states

One of the most important characteristics of semiconductor materials is absorbance spectrum of electromagnetic waves. The analysis of absorption spectra allows to unveil the information about band structure of the material, as well as to estimate the quality of particular sample (the presence of impurities, defects, etc.). At room temperature range for the majority of semiconducting materials the absorption spectrum is governed by interband transitions, where the electron goes from the valence band to the conduction band. However, at low temperature limit (of order of a few Kelvins) the dominant contribution to the spectrum is given by excitons — bound electron - hole pairs (see Fig. 1.2 (a)). The formation of excitons takes place in the case when the kinetic energy of free charge carriers (i. e., conduction electrons and holes) is lower than the energy of Coulomb attraction within them. Thus, excitons represent themselves solid-state analogues of hydrogen atom. One can distinguish excitons of small radius, where the exciton radius is smaller than lattice constant (Frenkel exciton), and excitons of large radius (Wannier-Mott excitons). In typical direct gap semiconductors the latter are formed, that is why in the following we will restrict ourselves by description of Wannier-Mott excitons.

Continuing the analogy with hydrogen atom it is important to note, that exciton internal dynamics is fully quantized and represented by hydrogen type wave functions. It means that the excitonic state is fully defined by set of quantum numbers $|nlm\rangle$ (for the bulk exciton) denoting the principal, orbital, and magnetic quantum numbers. In the frameworks of atomic physics in the last decades the highly excited states were attracting a lot of interest [2]. The reason for this in their various notable properties, such as long lifetime, enhanced dipole-dipole interactions, significant response to external fields, coming from the spatial widespread of the wave function. In particular, Rydberg atomic states with quantum number of order of $n = 1000$ and having cm size were experimentally reached.

Although acknowledging the existence of higher excitonic states, for a long period the main research interest in the field was restricted by lower states. The latter explained by the energy structure of excitonic states, obeying Rydberg rule. In typical semiconductors (GaAs, AlGaAs) the binding energy of exciton is about 10 - 20 meV, and decreases rapidly with the excitation. In particular, the energy of first excited state is smaller 4 times (9 times in the two dimensional case). Thus, the energy of excited states is less than meV, which means that these states are actually merged with the conduction band, and therefore, cannot be observed in experiments. The latter is best illustrated in absorption spectra scheme, shown in Fig. 1.2 (b). One can

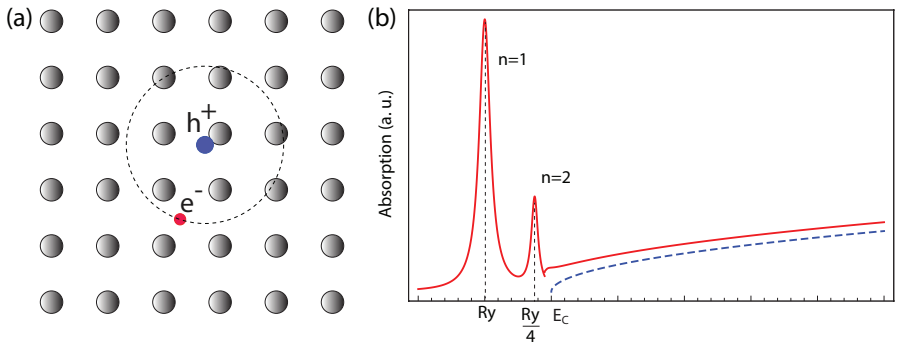

Figure 1.2: (a) Exciton state in semiconductor crystal. (b) The absorption scheme of typical semiconductor with exciton transitions (red solid line), and without (blue dashed line).

see, that only lower excitonic peaks are visible in absorption spectra.

However, very recently the situation changed dramatically. Advances in spectroscopic experimental techniques allowed the observation of exciton peaks with quantum number up to $n = 25$. The latter was reported in breakthrough paper by Kazimierczuk et. al. [3], giving rice to the intense investigations in physics of Rydberg excitons [4, 5, 6, 7]. As an experimental material copper dioxide (Cu_2O) was used, having Rydberg energy of about 100 meV. Here the optical excitation of s-type excitons is prohibited, due to the same parity of the lowest conduction and topmost valence bands, while the p-type excitons are dipole-allowed. The corresponding experimental results, are depicted on Fig. 1.3. Among the notable properties of observed states it should be noted extra large size. For instance, the calculation show $\langle r_{25} \rangle = 1.02\mu$m and the energy $E_{25} = 0.07$ meV, as it follows from the Fig. 1.3. Further, the detailed excitation power dependent spectroscopic analysis of the absorption let the authors of the paper conclude the existence of so called Coulomb blockade effect for highly excited states. The latter manifests itself in the reduction of exciton peak strength with the increase of excitation power (see Fig. 1.4). The observed phenomena believed to be explained by enhanced dipole-dipole interactions, prohibiting the excitation of new particles in the volume of their action.

The observed results motivated us to perform theoretical analysis of interactions between excited exciton states. However, we choose to model exciton interactions in two dimensional systems, since they better fit for obtaining strong light matter coupling regime (see subsequent sections). Proceeding with mathematical description of two dimensional excited excitonic states one should take into account the presence of size quantization in the growth axis direction in the case of quantum well.

$$\hat{H}_{exc} = -\frac{\hbar^2(k_{e||}^2 + k_{ez}^2)}{2m_e} - \frac{\hbar^2(k_{h||}^2 + k_{hz}^2)}{2m_h} - \frac{e^2}{4\pi\varepsilon_0\varepsilon|\vec{\rho}_e - \vec{\rho}_h|} + U(z_e) + U(z_h), \quad (1.1)$$

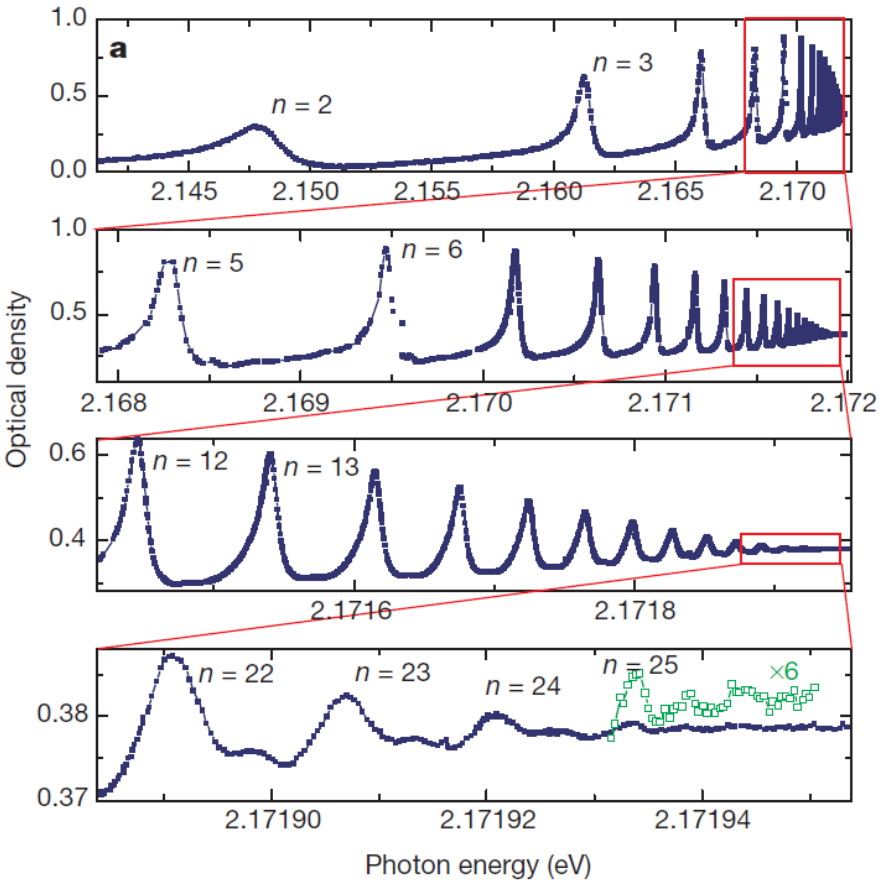

Figure 1.3: Exciton absorption spectra in bulk Cu_2O. Adapted from Ref. [3].

where the first two terms describe the kinetic energies of electron and hole, the third one correspond to Coulomb interaction, and last two terms denote the confinement potential for electron and hole. We note that in the limit of narrow quantum well (strong size quantization) the motions of electron and hole in z direction are quantized independently. Additionally, in the mentioned limit in the Coulomb term the contribution of motion in growth direction can be neglected, that is why in the Hamiltonian (1.2) $\rho_{e(h)}$ denotes the in-plane coordinate of electron (hole). Turning now the in-plane center of mass and relative coordinates $\vec{\rho} = \vec{\rho}_e - \vec{\rho}_h$, $\vec{R} = (m_e\vec{\rho}_e + m_h\vec{\rho}_h)/(m_e + m_h)$, one may rewrite

$$\hat{H}_{exc} = -\frac{\hbar^2\Delta_R}{2M} - \frac{\hbar^2\Delta_\rho}{2\mu} - \frac{e^2}{4\pi\varepsilon_0\varepsilon|\vec{\rho}|} - \frac{\hbar^2 k_{ez}^2}{2m_e} - \frac{\hbar^2 k_{hz}^2}{2m_h} + U(z_e) + U(z_h), \qquad (1.2)$$

where the first term corresponds to the exciton center of mass dynamics, second and

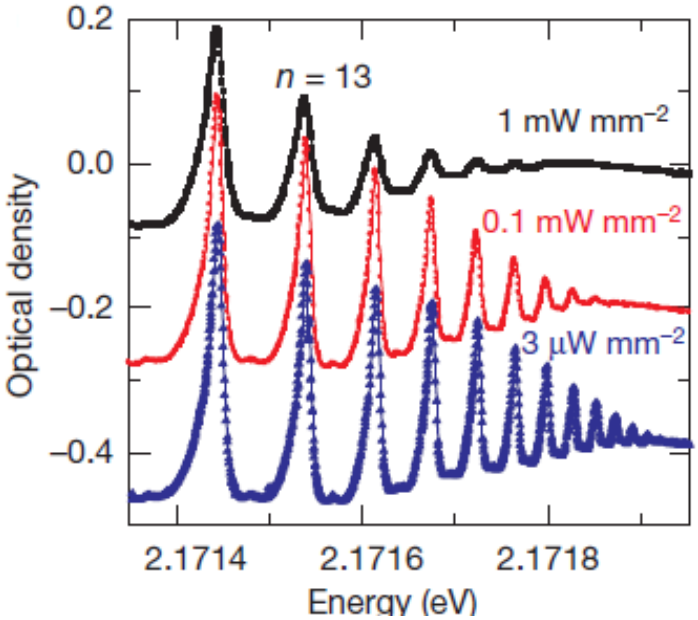

Figure 1.4: Excitation dependent Rydberg exciton absorption spectra in bulk Cu_2O. Adapted from Ref. [3].

third terms describe the internal dynamics, and the remaining terms stand for the dynamics of electron and hole in the quantum well growth direction. Correspondingly one can perform factorization of the wave function to the form

$$\Phi_{\vec{Q},n,m}(\vec{R},\rho,z_e,z_h) = \frac{1}{\sqrt{A}} e^{i\vec{Q}\vec{R}} \psi_{n,m}(\rho)\chi(z_e)\chi(z_h), \tag{1.3}$$

where the first factor denotes the free motion of exciton as a whole, and $\psi_{n,m}(\rho)$ corresponds to exciton internal dynamics. The wave functions of electron and hole in the z direction are defined by the shape of confinement potential, which typically modeled in the form of rectangular quantum well or quadratic potential. Thus, the problem of internal dynamics of quantum well exciton is equivalent to the two-dimensional Coulomb problem in the medium, having dielectric permittivity ε. The wave function of such a problem has a form [8]

$$\begin{aligned}\psi_{n,m}(\rho) =& \frac{1}{\sqrt{2}\lambda_{2\mathrm{D}}} \sqrt{\frac{(n-|m|-1)!}{(n-1/2)^3(n+|m|-1)!}} \left(\frac{\rho}{(n-1/2)\lambda_{2\mathrm{D}}}\right)^{|m|} \\ & \exp\left[-\frac{\rho}{(2n-1)\lambda_{2\mathrm{D}}}\right] L^{2|m|}_{n-|m|-1}\left[\frac{\rho}{(n-1/2)\lambda_{2\mathrm{D}}}\right] \frac{1}{\sqrt{2\pi}} e^{im\varphi},\end{aligned} \tag{1.4}$$

where L denotes associated Laguerre polynomial, and $\lambda_{2D} = 4\pi\varepsilon_0\varepsilon\frac{\hbar^2}{2\mu e^2}$ is the two-

dimensional Bohr radius. Corresponding energy levels read as

$$E_n = -\frac{1}{(4\pi\varepsilon_0\varepsilon)^2}\frac{\mu e^4}{2\hbar^2(n-1/2)^2} = -\frac{1}{4\pi\varepsilon_0\varepsilon}\frac{e^2}{4\lambda_{2D}(n-1/2)^2}, \qquad n = 1, 2, 3, \cdots \tag{1.5}$$

The above described formalism, in fact, represents itself a bosonisation procedure. Indeed, we turned form the dynamics of two interacting fermionic particles to a single bosonic particle, having some internal structure and performing free motion in the quantum well plane. Such transformation is physically correct only in the case of low concentrations of excited electron - hole pairs, which should be below critical value, referred as Mott density. Thus the validity of application of exciton formalism is given by the condition

$$n\lambda_{2D}^2 \ll 1, \tag{1.6}$$

where n is the exciton concentration. It should be noted that for higher excited states the two-dimensional Bohr radius should be replaced by the corresponding state radius $\rho_n = \int \rho|\psi_{n,m}(\rho)|^2 dS$, with $dS = \rho d\rho d\varphi$ denoting the elementary area.

In the frameworks of the current thesis we study the interactions between excited excitons. It should be noted, that there are variety of approaches addressing the study of interaction between ground state excitons [9, 10, 11, 12, 13]. Here we will follow to the earlier developed approach, considering the interaction as two body Coulomb scattering process, accounting for four possible scattering channels, including direct interaction and exchange terms [14]. Whithin this approach it was shown, that the interaction is governed by the exchange terms, which can be accurately estimated as [15]:

$$V_{XX} \approx \frac{6E_b\lambda_{2D}^2}{A}, \tag{1.7}$$

where A denotes the area of the sample. Here we will check whether similar formula is eligible for the description of interaction of excited excitons both in quantum wells and novel transition - metal dichalcogenide monolayers, discussed in the corresponding chapters.

1.2. Strong light matter coupling in semiconductor nanostructures

The quantitative boundary of the establishment of strong coupling regime is the condition of light matter interaction constant to overcome all the decay rates present in the system under consideration. In the frameworks of current thesis we will deal with two efficient realizations of strong light-matter interaction concept. The first one implies the coupling of matter system with electromagnetic field confined in the microcavity.

In the second case the regime of strong coupling emerges between the low-dimensional semiconductor structure and external resonant or near-resonant laser field. Consider these cases separately.

1.2.1. Microcavities

Microcavity represents itself micrometer size resonator of typically optical frequency range. One common mechanism of light confinement in microcavities is based on the use of periodic structure calibrated on some fixed wavelength (say, cavity eigenmode). Striking examples of such structures are the distributed Bragg reflectors (DBRs), consisting of altering semiconductor layers of nm thickness, having different refractive indexes. Such a structure provides high reflectivity, leading to proper confinement of cavity eigenmode. Typical planar microcavity consist of two DBRs and active medium (represented by low-dimenisonal semiconductor structure) in between them, placed in the position of the highest density of electromagnetic field (see Fig. 1.5.

There are several physical quantities, characterizing microcavity. First of all, for the confinement of specific frequency mode the condition of standing wave should be satisfied:

$$L = N\frac{\lambda_N}{2}, \tag{1.8}$$

with L denoting the cavity optical length and λ_N corresponding to the N-th eigenmode wavelength. As it follows from the eq. (1.8), the cavity can have several eigenmodes. However we will limit the consideration with the cases when only a single mode is relevant. The condition of validity of such an assumption is given below.

Another important quantity characterizing an optical mode of a cavity is a linewidth Γ, defined as the frequency width at half maximum (FWHM). The latter can be explained in the following way. In typical spectroscopic experiments the spectral peaks have a shape of Lorentzian broadening, instead of being delta-function type peak. The reason of this consists in decoherence processes, corresponding to radiative losses of the electromagnetic field to the outside media. Linewidth is the quantity characterizing the decay rate.

The presence of broadening allows one to introduce a quality factor of a cavity Q, describing the average number of oscillations made by cavity photon before leaving the cavity. The quality factor defined as

$$Q = \frac{\omega_c}{2\pi\Gamma}, \tag{1.9}$$

where ω_c defines the resonant angular frequency of a cavity. Another characteristic microcavity quantity closely related to the mode linewidth is the cavity photon lifetime, defined as

$$\tau = \frac{1}{2\pi\Gamma}. \tag{1.10}$$

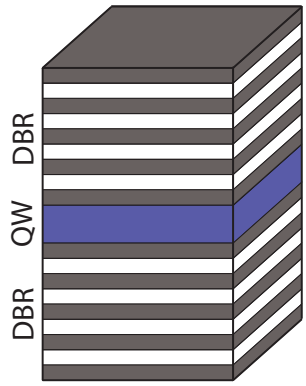

Figure 1.5: The sketch of planar microcavity, consisting of pair of DBRs with embedded quantum well.

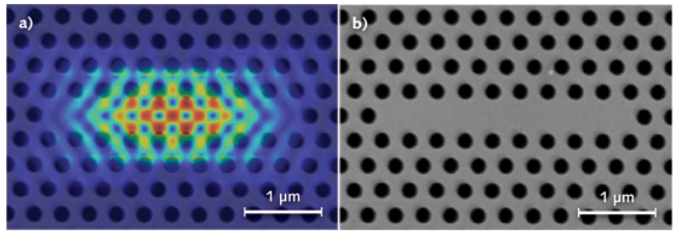

Figure 1.6: Photonic crystal cavity. (a) Calculation of the electric field distribution $|E|^2$; (b) Scanning electron microscopy image.

After introduction of the linewidth one can onset the condition on the above assumption, implying the consideration of microcavity as a single mode resonator. For this purpose we introduce the quantity called "finesse ov the cavity":

$$F = \frac{\Delta\omega}{2\pi\Gamma}. \tag{1.11}$$

The microcavity can be treated as a single mode resonator in the case when the separation between the neighboring modes exceed the linewidth (that is, $F >> 1$), ensuring that spectral lines are well-resolved. It should be mentioned, that this condition is easilly fulfilled simply reducing the cavity size, while the achiviement of high Q-factor is more challenging.

Proceeding with the description of planar microcavities one should stress the attention to the fact, that in such structures the electromagnetic field is confined only in the growth direction, while being able to propagate in other two. This circumstance leads to an interesting structure of energy spectrum, best described by the introduction of

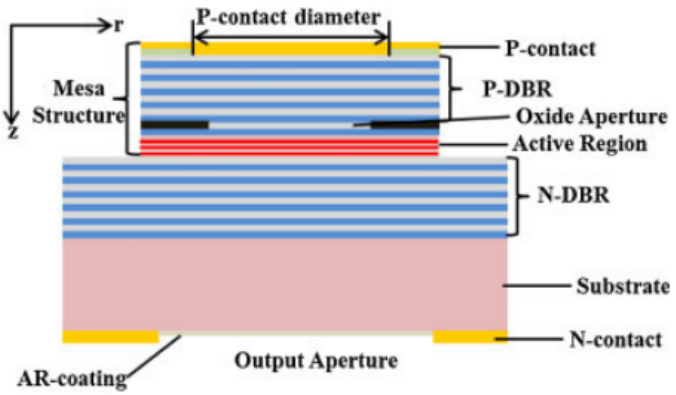

Figure 1.7: Sketch of VCSEL structure from Ref. [16].

photon effective mass. In particular, one has

$$E_C(k) = \frac{\hbar c}{n}\sqrt{\left(\frac{2\pi}{\lambda}\right)^2 + k^2} \approx \frac{2\pi\hbar c}{n\lambda} + \frac{\lambda c}{2\pi\hbar n}\frac{\hbar^2 k^2}{2} = E_C(0) + \frac{\hbar^2 k^2}{2m_C}, \tag{1.12}$$

where $k = \sqrt{k_x^2 + k_y^2}$ denotes the in-plane wave vector, and

$$n = \frac{\int_0^L n(z)E^2(z)\mathrm{d}z}{\int_0^L E^2(z)\mathrm{d}z} \tag{1.13}$$

is the effective refractive index, with $E(z)$ denoting the amplitude of electric field. The first term in eq. (1.12) corresponds to the cavity resonant energy, while the second term describes the contribution of in-plane propagation.

The semiconductor structures consisting of microcavity and size-quantized electronic system forms physical basis for novel generation optoelectronic devices. By constituent choice of cavity geometry, material and structure one can obtain confinement of modes with predefined frequency and polarization. The latter opens horizons for development of photonic devices such as light emitting diodes and bosonic lasers. In addition to the practical applications, various physical phenomena appearing in microcavities represent significant scientific interest. Namely, the description of interaction of cavity mode with embedded active media is given within the cavity quantum electrodynamics (CQED). It should be noted, that the observation of various collective quantum effects, such as condensation, superfluidity, spin transport, etc., requires the fabrication of high-Q microcavities, which is a challenging task, since in the conventional setups the quality decreases when decreasing the cavity size. In the last decades there

were proposed variety of microcavities of different shape and construction. However, DBR-based cavities remain the most common when speaking about cavities with two dimensional active media.

With this respect in worth noting the existence of conceptually different type of cavity, based on photonic crystals (see Fig. 1.6). The latter can act both in terahertz and optical ranges. The mode confinement effect here obtained by spoiling the periodicity, and placing instead active element, typically represented by single quantum dot or an ensemble of dots. Within the current thesis we will consider the latter case.

Among the microcavity-based devices here we would like outline so called VCSEL — Vertical Cavity Surface Emitting Laser. The structure consist of doped quantum well, providing the populating inversion, embedded into cavity, consisting of DBRs (Fig 1.7). Nowadays it is a commercialized product finding applications in large range of technological and scientific areas. VCSEL typically operates typically in the "weak coupling regime", where the decay rates of photonic mode and excitations of active media overcome the light-matter coupling strength. At the same time such structures provide the basis for achievement of strong coupling regime, discussed in the following section.

1.2.2. Cavity exciton-polaritons

While early theoretical predictions of possibility to obtain strong light-matter coupling regime on the basis of excitons were done in mid fifties [17, 18, 19], the experimental realization of this concept took a decades. The successful experimental observation of hybrid exciton - photon objects was done in 1992 in low dimensional semiconductor structure, consisting of DBR - microcavity with embedded quantum wells [20].

The two-dimensional excitons, confined in quantum well, interact with cavity photons, which are trapped between two DBRs. By consequent choice of structure geometrical parameters one can tune cavity eigenmode to be resonant with QW excitonic transition energy, making possible the achievement of the strong coupling regime. The emerging hybrid-particle, referred as exciton - polariton (polariton hereafter), have a half-light half matter nature. Polariton manifests itself in emission spectra, which is no longer represented by bare photon and exciton peaks.

The mathematical description of polariton states can be done semiclassically, based on the calculation of exciton optical dielectric function response [22]. However there is a relatively simple Hamiltonian model, based on a two coupled oscillators, which successfully describes the rise of polariton eigenstates. In secondary quantization formalism one can write

$$H = \sum_{\mathbf{k}} E_C(\mathbf{k}) a^\dagger_{\mathbf{k}} a_{\mathbf{k}} + \sum_{\mathbf{k}} E_X(\mathbf{k}) b^\dagger_{\mathbf{k}} b_{\mathbf{k}} + \sum_{\mathbf{k}} \frac{V_R(\mathbf{k})}{2} \left(a^\dagger_{\mathbf{k}} b_{\mathbf{k}} + a_{\mathbf{k}} b^\dagger_{\mathbf{k}} \right), \tag{1.14}$$

where the operators $a^\dagger_{\mathbf{k}}, a_{\mathbf{k}}, b^\dagger_{\mathbf{k}}, b_{\mathbf{k}}$, are creation and annihilation operators for photons and excitons with in-plane momenta $\mathbf{k}$, respectively. We suppose that condition (1.6) is satisfied, and both excitonic and photonic operators obey the rules of bosonic algebra. The first and second terms correspond to the bare photons and excitons , with $E_C(\mathbf{k})$ given by eq. (1.12), and $E_X(\mathbf{k})$ denoting the exciton dispersion in effective mass approximation:

$$E_X(k) = E_X(0) + \frac{\hbar^2 k^2}{2m_X}, \tag{1.15}$$

where m_X is the exciton mass. Here it is important to outline that typical effective mass a photon is extremely small and is of order of $10^{-4} - 10^{-5}$ of the free electron mass m_0, while the effective mass of an exciton is of order of m_0. Consequently, for the positive values of the detuning parameter $\Delta = E_X(0) - E_C(0)$ there is a certain momentum value $k_{cr} = \sqrt{2\Delta m_X m_C/\hbar^2(m_X - m_C)}$, where the dispersion curves of bare excitons and photons cross each other. In the case of negative detuning the photon energy lies higher everywhere in momentum space.

The last term in (1.14) corresponds to the light-matter interaction which is governed by the exciton-photon coupling constant $V_R/2$. The latter is defined as:

$$V_R(k) = \frac{d_{cv}}{2\pi a_B^{2D}} \sqrt{\frac{E_X(k)}{n\lambda}}, \tag{1.16}$$

where d_{cv} is the dipole matrix element of interband transition and determined by the material parameters. It should be mentioned that the coupling rate $V_R(k)$ is a weak function of momentum at small in-plane polariton momenta $k \ll k_z$, since E_X is almost constant in that region.

The Hamiltonian (1.14) can be rewritten in diagonal form by the following linear transformation of the operators [21]

$$p_{L,\mathbf{k}} = C_{L,\mathbf{k}} a_{\mathbf{k}} + X_{L,\mathbf{k}} b_{\mathbf{k}}, \tag{1.17}$$

$$p_{U,\mathbf{k}} = C_{U,\mathbf{k}} a_{\mathbf{k}} + X_{U,\mathbf{k}} b_{\mathbf{k}}. \tag{1.18}$$

In new operators the Hamiltonian reads as

$$H = \sum_{\mathbf{k}} E_L(\mathbf{k}) p^\dagger_{L,\mathbf{k}} p_{L,\mathbf{k}} + \sum_{\mathbf{k}} E_U(\mathbf{k}) p^\dagger_{U,\mathbf{k}} p_{U,\mathbf{k}}, \tag{1.19}$$

where

$$E_{U,L}(k) = \frac{E_C(k) + E_X(k)}{2} \pm \frac{1}{2}\sqrt{(E_C(k) - E_X(k))^2 + V_R^2}, \tag{1.20}$$

are the energies of the upper and lower polariton branches, respectively. Thus, operators (1.17) and (1.18) correspond to the upper and lower polariton — new eigenmodes of the coupled QW-cavity system. The coefficients $C_{U,L}$, $X_{U,L}$ in expressions (1.17),

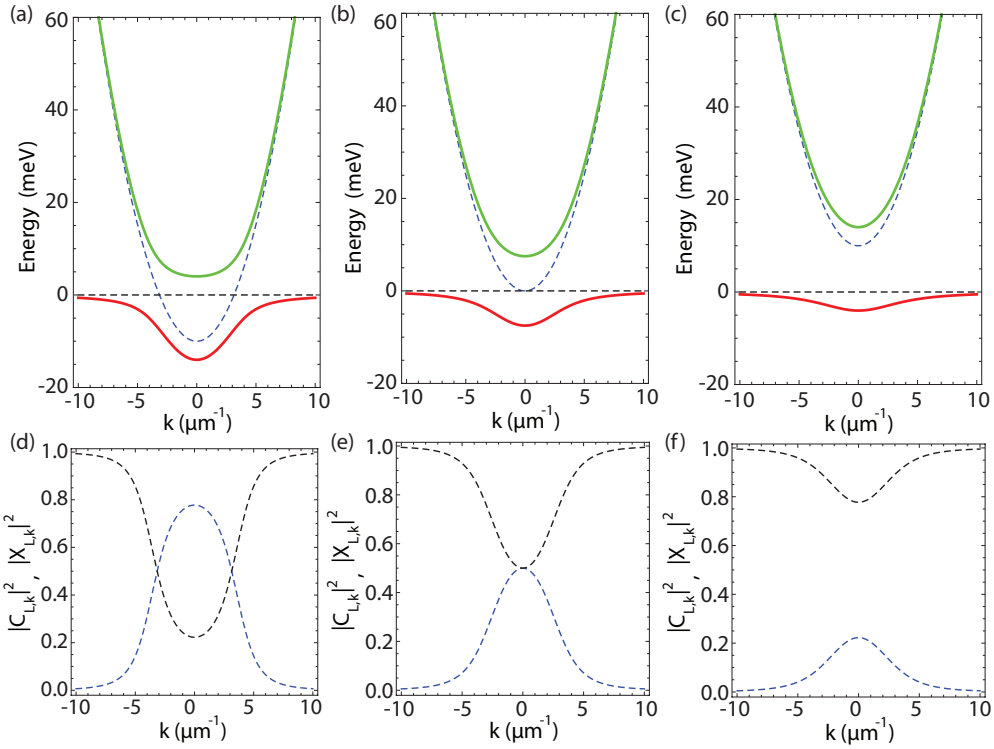

Figure 1.8: The dispersion of upper and lower polariton modes (green and red solid lines) plotted for the detuning values a) $\Delta = 10meV$; b) $\Delta = 0meV$; c) $\Delta = -10meV$. The interaction constant was chosen to be $V_R = 15$ meV. The bare exciton and photon modes are shown by black and blue dashed lines, respectively. Panels (d)-(f) depict the photonic (blue line) and excitonic (black line) fractions of lower polariton branch for corresponding value of detuning.

(1.18) describe the fractions of bare exciton and photon mode fractions in the polariton branches, and calculated as

$$C_{L,\mathbf{k}} = -X_{U,\mathbf{k}} = \frac{1}{\sqrt{2}}\sqrt{1 - \frac{E_X(\mathbf{k}) - E_C(\mathbf{k})}{\sqrt{V_R^2 + (E_X(\mathbf{k}) - E_C(\mathbf{k}))^2}}}, \tag{1.21}$$

$$X_{L,\mathbf{k}} = C_{U,\mathbf{k}} = \frac{1}{\sqrt{2}}\sqrt{1 + \frac{E_X(\mathbf{k}) - E_C(\mathbf{k})}{\sqrt{V_R^2 + (E_X(\mathbf{k}) - E_C(\mathbf{k}))^2}}}. \tag{1.22}$$

The Fig. 1.8 shows the polariton dispersion curves for different detuning values. As it follows from the panel (a), for the case of positive detuning so called effect of anticrossing takes place. The essence of the anticrossing is that in contrast to the energies of the bare modes, the energies of polariton brances are splitted by the Rabi interaction energy V_R for the momentum value k_{cr}. On the panel (d) we depicted the squares of Hopfield coefficients, showing the fractions of bare modes on lower polariton branch. As it seen, in the case of configuration with positive detuning near the vicinity of momentum minima the lower polariton branch is almost purely photonic. And instead, adter the inflection point k_{cr} it becomes mostly excitonic. In the opposite limiting case, corresponding to strongly negative detuning (panels (c) and (f)) there is a weaker mixing between the modes, and for all the values (expect with small area near the momentum minima) the lower polariton branch is predominantly excitonic.

It should be noted that in real structures one should account for finite lifetimes of excitons and photons. It means that their energy spectrum conatins additional imaginary terms $-i\gamma_{X,C}$. In this case the expressions of polariton eigenmodes (1.20) become complex as well. Their real parts correspond to dispersions of polariton modes, while imaginary parts give polariton spectral lines homogeneous broadenings. The Rabi splitting in this case is determined as a distance between the real parts of the polariton states and in the anti-crossing point has a form

$$\hbar\Omega_R = \begin{cases} \sqrt{V_R^2 - (\gamma_X - \gamma_C)^2}, & V_R^2 > (\gamma_X - \gamma_C)^2 \\ 0, & V_R^2 < (\gamma_X - \gamma_C)^2 \end{cases} \tag{1.23}$$

Thus, the strong coupling regime can be maintained when the exciton and photon damping rates are lower than the coupling rate.

Microcavity with embedded quantum wells operating in strong coupling regime represents itself perfect testbed for observation of various collective quantum phenomena and serves as physical basis for novel generation optoelectronic devices at the same time [23]. Namely, the bosonic nature of polaritons, along with extermely small mass provided by photonic counterpart and strong interparticle scatterings, coming from excitonic fraction, makes possible the experimental achievement of Bose-Einstein condensation of polaritons [24, 25] and onset of superfluidity [26, 27]. Moreover, the use of wide gap materials (GaN and ZnO) allowed to shift the condensation temperature to the room temperature limit, where the lasing was demonstrated [28, 29, 30].

It also worth mentioning the presence of effective magnetic fields, provided by the longitudinal-transverse (LT) splitting of photonic mode and spin-orbit interaction for excitonic counterpart. The combined impact of these effective fields, together with the influence of external magnetic field, lead to a variety of spin effects, including optical spin Hall effect [31], skyrmion formation [32], field-tunable spin patterns [33], rise of spin currents [A7], etc.

1.2.3. Dipolaritons

In the introductory section 1.1.1 we have discussed the two-dimensional excitonic states, where both electron and hole were confined in single quantum well. However, along with the mentioned case the systems of coupled quantum wells attract considerable scientific interest. Exciton in this case consists of electron and hole localized in different wells [34, 35], and typically referred as spatially indirect excitons [36]. The reduced overlap between electron and hole wave functions leads to lifetime of order of nanoseconds, which is much larger than for spatially direct excitons. This circumstance makes it possible the cooling down to lattice temperature [37, 38, 39], which is why they are frequently referred to as cold excitons [40]. One different consequence of electron hole spatial separation is their large dipole momentum, oriented along the structure growth axis, leading to strong interexciton interactions.

The mentioned peculiarities make indirect excitons promising candidates for observation of various phenomena in the domain of strong light-matter coupling physics. In particular, it was shown that the combination of exciton polaritons and spatially indirect excitons may lead to several promiment results [41, 42]. Namely, embedding coupled quantum wells into microcavity leads to rise of new hybrid eigenmodes, named dipolaritons. They represent themselves superposition of cavity photons (C) and spatially direct (DX) and indirect (IX) excitons. The considered structure consists of two quantum wells of different width, separated by thin barrier (see Fig. 1.9). The size of barrier is chosen in a way to forbid the tunneling of hole and allowing the tunneling of electron. Thus, the hole in this configuration is localized in wider quantum well (since it has lower size quantization energy), while electron wave function is distributed between the wells. The cavity is tuned to be near resonant with wider quantum well, while the narrow one remains decoupled from the optical mode. Thus, the hybridization of the modes leads to the formation of three dipolariton modes: upper (UP), middle (MP) and lower (LP). The term "dipolariton" highlights the nature of particles, which are exciton polaritons possessing large dipole momentum, and mixing with indirect exciton will give rise to dipolaritons. It should be noted, that the external electric field can tune the energy of indirect exciton mode, thus making possible the control of bare mode partitions in dipolariton branches.

The system can be effectively described by three coupled oscillators Hamiltonian model, which is in perfect agreement with the results experimental measurements

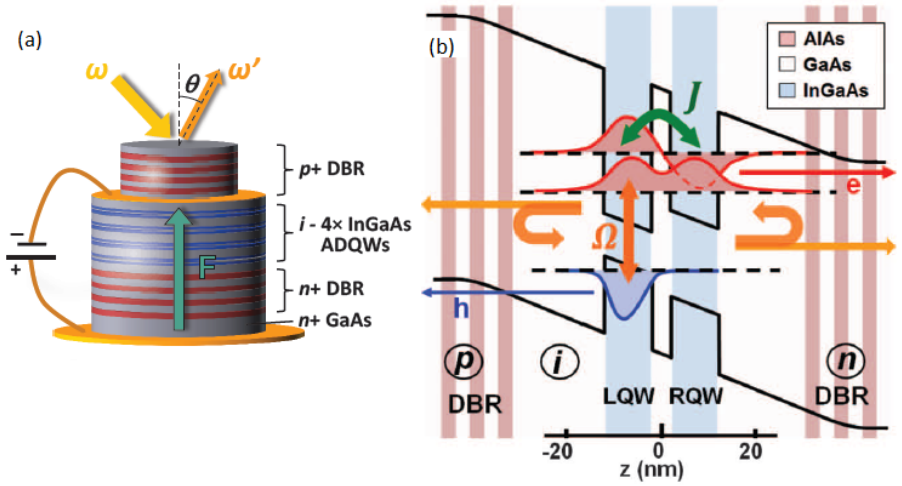

Figure 1.9: (a): The sketch of dipolariton setup. The system of four asymmetric double quantum wells is embedded into microcavity, with external electric field controlling the energy of indirect exciton state. (b) The schematic representation of double quantum well energy structure and wave functions, along with coupling to cavity photon. The figure is adapted from Ref. [42].

[42]. In the matrix form the Hamiltonian and wave function read as

$$H = \hbar \begin{pmatrix} \omega_{IX} & J/2 & 0 \\ J/2 & \omega_{DX} & \Omega/2 \\ 0 & \Omega/2 & \omega_C \end{pmatrix}, \quad |\Psi\rangle = \begin{pmatrix} \Psi_{IX} \\ \Psi_{DX} \\ \Psi_C \end{pmatrix}, \tag{1.24}$$

where ω_C, ω_{DX} and ω_{IX} correspond to the frequencies of cavity mode, direct exciton and indirect exciton, respectively. The coupling constant between photon and direct exciton is $\hbar\Omega$ (Rabi energy), and the tunneling rate corresponding to transitions between direct and indirect excitons is $\hbar J$. The wave-function $|\Psi\rangle$ of dipolariton is the superposition of the uncoupled wave functions Ψ_C, Ψ_{DX} and Ψ_{IX}, correspodning to the field operators for cavity photon, direct exciton and indirect exciton, respectively.

The energies of dipolariton modes can be found via diagonalization of Hamiltonian (1.24). The new eigenenergies of the system are shown in Fig. 1.10, as a function of detuning between direct and indirect exciton modes (a) and in-plane momentum (b). The parameters for the calculation are close to those obtained in Ref. [42], where $In_{0.1}Ga_{0.9}As/GaAs/In_{0.08}Ga_{0.92}As$ heterostructure was studied. The tunneling rate is $\hbar J = 6$ meV, and the indirect exciton energy depends linearly on the external electric field amplitude. The Rabi frequency of photon-exciton coupling is $\hbar\Omega = 6$ meV, and photon detuning was taken as $\delta_\Omega = \hbar\omega_C - \hbar\omega_{DX} = -5$ meV. Also, in Fig. 1.10 (b) we fixed exciton detuning to $\delta_J = \hbar\omega_{DX} - \hbar\omega_{IX} = -5$ meV.

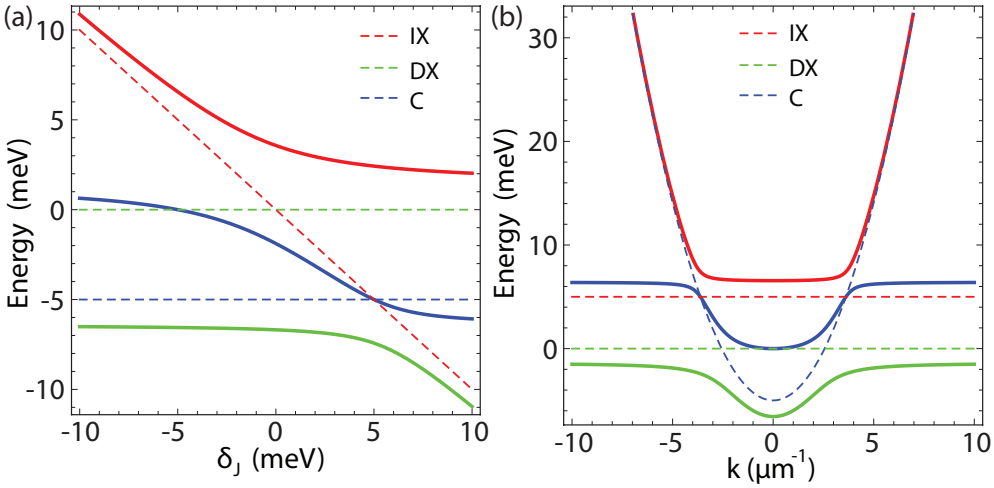

Figure 1.10: (a): Energies of the dipolariton modes (solid curves) plotted as a function of detuning between direct and indirect exciton modes. Bare modes are depicted by dashed curves. (b): Dispersion of dipolariton excitations plotted for the fixed exciton detuning $\delta_J = \hbar\omega_{DX} - \hbar\omega_{IX} = -5$ *meV.*

It should be mentioned, that the dynamics of three coupled oscillators system has rich phenomenology. Namely, the strong coupling between levels leads to so-called Rabi flopping process, which consists in population oscillations between the coupled modes occurring at characteristic Rabi frequency. The electron tunneling between direct and indirect excitons results in oscillations of dipole momentum. The frequency of such oscillations typically lies in terahertz range, which leads to classical radiation of THz signal by the Hertz dipole array [43]. The strong coupling between direct exciton and the cavity mode lead to the superradiant character of radiation, resulting in the quantum efficiency of the emitter. Additionally, the Rabi oscillations and consequent continuous THz emission can be further enhanced in higher excitation regime, when the interaction effects become relevant [44, 45].

The dipolariton setups potentially can have significant impact on the Bose-Einstein condensation phenomena as well. While the condensate of exciton-polaritons are routinely obtained nowadays [24], an unambiguous experimental evidence of exciton condensation is lacking so far. In the frameworks of the current thesis we propose an algorithm of Bose-Einstein condensation of indirect excitons in dipolaritons system. The idea is based on the separation of the process of optical pump and initial condensation, which takes place in pure polaritonic configuration (with decoupled indirect exciton mode) and consequent transition of coherent population to the indirect exciton state. The detailed discussion is presented in the Chapter 4.

1.3. Electromagnetically dressed two-level quantum systems

In the current section we will consider the interaction of two-level quantum system with external time-periodic electromagnetic field [1] . The latter represents itself one of the model problems of quantum physics, finding applications in wide range of areas, covering quantum optics, qubits, spin-related phenomena, atomic physics, etc. In the framework of the current paper we employ two-model system to describe the quantum dot optical properties. Namely, in the chapter 2 we treat as upper an lower states the size quantization levels of quantum dot, while in chapter 3 we deal with interband transitions, with states denoting electron in conduction and valence band.

We restrict the consideration with the case of monochromatic laser field:

$$\mathbf{E}(t) = \mathbf{e}E_0 \cos\omega t = \mathbf{e}\frac{E_0}{2}(e^{-i\omega_L t} + e^{i\omega_L t}) = \mathbf{E}^{(+)}(t) + \mathbf{E}^{(-)}(t), \tag{1.25}$$

where $\mathbf{e}$ is the unit polarization vector, E_0 denotes the field amplitude, and ω_L is angular frequency. Here we neglect the spatial dependence of the field, which is reasonable in the long-wavelength approximation, when the wavelength is much longer than the characteristic size of the structure. In the domain of optical frequencies, where we operate, such an approximation is completely valid.

The two-level system Hamiltonian read as

$$H_{QD} = \hbar\omega_0 |e\rangle\langle e|, \tag{1.26}$$

where $|e\rangle$ denotes the excited state, $\hbar\omega_0$ denotes the two-level separation energy, and we choose the zero of energy to corresponding ground state $|g\rangle$. The subscript "QD" we use for two-level system Hamiltonian stands for quantum dot, although the presented theory is of general character.

The interaction with the field is given in the form

$$H_{QD-F} = -\mathbf{dE}, \tag{1.27}$$

where $\mathbf{d}$ denotes the system dipole operator, read as

$$\mathbf{d} = \mathbf{d}_{eg}(\sigma^- + \sigma^+) = \mathbf{d}^{(+)} + \mathbf{d}^{(-)}, \tag{1.28}$$

where $\sigma^- = |g\rangle\langle e|$, $\sigma^+ = |e\rangle\langle g|$. Note that for the symmetric two-level systems $\mathbf{d}_{ee} = \mathbf{d}_{gg} = 0$. In the current section we will deal with symmetric systems, noting that the break of time reversal symmetry leads to rise of various nontrivial effects, presented in the following chapters. Thus, for the moment the system total Hamiltonian is

$$H = H_{QD} + H_{QD-F} = \hbar\omega_0\sigma^+\sigma^- - \mathbf{dE}, \tag{1.29}$$

[1] The current section is based on the Refs. [46, 47]

with $\sigma^+\sigma^- = |e\rangle\langle e|$ corresponding to the excited state projection operator. Next, expanding dipole and field operators, for the interaction term we can write

$$H_{QD-F} = -\mathbf{d}^{(+)}\mathbf{E}^{(+)} - \mathbf{d}^{(-)}\mathbf{E}^{(-)} - \mathbf{d}^{(+)}\mathbf{E}^{(-)} - \mathbf{d}^{(-)}\mathbf{E}^{(+)}. \tag{1.30}$$

Here we note that dipole and field operators have time dependences $\mathbf{d}^{(\pm)} \sim e^{\mp i\omega_0 t}$, $\mathbf{E}^{(\pm)} \sim e^{\mp i\omega_L t}$, meaning that the first two terms oscillate as $e^{\pm i(\omega_L+\omega_0)t}$, while the last terms as $e^{\pm i\Delta t}$, where $\Delta = \omega_L - \omega_0$. In the case of near-resonant interaction, when $\Delta << \omega_L + \omega_0$, we can make so-called rotating wave approximation (RWA), consisting in omitting the quickly oscillating terms. The latter is reasonable since on a large time scale their average value is zero. Thus, in the RWA we have

$$H^{RWA}_{QD-F} = -\mathbf{d}^{(+)}\mathbf{E}^{(-)} - \mathbf{d}^{(-)}\mathbf{E}^{(+)} = \frac{\hbar\Omega}{2}(\sigma^- e^{i\omega_L t} + \sigma^+ e^{-i\omega_L t}), \tag{1.31}$$

where we introduce the Rabi frequency

$$\Omega = -\frac{2\mathbf{e}\mathbf{d}_{eg}E_0}{2}. \tag{1.32}$$

We note that interlevel transition matrix elements have induced character, being aligned parallel to the electric field vector.

Thus, in the RWA Hamiltonian takes the form

$$H^{RWA} = \hbar\omega_0\sigma^+\sigma^- + \frac{\hbar\Omega}{2}(\sigma^- e^{i\omega_L t} + \sigma^+ e^{-i\omega_L t}). \tag{1.33}$$

We proceed now with the systems dynamics. For this purpose we introduce generic wavefunction in the form

$$|\psi\rangle = c_g|g\rangle + c_e|e\rangle, \tag{1.34}$$

where $c_{g,e}$ are time dependent coefficients. Substituting then 1.34 into Scrodinger equation

$$i\hbar\frac{\partial|\psi\rangle}{\partial t} = H^{RWA}|\psi\rangle, \tag{1.35}$$

we arrive to the following equation:

$$\frac{\partial c_g}{\partial t}|g\rangle + \frac{\partial c_e}{\partial t}|e\rangle = -i\omega_0 c_e|e\rangle - i\frac{\Omega}{2}e^{i\omega_L t}c_e|g\rangle - i\frac{\Omega}{2}e^{-i\omega_L t}c_g|e\rangle. \tag{1.36}$$

Next, projecting the states $\langle g|$, $\langle e|$, we obtain two coupled differential equations describing the systems time dynamics:

$$\begin{aligned}\frac{\partial c_g}{\partial t} &= -i\frac{\Omega}{2}e^{i\omega_L t}c_e,\\ \frac{\partial c_e}{\partial t} &= -i\omega_0 c_e - i\frac{\Omega}{2}e^{-i\omega_L t}c_g.\end{aligned} \tag{1.37}$$

In order to eliminate the oscillations on the optical frequency ω_L, we will modify the excited state amplitude to the form

$$c_e = a_e e^{i\omega_L t}. \tag{1.38}$$

Substituting, we have

$$\begin{aligned} \frac{\partial c_g}{\partial t} &= -i\frac{\Omega}{2}a_e, \\ \frac{\partial a_e}{\partial t} &= -i\Delta a_e - i\frac{\Omega}{2}c_g. \end{aligned} \tag{1.39}$$

It worth mentioning at this point that we could obtain the equations (1.39) from the Hamiltonian in the rotating frame, i. e.,

$$\tilde{H} = \hbar\Delta\sigma^+\sigma^- + \frac{\hbar\Omega}{2}(\sigma^- + \sigma^+), \tag{1.40}$$

which, in its turn, is obtained from the unitary transformation of initial Hamiltonian

$$\tilde{H} = UHU^\dagger + i\hbar\frac{\partial U}{\partial t}U^\dagger, \tag{1.41}$$

with $U = exp(i\omega_L t|e\rangle\langle e|)$.

Next, differentiating each of eqs. (1.39) and substituting the first order terms, we arrive to uncoupled second order differential equations:

$$\begin{aligned} \frac{\partial^2 c_g}{\partial t^2} - i\Delta\frac{\partial c_g}{\partial t} + \frac{\Omega^2}{4}c_g &= 0, \\ \frac{\partial^2 a_e}{\partial t^2} - i\Delta\frac{\partial a_e}{\partial t} + \frac{\Omega^2}{4}a_e &= 0. \end{aligned} \tag{1.42}$$

The general solution can be written in the form

$$\begin{aligned} c_g(t) &= e^{i\frac{\Delta t}{2}}\left[c_g(0)\cos\frac{\Omega_R t}{2} - i\frac{\Delta c_g(0) + \Omega a_e(0)}{\Omega_R}\sin\frac{\Omega_R t}{2}\right], \\ a_e(t) &= e^{i\frac{\Delta t}{2}}\left[a_e(0)\cos\frac{\Omega_R t}{2} - i\frac{\Delta a_e(0) + \Omega c_g(0)}{\Omega_R}\sin\frac{\Omega_R t}{2}\right], \end{aligned} \tag{1.43}$$

where we introduce the generalized Rabi frequency

$$\Omega_R = \sqrt{\Omega^2 + \Delta^2}. \tag{1.44}$$

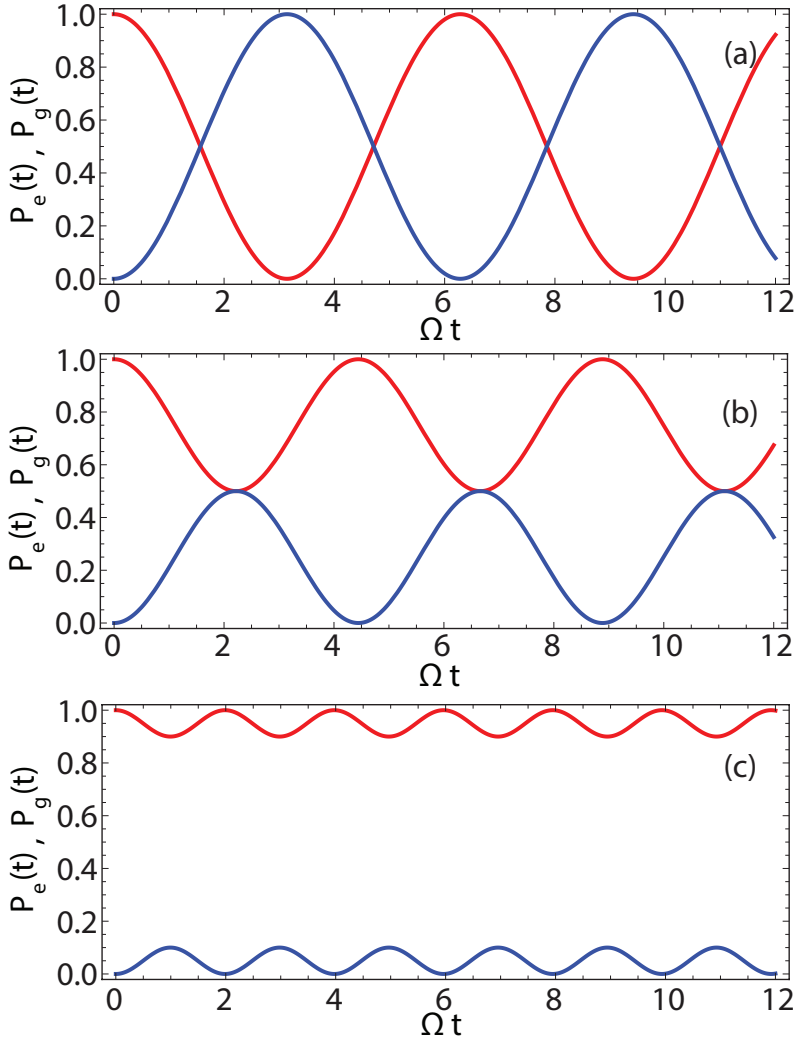

Figure 1.11: The time dynamics of ground (red curve) and excited (blue curve) state population for the detuning values (a) $\Delta = 0$, (b) $\Delta = \Omega$, (c) $\Delta = 3\Omega$.

Coefficients $c_g(0)$ and $a_e(0)$ can be found from the initial conditions.

In particular case of the exact resonance, i. e. $\Delta = 0$, the solution reduces to the form

$$\begin{aligned} c_g(t) &= c_g(0)\cos\frac{\Omega_R t}{2} - i a_e(0)\sin\frac{\Omega t}{2}, \\ a_e(t) &= a_e(0)\cos\frac{\Omega_R t}{2} - i c_g(0)\sin\frac{\Omega t}{2}. \end{aligned} \tag{1.45}$$

Consider the case when the system is initially in the ground state, $c_g(0) = 1$, and $a_e(0) = 0$. Then the time dependences of the state populations read as

$$\begin{aligned} P_g(t) &= |c_g(t)|^2 = \cos^2\frac{\Omega_R t}{2} + \frac{\Delta^2}{\Omega_R^2}\sin^2\frac{\Omega_R t}{2}, \\ P_e(t) &= |a_e(t)|^2 = \frac{\Omega^2}{\Omega_R^2}\sin^2\frac{\Omega_R t}{2}. \end{aligned} \tag{1.46}$$

In the Fig. 1.11 we present the dynamics of the populations for the different values of the ratio Δ/Ω. First of all, for the case of exact resonance $\Delta = 0$ we see the full conversions of populations between ground and excited states, appearing at the Rabi frequency Ω. This oscillating phenomenon is referred as Rabi flopping. Further, for the nonzero detuning the oscillations occur at generalized Rabi frequency Ω_R. One more thing to note that the amplitude of oscillations for the excited state is modulated as Ω^2/Ω_R^2, and thus decrease when detuning grows.

1.3.1. Dressed states

We proceed with the introduction of the concept of dressed states. From the Rabi oscillations between the initial eigenstates we can conclude, that they are not the eigenstates for the total Hamiltonian, accounting for interaction with the field. To find the new eigenstates, let us rewrite the dynamic equations (1.39) in the matrix form:

$$\frac{\partial}{\partial t}\begin{bmatrix} a_e \\ c_g \end{bmatrix} = -i\begin{bmatrix} -\Delta & \Omega/2 \\ \Omega/2 & 0 \end{bmatrix}\begin{bmatrix} a_e \\ c_g \end{bmatrix}, \tag{1.47}$$

and the RWA Hamiltonian is

$$\tilde{H} = \begin{bmatrix} -\Delta & \Omega/2 \\ \Omega/2 & 0 \end{bmatrix}. \tag{1.48}$$

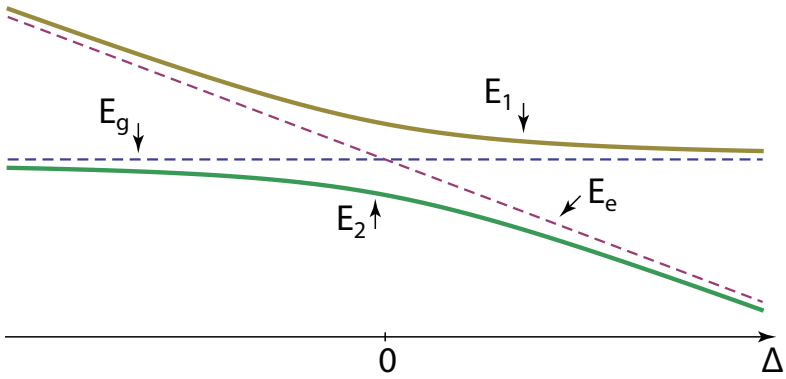

Figure 1.12: The energies of bare (dashed lines) and dressed (solid lines) states as a function of detuning Δ.

After the diagonalization, for the eigenvalues we get

$$E_{1,2} = -\frac{\hbar\Delta}{2} \pm \frac{\hbar\Omega_R}{2} \tag{1.49}$$

with corresponding eigenvectors

$$\begin{aligned} |1\rangle &= \sin\theta|g\rangle + \cos\theta|e\rangle, \\ |2\rangle &= \cos\theta|g\rangle - \sin\theta|e\rangle, \end{aligned} \tag{1.50}$$

where

$$\begin{aligned} \sin\theta &= \frac{1}{\sqrt{2}}\sqrt{1+\frac{\Delta}{\Omega_R}}, \\ \cos\theta &= \frac{1}{\sqrt{2}}\sqrt{1-\frac{\Delta}{\Omega_R}}. \end{aligned} \tag{1.51}$$

In the Fig. 1.12 we present the energies of bare and dressed states, where the excited state energy in the rotating frame is $E_e = -\hbar\Delta$. Here we again meet the phenomenon of avoided crossing, appearing as a result of hybridization of the modes, caused by the interaction. Thus, the concept of dressed states is somewhat analogous to earlier discussed polaritons.

As we saw, in the picture of the bare states the state populations make Rabi oscillations. It is interesting to examine how these oscillations are expressed in the dressed state picture. For simplicity we will consider the case of exact resonance, $\Delta = 0$. Then

the relation between bare and dressed states read as

$$\begin{aligned} |1\rangle &= \frac{1}{\sqrt{2}}(|g\rangle + |e\rangle), \\ |2\rangle &= \frac{1}{\sqrt{2}}(|g\rangle - |e\rangle), \end{aligned} \tag{1.52}$$

and the inverse relations

$$\begin{aligned} |g\rangle &= \frac{1}{\sqrt{2}}(|1\rangle + |2\rangle), \\ |e\rangle &= \frac{1}{\sqrt{2}}(|1\rangle - |2\rangle). \end{aligned} \tag{1.53}$$

Then if the system starts from the two-level ground state $|g\rangle$, in the dressed states picture wave function dynamics will read

$$|\psi(t)\rangle = \frac{1}{\sqrt{2}}\left(e^{-iE_1 t/\hbar}|1\rangle + e^{-iE_2 t/\hbar}|2\rangle\right) = \frac{e^{-i\Omega t/2}}{\sqrt{2}}\left(|1\rangle + e^{i\Omega t}|2\rangle\right), \tag{1.54}$$

The characteristic frequency of the system is Rabi frequency, so the dynamics must be periodic with Ω. Calculating the wave function at the moments $\Omega t = \pi$ and $\Omega t = 2\pi$, we get

$$\begin{aligned} |\psi(t = \pi/\Omega)\rangle &= \frac{1}{\sqrt{2}}\left(|1\rangle + e^{i\pi}|2\rangle\right) = |e\rangle, \\ |\psi(t = 2\pi/\Omega)\rangle &= \frac{1}{\sqrt{2}}\left(|1\rangle + e^{i2\pi}|2\rangle\right) = |g\rangle. \end{aligned} \tag{1.55}$$

where we drop an irrelevant overall phase. As expected, we get the same result.

1.3.2. Full quantum picture: Jaynes-Cummings model

So far we were considering the interaction of two-level quantum system with classical external field. However, such a semiclassical approach represents itself the limiting case of full quantum treatment, where we account the quantum nature of field component as well. The semiclassical approach is relevant for large values of the field amplitude, when the fluctuations of photon number become negligibly small in comparison with photon mean number. Below we present the theory of two-level system interacting with quantum field. The reason for this is that in such a picture we can clearly identify the processes of absorption and stimulated emission, and thus provide very illustrative physical explanation of the fluorescence spectra of the system under consideration.

As before, we describe the two-level system by Hamiltonian

$$H_{QD} = \hbar\omega_0 |e\rangle\langle e|, \tag{1.56}$$

with the ground state energy being equal to zero. The field component read as

$$H_F = \hbar\omega_L \left(a^\dagger a + \frac{1}{2} \right), \tag{1.57}$$

with a denoting the photon annihilation operator. The interaction term is

$$H_{QD-F} = -\mathbf{dE}, \tag{1.58}$$

where we recall the dipole momentum definition

$$\mathbf{d} = \mathbf{d}_{eg}(\sigma^- + \sigma^+), \tag{1.59}$$

and the field amplitude read as

$$\mathbf{E} = -\mathbf{e}\sqrt{\frac{\hbar\omega_L}{2\varepsilon\varepsilon_0 V}}(a + a^\dagger). \tag{1.60}$$

Defining the coupling energy

$$\hbar g = -\mathbf{e}\sqrt{\frac{\hbar\omega_L}{2\varepsilon\varepsilon_0 V}}\mathbf{d}_{eg}, \tag{1.61}$$

and inserting to the coupling Hamiltonian, we get

$$H_{QD-F} = \hbar g(\sigma^- + \sigma^+)(a + a^\dagger). \tag{1.62}$$

Applying again rotating wave approximation and eliminating the quickly oscillating terms, we finally get

$$H_{QD-F}^{RWA} = \hbar g(\sigma^- a^\dagger + \sigma^+ a). \tag{1.63}$$

The full Hamiltonian now will be

$$H_{JC} = H_{QD} + H_F + H_{QD-F}^{RWA} = \hbar\omega_0\sigma^+\sigma^- + \hbar\omega_L a^\dagger a + \hbar g(\sigma^- a^\dagger + \sigma^+ a), \tag{1.64}$$

where we drop the field vacuum oscillations energy. "JC" here denotes the names of E. Jaynes and F. Cummings, who suggested this model.

To study the system dynamics, we employ the generic wave function in the form

$$|\psi(t)\rangle = |\psi_{ph}(t)\rangle \otimes |\psi_{QD}(t)\rangle = \sum_{N=0}^{\infty} \left[c_{g,N}|g, N\rangle + c_{e,N}|e, N\rangle \right]. \tag{1.65}$$

Inserting into the Schrodinger equation and projecting with $\langle e|$ and $\langle g|$ we derive the set of coupled differential equations

$$\frac{\partial c_{e,N}}{\partial t} = -i(\omega_0 + N\omega_L)c_{e,N} - i\sqrt{N+1}gc_{g,N+1},$$
$$\frac{\partial c_{g,N+1}}{\partial t} = -i(N+1)\omega_L c_{g,N+1} - i\sqrt{N+1}gc_{e,N},$$
(1.66)

where we use the annihilation operator in the following form:

$$a = \sum_{N=0}^{\infty} \sqrt{N+}|N\rangle\langle N+1|. \tag{1.67}$$

The equations are equivalent to the semiclassical equations (1.42) with Rabi frequency $\Omega \leftrightarrow 2g\sqrt{N+1}$ and the detuning

$$(N+1)\omega_L - (\omega_0 + N\omega_L) = \omega_L - \omega_0 = \Delta. \tag{1.68}$$

Thus, the problem is reduced to the semiclassical case, meaning that the solutions are readily found. For instance, starting from the ground state $|g, N+1\rangle$, for the populations we have

$$P_{g,N+1}(t) = \cos^2\frac{\Omega_{R,N}t}{2} + \frac{\Delta^2}{\Omega_{R,N}^2}\sin^2\frac{\Omega_{R,N}t}{2},$$
$$P_{e,N}(t) = \frac{4(N+1)g^2}{\Omega_{R,N}^2}\sin^2\frac{\Omega_{R,N}t}{2},$$
(1.69)

where we introduce quantized generalized Rabi frequency $\Omega_{R,N} = \sqrt{4(N+1)g^2 + \Delta^2}$. We note that in the case when $N >> 1$, the population dynamics (1.69) and generalized Rabi frequency dependence on photon number is negligible, i. e., $P_{e,N}(t) \simeq P_{e,N+1}(t)$. It corresponds to the transition to semiclassical case. The semiclassical Hamiltonian can also be derived from the Jaynes-Cummings Hamiltonian by substitution $a = a^\dagger = \sqrt{N}$.

1.3.3. Dressed states in full quantum picture: rise of Mollow triplet

In analogy with the semiclassical case, we can introduce introduce quantum dressed states, corresponding to the eigenstates of Jaynes-Cummings Hamiltonian, in the following form:

$$|1,(N)\rangle = \sin\theta_N|g, N+1\rangle + \cos\theta_N|e, N\rangle,$$
$$|2,(N)\rangle = \cos\theta_N|g, N+1\rangle - \sin\theta_N|e, N\rangle,$$
(1.70)

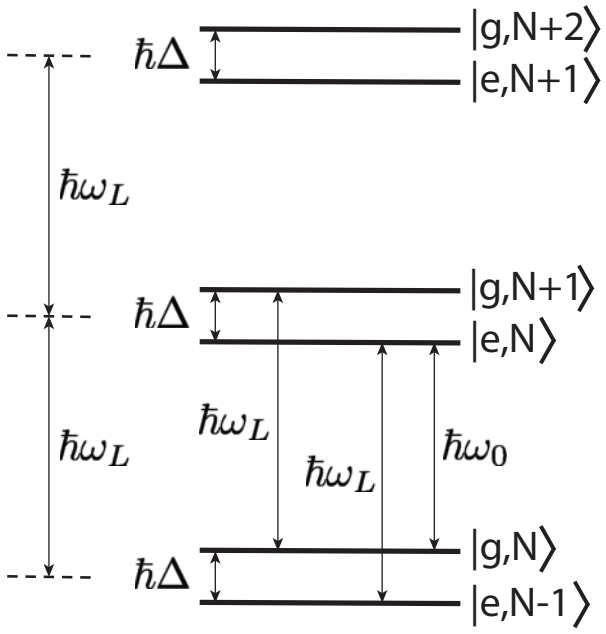

Figure 1.13: The energies of uncoupled two-level states together with photon component.

where

$$\sin\theta_N = \frac{1}{\sqrt{2}}\sqrt{1+\frac{\Delta}{\Omega_{R,N}}},$$
$$\cos\theta_N = \frac{1}{\sqrt{2}}\sqrt{1-\frac{\Delta}{\Omega_{R,N}}}. \tag{1.71}$$

We next examine the energy structure of the system. First of all let us start with the noninteracting case. In the Fig. 1.13 we present the energy of the bare two-level states and photon number. As we see, in the near resonant case ($Delta << \omega_0$), the states $|g, N+1\rangle$, $|e, N\rangle$, are situated close by energy to each other (the separation energy is $\hbar\Delta$. When the interaction is turned on, the mentioned states form one manifold of dressed states, which are separated by energy $\hbar\Omega_{R,N}$ (see Fig. 1.14).

In order to give qualitative explanation of two-level dressed system resonance fluorescence spectra, on the Fig. 1.14 we depict two neighboring manifolds of the dressed states ladder. To find out the allowed transitions, we recall the evidence, that only the nondiagonal matrix elements of dipole momentum are nonzero, $\mathbf{d}_e g \neq 0$. It means that

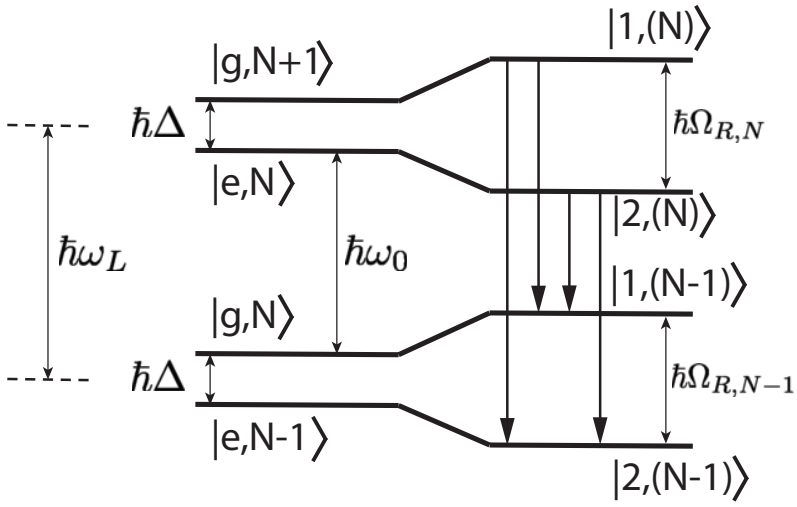

Figure 1.14: The energetic scheme of two-level dressed states and allowed optical transitions.

in the uncoupled basis (left side of Fig. 1.14) only the transitions between $|e, N\rangle$ and $|g, N\rangle$ are allowed. At the same time, the dressed states of upper manifold $|1, (N)\rangle$ and $|2, (N)\rangle$ contain the component $|e, N\rangle$, while the states f lower manifold $|1, (N-1)\rangle$ and $|2, (N-1)\rangle$ contain $|g, N\rangle$. Thus, all four transitions between the states of neighboring manifolds become allowed. We note also, that in the limit of strong field $N >> 1$, the fluctuations of photon number become negligible, and the frequencies of optical transitions between any neighboring manifolds are consequently independent of photon number. Thus, the resonance fluorescence spectra of dressed symmetric two-level system is formed by cascades of transitions between neighboring manifolds, appearing at the frequencies $\omega_L - \Omega_R$, ω_L, $\omega_L + \Omega_R$, forming the Mollow triplet structure.

Finally, we see that the transitions between the levels of the same manifold are not allowed, since they not simultaneously contain the states $|e, N\rangle$ and $|g, N\rangle$. The situation is completely different in the case of systems with broken inversion symmetry, when $\mathbf{d}_{ee} \neq 0$. The effects, appearing there, are discussed in the chapters 2 and 3.

2. Resonance fluorescence from a doubly dressed asymmetric quantum dot

We present the theory of resonance fluorescence from an asymmetric quantum dot driven by a two-component electromagnetic field with two different frequencies, polarizations and amplitudes (bichromatic field) in the regime of strong light-matter coupling. It follows from the elaborated theory that the broken inversion symmetry of the driven quantum system and the bichromatic structure of the driving field result in unexpected features of the resonance fluorescence, including the infinite set of Mollow triplets, the quench of fluorescence peaks induced by the dressing field, and the oscillating behavior of the fluorescence intensity as a function of the dressing field amplitude. These quantum phenomena are of general physical nature and, therefore, can take place in various double-driven quantum systems with broken inversion symmetry.

2.1. Introduction

Advances in nanotechnology, laser physics and microwave techniques created a basis for studies of the strong light-matter coupling in various quantum systems. Differently from the case of weak electromagnetic field, the interaction between electrons and a strong field cannot be treated as a perturbation. Therefore, the system "electron + strong field" is conventionally considered as a composite electron-field object which was called "electron dressed by field" (dressed electron) [46, 48]. The field-induced modification of physical properties of dressed electrons was studied in both atomic systems [46, 48, 49] and various condensed-matter structures, including bulk semiconductors [50, 51], graphene [52, 53, 54, 55, 56], quantum wells [57, 58, 59, 60, 61, 62], quantum rings [63, 64, 65, 66], quantum dots [67, 68, 69, 70, 71, 72, 73, 74, 75, 76, 77], etc. Among these structures, quantum dots (QDs) — semiconductor 3D structures of nanometer scale, which are referred to as "artificial atoms" — seem to be most interesting for optical studies since they are basic elements of modern nanophotonics [78, 79]. In contrast to natural atoms, the most of QDs are devoid of inversion symmetry and, therefore, are asymmetric. As an example, QDs based on gallium nitride heterostructures have a strong built-in electric field [80, 81] and, therefore,

acquire the giant anisotropy [82, 83, 84, 85, 86]. This motivates to studies of various asymmetry-induced optical effects in QDs [74, 75, 76, 77].

The most of studies of dressed quantum systems was performed before for a monochromatic dressing field. However, there is a lot of interesting phenomena specific for quantum systems driven by a two-mode electromagnetic field with two different frequencies, polarizations and amplitudes (bichromatic field). In symmetric quantum systems (atoms and superconducting qubits), the bichromatic coupling leads to features of photon correlations, squeezing, Autler-Townes effect, suppression of spontaneous emission, multi-photon transitions, etc. [87, 88, 89, 90, 91, 92, 93, 94]. Broken symmetry brings substantially new physics to bichromatically dressed quantum systems, including additional lines in optical spectra, multiple splitting of the dressed-state transitions, etc. [95, 96, 97]. Although these optical effects are extensively studied during long time, a consistent quantum theory of resonance fluorescence from bichromatically dressed asymmetric systems was not elaborated before. The present research is aimed to fill this gap at the border between quantum optics and physics of nanostructures. To solve the problem, we focused on the strong light-matter coupling regime when the interaction of an asymmetric QD with a bichromatic dressing field overcomes the spontaneous emission and non-radiative decay of QD excitations. In this case, the spectral lines of QD are well resolved and various radiation effects (particularly, the resonance fluorescence) can be analyzed using a concept of quasienergetic (dressed) electronic states. In the framework of this approach, such characteristics of dressed QD as decay rates and lineshapes can be calculated by solving the master equations in the representation of quasienergetic states. As a result, we found unexpected features of resonance fluorescence, which are discussed below.

The chapter is organized as follows. In the Section 2, we derive quasienergetic electronic states for an asymmetric QD dressed by a bichromatic electromagnetic field and calculate matrix elements of optical dipole transitions between these states. In the Section 3, we apply the found quasienergetic spectrum of dressed electrons to elaborate the theory of resonance fluorescence from the QD. The Section 4 contains the discussion of the calculated spectra of resonance fluorescence and the conclusion.

2.2. Model of electronic structure

Let us consider an asymmetric QD with broken inversion symmetry along the z axis, which is dressed by the bichromatic field

$$\mathbf{E}(t) = \mathbf{E}_1 \cos \omega_1 t + \mathbf{E}_2 \cos \omega_2 t, \tag{2.1}$$

where the electric field of the first mode, $\mathbf{E}_1$, is directed along the z axis and the electric field of the second mode, $\mathbf{E}_2$, is perpendicular to this axis (see Fig. 2.1 (a)). In what follows, we will assume that the second frequency, ω_2, is near the electronic resonance

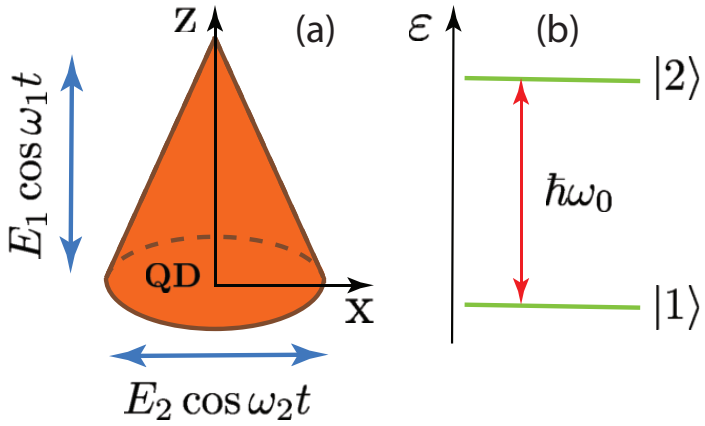

Figure 2.1: Sketch of the system under consideration: (a) Asymmetric quantum dot (QD) with broken inversion symmetry along the z axis, which is exposed to a bichromatic electromagnetic field with the electric field amplitudes $E_{1,2}$ and the frequencies $\omega_{1,2}$; (b) Two-level model of the electronic energy spectrum of the QD, ε, with the interlevel distance $\hbar\omega_0$.

frequency, ω_0, whereas the first frequency, ω_1, is far from all resonance frequencies. As a consequence, the bichromatic field (2.1) mixes effectively only two electron states of QD, $|1\rangle$ and $|2\rangle$, which are separated by the energy $\hbar\omega_0$ (see Fig. 1b). Within the basis of these two states, the asymmetric QD can be described by the matrix Hamiltonian [74]

$$\hat{\mathcal{H}} = \begin{pmatrix} -\hbar\omega_0/2 - d_{11}E_1\cos\omega_1 t & -d_{12}E_2\cos\omega_2 t \\ -d_{21}E_2\cos\omega_2 t & \hbar\omega_0/2 - d_{22}E_1\cos\omega_1 t \end{pmatrix} \tag{2.2}$$

where $d_{11} = \langle 1|ez|1\rangle$, $d_{22} = \langle 2|ez|2\rangle$ and $d_{12} = d_{21} = \langle 1|ex|2\rangle$ are the matrix elements of the operator of electric dipole moment along the z, x axes, and e is the electron charge. To simplify calculations, the Hamiltonian (2.2) can be written as a sum, $\hat{\mathcal{H}} = \hat{\mathcal{H}}_0 + \hat{\mathcal{H}}'$, where

$$\hat{\mathcal{H}}_0 = \begin{pmatrix} -\hbar\omega_0/2 - d_{11}E_1\cos\omega_1 t & 0 \\ 0 & \hbar\omega_0/2 - d_{22}E_1\cos\omega_1 t \end{pmatrix} \tag{2.3}$$

is the diagonal part of the full Hamiltonian (2.2), and

$$\hat{\mathcal{H}}' = \begin{pmatrix} 0 & -d_{12}E_2\cos\omega_2 t \\ -d_{21}E_2\cos\omega_2 t & 0 \end{pmatrix} \tag{2.4}$$

is the nondiagonal part describing electron transitions between the states $|1\rangle$ and $|2\rangle$ under influence of the field (2.1). Exact solutions of the non-stationary Schrödinger equation with the Hamiltonian (2.3),

$$i\hbar\frac{\partial\psi}{\partial t} = \hat{\mathcal{H}}_0\psi,$$

can be written in the spinor form as

$$\psi^{(-)} = e^{i\omega_0 t/2}\exp\left[i\frac{d_{11}E_1}{\hbar\omega_1}\sin\omega_1 t\right]\begin{pmatrix}1\\0\end{pmatrix} \tag{2.5}$$

and

$$\psi^{(+)} = e^{-i\omega_0 t/2}\exp\left[i\frac{d_{22}E_1}{\hbar\omega_1}\sin\omega_1 t\right]\begin{pmatrix}0\\1\end{pmatrix}. \tag{2.6}$$

Since the two pseudo-spinors (2.5)–(2.6) are the complete basis of the considered electronic system at any time t, we can sought eigenstates of the full Hamiltonian (2.2) as an expansion

$$\widetilde{\psi} = a^{(-)}(t)\psi^{(-)} + a^{(+)}(t)\psi^{(+)}, \tag{2.7}$$

where the time-dependent coefficients $a^{(\pm)}(t)$ obey the equation

$$i\hbar\dot{a}^{(\mp)}(t) = -a^{(\pm)}(t)d_{12}E_2\cos\omega_2 t e^{\mp i\omega_0 t}\exp\left[\pm i\frac{(d_{22}-d_{11})E_1}{\hbar\omega_1}\sin\omega_1 t\right]. \tag{2.8}$$

Applying the Jacobi-Anger expansion,

$$e^{iz\sin\theta} = \sum_{n=-\infty}^{\infty} J_n(z)e^{in\theta},$$

we arrive from Eq. (2.8) at the equation

$$\begin{aligned} i\hbar\dot{a}^{(\mp)}(t) &= -a^{(\pm)}(t)\frac{d_{12}E_2}{2}\sum_{n=-\infty}^{\infty} J_n\left(\frac{(d_{22}-d_{11})E_1}{\hbar\omega_1}\right) \\ &\times \left[e^{\mp i(\omega_0+\omega_2-n\omega_1)t} + e^{\mp i(\omega_0-\omega_2-n\omega_1)t}\right], \end{aligned} \tag{2.9}$$

where $J_n(z)$ is the Bessel function of the first kind. Formally, the equation of quantum dynamics (2.9) describes a two-level quantum system subjected to a multi-mode field. It is well-known that the main contribution to the solution of such equation arises from a mode which is nearest to the resonance. Correspondingly, near the resonance condition,

$$\omega_0 \pm \omega_2 = n\omega_1, \tag{2.10}$$

we can neglect all modes except the resonant one. In this approximation, Eq. (2.9) reads as

$$i\dot{a}^{(\pm)}(t) = a^{(\mp)}(t)F_n e^{\pm i\varphi_n t}, \tag{2.11}$$

where $F_n = -(d_{12}E_2/2\hbar)J_n\left(\widetilde{\omega}/\omega_1\right)$ are the Rabi frequencies of the considered system,

$$\widetilde{\omega} = \frac{E_1(d_{22} - d_{11})}{\hbar} \tag{2.12}$$

is the effective frequency, and $\varphi_n = \omega_0 \pm \omega_2 - n\omega_1$ is the resonance detuning. It follows from Eq. (2.11) that the considered problem is reduced to the effective two-level system driven by the monochromatic field with the combined frequency φ_n. Using the well-known solution of Eq. (2.11) (see, e.g., Ref. [98]), we can write the sought wave functions (2.7) in the conventional form of quasienergetic (dressed) states as

$$\begin{aligned}\widetilde{\psi}_1 &= e^{-i\tilde{\varepsilon}_1 t/\hbar}\left[\sqrt{\frac{1}{2}\left(1+\frac{\varphi_n}{2\Omega_n}\right)}\Lambda_{11}(t)\begin{pmatrix}1\\0\end{pmatrix}\right.\\ &- \left.\sqrt{\frac{1}{2}\left(1-\frac{\varphi_n}{2\Omega_n}\right)}e^{i(\varphi_n-\omega_0)t}\Lambda_{22}(t)\begin{pmatrix}0\\1\end{pmatrix}\right],\end{aligned} \tag{2.13}$$

$$\begin{aligned}\widetilde{\psi}_2 &= e^{-i\tilde{\varepsilon}_2 t/\hbar}\left[\sqrt{\frac{1}{2}\left(1+\frac{\varphi_n}{2\Omega_n}\right)}\Lambda_{22}(t)\begin{pmatrix}0\\1\end{pmatrix}\right.\\ &+ \left.\sqrt{\frac{1}{2}\left(1-\frac{\varphi_n}{2\Omega_n}\right)}e^{-i(\varphi_n-\omega_0)t}\Lambda_{11}(t)\begin{pmatrix}1\\0\end{pmatrix}\right],\end{aligned} \tag{2.14}$$

where

$$\tilde{\varepsilon}_1 = -\frac{\hbar\omega_0}{2} - \hbar\Omega_n + \hbar\frac{\varphi_n}{2}, \quad \tilde{\varepsilon}_2 = \frac{\hbar\omega_0}{2} + \hbar\Omega_n - \frac{\hbar\varphi_n}{2}. \tag{2.15}$$

are the corresponding quasienergies and

$$\Lambda_{ii}(t) = \exp\left[i\frac{d_{ii}E_1}{\hbar\omega_1}\sin\omega_1 t\right], \quad \Omega_n = \sqrt{\frac{\varphi_n^2}{4} + F_n^2}.$$

As to optical transitions between the dressed states (2.13) and (2.14), they can be described by the matrix dipole elements

$$\tilde{d}_{ij}(t) = \langle\widetilde{\psi}_i|ex|\widetilde{\psi}_j\rangle = d_{ij}^{(+)} + d_{ij}^{(-)}, \tag{2.16}$$

where $d_{ij}^{(+)} = \left[d_{ji}^{(-)}\right]^*$,

$$\begin{aligned}d_{21}^{(+)} &= \frac{d_{21}}{2}\left[1+\frac{\varphi_n}{2\Omega_n}\right]\Lambda^*(t)e^{i(\omega_0-\varphi_n+2\Omega_n)t},\\ d_{21}^{(-)} &= -\frac{d_{12}}{2}\left[1-\frac{\varphi_n}{2\Omega_n}\right]\Lambda(t)e^{-i(\omega_0-\varphi_n-2\Omega_n)t},\\ d_{11}^{(+)} &= -d_{22}^{(+)} = -\frac{d_{12}}{2}\frac{F_n}{\Omega_n}\Lambda^*(t)e^{i(\omega_0-\varphi_n)t},\end{aligned} \tag{2.17}$$

and $\Lambda(t) = \Lambda_{22}(t)\Lambda_{11}^*(t)$.

2.3. Resonance fluorescence

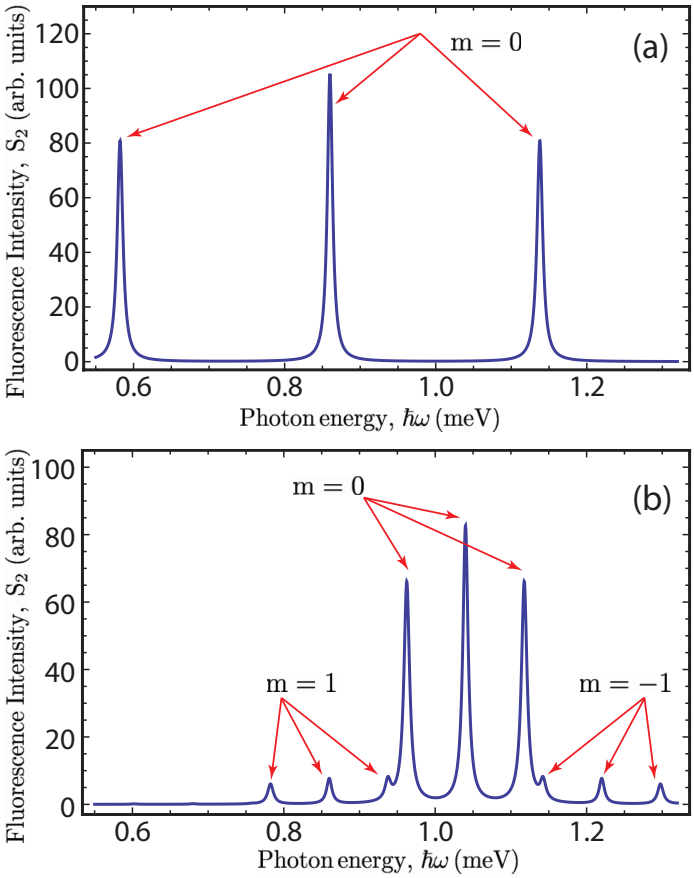

Figure 2.2: The spectra of resonance fluorescence from an asymmetric quantum dot with the interlevel distance $\hbar\omega_0 = 1$ meV, dipole moments $d_{22} - d_{11} = d_{12} = 40$ D, and the decay rate $\gamma = 10^{-10}$ s^{-1}: (a) in the presence of a monochromatic dressing field with the amplitude $E_2 = 3 \cdot 10^3$ V/cm and the frequency $\omega_2 = 0.86\,\omega_0$; (b) in the presence of a bichromatic dressing field with the amplitudes $E_1 = 1.3 \cdot 10^3$ V/cm, $E_2 = 3 \cdot 10^3$ V/cm and the frequencies $\omega_1 = 0.18\,\omega_0$, $\omega_2 = 0.86\,\omega_0$. The indices $m = 0, \pm 1$ indicate the different Mollow triplets.

The general theory to describe the resonance fluorescence in the representation of quasienergetic (dressed) states has been elaborated in Refs. [99, 100, 101, 102]. Applying this known approach to the considered dressed QD, we have to write the Hamiltonian of interaction of the QD with the radiative field as

$$\hat{H}_{\rm int} = -\tilde{d}_{ij}(t)[\mathbf{E}^+(t) + \mathbf{E}^-(t)], \tag{2.18}$$

where

$$\mathbf{E}^{\pm}(t) = \int d\omega g^{\pm}(\omega)\mathbf{e}_{\omega}^{\pm}a_{\omega}^{\pm}e^{\mp i\omega t}$$

is the positive (negative) frequency part of the radiative electric field, $\mathbf{E}(t) = \mathbf{E}^{+}(t) + \mathbf{E}^{-}(t)$, the parameters $g^{\pm}(\omega)$, $\mathbf{e}_{\omega}^{\pm}$, $a_{\omega}^{\pm}$ describe the density, polarization and amplitude of the corresponding electromagnetic modes, respectively, and $\tilde{d}_{ij}(t)$ are the dipole matrix elements of dressed QD (2.16)–(2.17). Within the conventional secular approximation and Markov approximation [46], the equations describing the quantum dynamics of the considered two-level system read as

$$\frac{d\sigma_{11}(t)}{dt} = -\Gamma_{11}[\sigma_{11}(t) - \sigma_{11}^{S}], \quad \frac{d\sigma_{12}(t)}{dt} = -\Gamma_{12}\sigma_{12}(t),$$
$$\sigma_{11}(t) + \sigma_{22}(t) = 1,$$

where $\sigma(t) = \mathrm{Tr}\{\rho(t)\}$ is the reduced density operator which involves tracing over reservoir variables, $\sigma_{\alpha\beta} = \langle\widetilde{\psi}_{\alpha}|\sigma|\widetilde{\psi}_{\beta}\rangle$ are the matrix elements of the density operator written in the basis of dressed states (2.13)–(2.14),

$$\sigma_{11}^{S} = \frac{w_{21}}{w_{12} + w_{21}}, \qquad \sigma_{22}^{S} = \frac{w_{12}}{w_{12} + w_{21}} \tag{2.19}$$

are the steady-state populations of the dressed states (2.13)–(2.14),

$$\Gamma_{11} = w_{12} + w_{21}, \ \Gamma_{12} = \frac{\Gamma_{11}}{2} - \mathrm{Re}(M_{11,22} + M_{22,11}) \tag{2.20}$$

are the field-dependent decay rates for the dressed states (2.13)–(2.14),

$$w_{12} = \frac{\gamma}{4}\left(1 - \frac{\varphi_n}{2\Omega_n}\right)^2, \quad w_{21} = \frac{\gamma}{4}\left(1 + \frac{\varphi_n}{2\Omega_n}\right)^2 \tag{2.21}$$

are the probabilities of radiative transitions per unit time between the dressed states (2.13)–(2.14),

$$M_{\alpha,\alpha,\beta,\beta} = \int_0^{\infty} \mathrm{d}\tau\, \widetilde{d}_{\alpha\alpha}(t-\tau)\widetilde{d}_{\beta\beta}(t)\langle E(t)E(t-\tau)\rangle, \tag{2.22}$$

$\langle E(t)E(t-\tau)\rangle$ is the correlation function averaged over the initial state of electromagnetic field, and γ is the spontaneous emission rate. Substituting Eqs. (2.21)–(2.22) into Eqs. (2.19)–(2.20), we arrive at the width of the transitions,

$$\Gamma_{11} = \frac{\gamma}{2}\left(1 + \frac{\varphi_n^2}{4\Omega_n^2}\right), \quad \Gamma_{12} = \frac{\gamma}{4}\left(3 - \frac{\varphi_n^2}{4\Omega_n^2}\right), \tag{2.23}$$

and the difference between the populations of dressed electronic states (2.13)–(2.14),

$$\Delta_S = \sigma_{11}^{S} - \sigma_{22}^{S} = 2w_{21}/\Gamma_{11} - 1. \tag{2.24}$$

Taking into account the aforesaid, the spectrum of resonance fluorescence from QD has the form [48]

$$S(\omega) \sim \frac{1}{\pi}\mathrm{Re}\left\{\int\limits_0^\infty d\tau \langle D^{(+)}(t+\tau)D^{(-)}(t)\rangle e^{-i\omega\tau}\right\}, \tag{2.25}$$

where

$$D^{(\pm)}(t) = \sum_{\alpha,\beta}\sigma_{\alpha\beta}(t)d^{(\pm)}_{\alpha\beta}(t) \tag{2.26}$$

is the positive(negative)-frequency part of the polarization operator written in the basis of dressed states (2.13)–(2.14). Applying the quantum regression theorem [48] and taking into account Eqs. (2.16)–(2.17), we arrive at the correlation function of the polarization operator (2.26) in the steady-state regime for long time t and arbitrary time τ,

$$\begin{aligned}\langle D^{(+)}(t+\tau)D^{(-)}(t)\rangle &= \left[\Delta_S^2 + (1-\Delta_S^2)e^{-\Gamma_{11}\tau}\right]\langle d^{(+)}_{11}(t+\tau)d^{(-)}_{11}(t)\rangle \\ &+ \frac{1}{2}\left[(1+\Delta_S)\langle d^{(+)}_{12}(t+\tau)d^{(-)}_{21}(t)\rangle + (1-\Delta_S)\langle d^{(+)}_{21}(t+\tau)d^{(-)}_{12}(t)\rangle\right]e^{-\Gamma_{12}\tau},\end{aligned} \tag{2.27}$$

where

$$\begin{aligned}\langle d^{(+)}_{11}(t+\tau)d^{(-)}_{11}(t)\rangle &= \frac{d_{12}^2}{4}\frac{F_n^2}{\Omega_n^2}\langle\Lambda^*(t+\tau)\Lambda(t)\rangle e^{i(\omega_0-\varphi_n)\tau} \approx \frac{d_{12}^2}{4}\frac{F_n^2}{\Omega_n^2}\Sigma(\tau)e^{-i\varphi_n\tau}, \\ \langle d^{(+)}_{12}(t+\tau)d^{(-)}_{21}(t)\rangle &= \frac{d_{12}^2}{4}\left(1-\frac{\varphi_n}{\Omega_n}\right)^2\langle\Lambda^*(t+\tau)\Lambda(t)\rangle \\ &\times e^{i(\omega_0-\varphi_n-2\Omega_n)\tau} \approx \frac{d_{12}^2}{4}\left(1-\frac{\varphi_n}{\Omega_n}\right)^2\Sigma(\tau)e^{-i(\varphi_n+2\Omega_n)\tau}, \\ \langle d^{(+)}_{21}(t+\tau)d^{(-)}_{12}(t)\rangle &= \frac{d_{12}^2}{4}\left(1+\frac{\varphi_n}{\Omega_n}\right)^2\langle\Lambda^*(t+\tau)\Lambda(t)\rangle \\ &\times e^{i(\omega_0-\varphi_n+2\Omega_n)\tau} \approx \frac{d_{12}^2}{4}\left(1+\frac{\varphi_n}{\Omega_n}\right)^2\Sigma(\tau)e^{-i(\varphi_n-2\Omega_n)\tau},\end{aligned}$$

and $\Sigma(\tau) = \sum\limits_m J_m^2\left(\widetilde{\omega}/\omega_1\right)e^{i(\omega_0-m\omega_1)\tau}$. Substituting Eq. (2.27) into Eq. (2.25), the spectrum of resonance fluorescence, $S(\omega) = S_1(\omega) + S_2(\omega)$, can be calculated as a sum of the two parts corresponding to the elastic and inelastic scattering of light [48], where the elastic term reads as

$$\begin{aligned}S_1(\omega) &\sim \frac{\Delta_S^2}{\pi}\mathrm{Re}\left\{\int\limits_0^\infty d\tau d^{(+)}_{11}(t+\tau)d^{(-)}_{11}(t)e^{-i\omega\tau}\right\} \\ &= \left[\frac{\Delta_S d_{12}F_n}{2\Omega_n}\right]^2\sum_m J_m^2\left(\frac{\widetilde{\omega}}{\omega_1}\right)\delta(\omega-[n-m]\omega_1-\omega_2)\end{aligned} \tag{2.28}$$

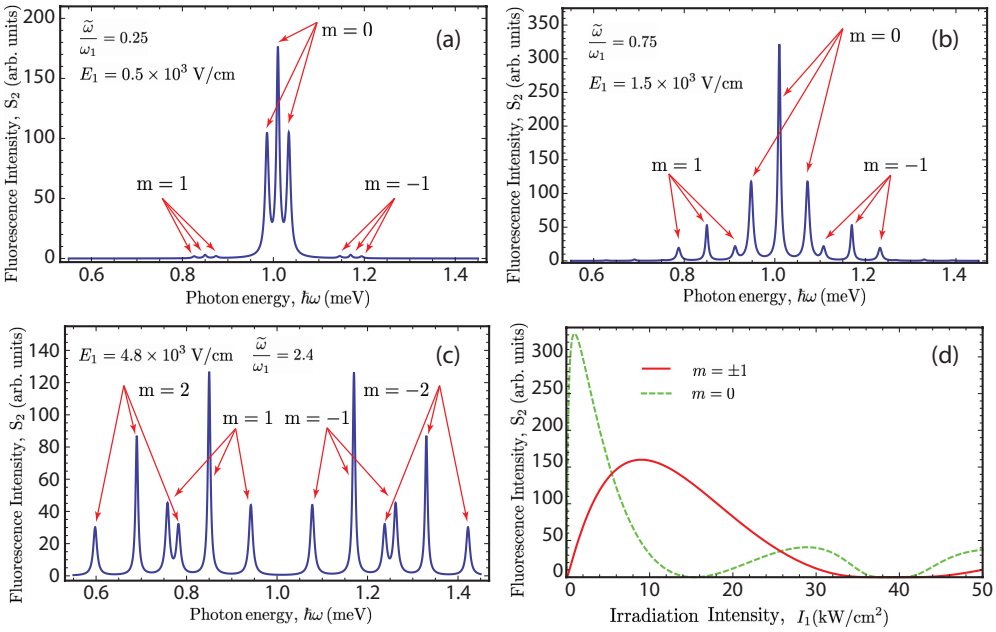

Figure 2.3: The spectra of resonance fluorescence from an asymmetric quantum dot with the interlevel distance $\hbar\omega_0 = 1$ meV, dipole moments $d_{22} - d_{11} = d_{12} = 40$ D, and the decay rate $\gamma = 10^{-10}$ s^{-1} in the presence of a bichromatic dressing field with the frequencies $\omega_1 = 0.16\,\omega_0$ and $\omega_2 = 0.85\,\omega_0$, the amplitude $E_2 = 2.2 \cdot 10^3$ V/cm and different amplitudes E_1: (a)–(c) structure of the Mollow triplets with the numbers $m = 0, \pm 1, \pm 2$; (c) Dependence of the central resonant peaks of the Mollow triplets with the numbers $m = 0, \pm 1$ on the irradiation intensity $I_1 = \varepsilon_0 E_1^2 c/4$.

and the inelastic term is

$$
\begin{aligned}
S_2(\omega) \;\sim\; & \frac{d_{12}^2}{4\pi}\left[\left(1-\Delta_S^2\right)\left(\frac{d_{12}E_2}{2\hbar\Omega_n}\right)^2 J_n^2\left(\frac{\widetilde{\omega}}{\omega_1}\right)\sum_m \frac{J_m^2\left(\widetilde{\omega}/\omega_1\right)\Gamma_{11}}{[\omega-(n-m)\omega_1-\omega_2]^2+\Gamma_{11}^2}\right. \\
& + \frac{1}{2}\frac{\left(1-\varphi_n^2/4\Omega_n^2\right)^2}{\left(1+\varphi_n^2/4\Omega_n^2\right)}\sum_m \frac{J_m^2\left(\widetilde{\omega}/\omega_1\right)\Gamma_{12}}{[\omega-(n-m)\omega_1-\omega_2+2\Omega_n]^2+\Gamma_{12}^2} \\
& + \left.\frac{1}{2}\frac{\left(1-\varphi_n^2/4\Omega_n^2\right)^2}{\left(1+\varphi_n^2/4\Omega_n^2\right)}\sum_m \frac{J_m^2\left(\widetilde{\omega}/\omega_1\right)\Gamma_{12}}{[\omega-(n-m)\omega_1-\omega_2-2\Omega_n]^2+\Gamma_{12}^2}\right].
\end{aligned}
\tag{2.29}
$$

In what follows, we will focus on the inelastic term (2.29) which is responsible for the spectral features of the resonance fluorescence.

2.4. Discussion and conclusion

Let us consider the effect of the two key factors of the considered system — the bichromatic structure of the dressing field and the asymmetry of the QD — on the resonance fluorescence. Mathematically, these two factors can be described by the effective frequency (2.12) appearing in various terms of Eq. (2.29). In order to explain it, we have to keep in mind that the ground and excited states of the asymmetric QD, $|1\rangle$ and $|2\rangle$, do not possess a certain spatial parity along the asymmetry axis, z. Therefore, the diagonal matrix elements of the dipole moment operator in an asymmetric QD prove to be nonequivalent, $d_{22} \neq d_{11}$. As a consequence, the difference of diagonal dipole matrix elements, $d_{22} - d_{11}$, describes the asymmetry of QD [74]. Since the effective frequency (2.12) is the product of this difference and the first field amplitude, E_1, it can be considered as a quantitative measure of both the asymmetry of the QD and the bichromatic nature of the dressing field (2.1). In the following, we will discuss the dependence of the resonance fluorescence on this effective frequency, $\widetilde{\omega} = (d_{22} - d_{11})E_1/\hbar$.

The calculated spectra of resonance fluorescence (2.29) are plotted in Figs. 2.2–2.3 for different effective frequencies, $\widetilde{\omega}$, near the resonance (2.10) with $n = 1$. If the QD is symmetric or the dressing field is monochromatic ($\widetilde{\omega} = 0$), the terms with $m \neq 0$ in Eq. (2.29) vanish since the Bessel functions of the first kind, $J_m(\widetilde{\omega}/\omega_1)$, satisfy the condition $J_m(0) = \delta_{m0}$. The nonzero terms with $m = 0$ correspond physically to the well-known Mollow triplet in the fluorescence spectrum of a two-level system driven by a monochromatic field [48], which is plotted in Fig. 2.2 (a). If the QD is asymmetric and the dressing field is bichromatic ($\widetilde{\omega} \neq 0$), the nonzero terms with $m \neq 0$ in Eq. (2.29) result in the infinite set of Mollow triplets which can be numerated by the index $m = 0, \pm 1, \pm 2, ...$ (see Fig. 2.2 (b) and Figs. 2.3 (a)–(c)). It is shown in Figs. 2.2–2.3 that the bichromatic dressing field generates side Mollow triplets ($m \neq 0$), shifts the main Mollow triplet ($m = 0$) and change the amplitudes of the Mollow triplets. According to Eq. (2.29), the amplitude of the m-th Mollow triplet is proportional to the squared Bessel function, $J_m^2(\widetilde{\omega}/\omega_1)$. This leads to the oscillating dependence of fluorescence peaks on the irradiation intensity, $I_1 = \varepsilon_0 E_1^2 c/4$ (see Fig. 2.3 (d)). It should be stressed that the zeros of the Bessel function, $J_m(\widetilde{\omega}/\omega_1)$, correspond physically to the zero amplitude of the m-th Mollow triplet. Thus, the dressing field can quench fluorescence peaks. Particularly, the absence of the main Mollow triplet ($m = 0$) in Fig. 2.3 (c) is caused by the first zero of the Bessel function $J_0(\widetilde{\omega}/\omega_1)$.

Summarizing the aforesaid, we can conclude that the exciting of asymmetric quantum systems by a bichromatic field results in the following features of resonance fluorescence spectra: an infinite set of Mollow triplets, the quench of fluorescence peaks induced by the dressing field, and the oscillating behavior of the fluorescence intensity as a function of the dressing field amplitude. To explain the physics of these novel effects, we have to stress that the considered bichromatic field (2.1) consists of an off-resonant dressing field $\mathbf{E}_1$ (which renormalizes electronic energy spectrum) and a near-resonant field $\mathbf{E}_2$

(which induces electron transitions between the two electronic levels). Although the dressing field $\mathbf{E}_1$ is off-resonant, it is very strong. Therefore, there are noticeable multiphoton processes which can involve many photons of the field. Particularly, electron transitions between the electronic levels can be accompanied by absorption of both near-resonant photon, $\hbar\omega_2$, and many off-resonant photons, $n\hbar\omega_1$, where n is the number of the photons. As a consequence, there is an infinite set of resonances (2.10) corresponding to the different numbers $n = 0, 1, 2, ...$ Since each resonance is accompanied with its own Mollow triplet, an infinite set of Mollow triplet appears in the fluorescence spectrum. As to the field-induced quench of fluorescence peaks and the oscillating behavior of the fluorescence intensity as a function of the dressing field amplitude, these effects arise from the Bessel-function factors in Eq. (2.29). Physically, these factors describe the nonlinear renormalization of electronic properties with the strong dressing field $\mathbf{E}_1$. It should be noted that the appearance of the Bessel functions in expressions describing dressed electrons is characteristic feature of various quantum systems driven by a dressing field. Particularly, the similar Bessel-function factors describe renormalized electronic properties of dressed quantum wells [103, 104] and graphene [105, 106].

Since the considered quantum phenomena depend on electronic parameters, the elaborated theory paves the new way to the nondestructive optical testing of various asymmetric structures. Applying the developed theory to experimental studies of asymmetric QDs, one should take into account that phonons affect strongly optical transitions in semiconductor structures. To avoid the phonon-induced destruction of the discussed fine structure of the fluorescence spectra, measurements should be performed at low temperatures, T, satisfying the condition $T \ll \Delta\varepsilon$, where $\Delta\varepsilon = \hbar|F_1|$ is the characteristic field-induced shift of electron energies (the dynamic Stark shift).

3. THz Lasing in ensembles of Asymmetric Quantum Dots

In the current chapter we propose a scheme of terahertz (THz) laser based on an ensemble of asymmetric quantum dots dressed by intense electromagnetic field. THz emission originates from the transitions at Rabi energy between the neighboring dressed states. For the amplification of the lasing mode high-Q photonic crystal cavity tuned to terahertz range can be employed. Within the mean field approximation the system is described by Maxwell-Bloch type equations, which account for inhomogeneous broadening and decoherence processes. The conditions for the onset of the lasing are determined and emission intensity and quantum efficiency are obtained by numerical solution of the Langevin type stochastic equations, describing the generation of THz pulses.

3.1. Introduction

Design of efficient terahertz (THz) lasing devices is among major challenges of modern applied physics [107]. In recent decades there appeared several proposals for practical realization of THz emitters based on variety of materials and methods, covering the areas of gas lasers [108, 109], single-layer [110] and double-layer [111] graphene, photonic crystals [112], quantum cascade lasers [113, 114] and frequency conversion in nonlinear optical systems [115]. However, despite the significant progress achieved over the years, there are variety of fundamental technological problems yet to overcome. As a result, the goal of creation of tunable and stable THz laser source hitherto remains not achieved.

One of the possible routes to realize this goal is use of operating in the regime of strong light-matter coupling, for which the interaction between material part with light drastically modifies the properties of the matter itself. Striking examples of such systems are low dimensional semiconductor microcavities for which strong resonant coupling between confined photonic cavity mode and excitonic resonance in the active media gives rise to the appearance of the hybrid modes, referred as exciton polaritons [22]. Among the notable applications of polaritons are polariton lasers, which have certain advantages with respect to the conventional lasers, including extremely low

threshold and easy tunability [116]. Such devices can be realized in both bulk [117] and low-dimensional [118] geometries, the latter including planar [119] and pillar [120] systems together with photonic crystal cavities [121] and for broad variety of materials including wide gap semiconductors (for instance, GaN and ZnO) for which room temperature operation becomes feasible [28, 29, 30].

Upper and lower polariton states are separated in energy by the gap, which is usually of the order of magnitude of several meV for conventional semiconductor systems of tens of meV for wide bandgap semiconductors and organic materials. Radiative transitions between upper and lower polariton states, if possible, will thus generate emission in THz frequency range which can be enhanced by the effect of bosonic stimulation in the system. Unfortunately, direct implementation of this scenario faces the fundamental problem: optical transition between two polariton branches is forbidden due to the same parity of their wavefunctions. There are several attempts to overcome this obstacle which include the use of intersubband polaritons [122], bosonic cascade lasers in parabolic traps [123] and systems with asymmetric quantum wells [124, 125, 126, 127] for which dark exciton states of the different parity are admixed to upper and lower polariton modes and thus open radiative relaxation channel between them. However the mentioned proposals overcomplicate the system and make experimental realization challenging.

The concept of a polariton is closely related to a concept of electromagnetically dressed states (DSs). The latter appears in the systems placed in strong external laser field [46, 48]. Formation of the DSs was predicted and then experimentally observed in broad variety of the physical systems such as atomic systems [49] and solid-state setups, including bulk semiconductors [50, 51] and various mesoscopic structures [52, 53, 56, 57, 58, 59, 60, 61, 63, 64, 67, 68, 69]. Characteristic energy separating DSs is known as Rabi splitting. Differently from the case of cavity polaritons (where the similar parameter is also known as vacuum Rabi splitting) it depends on the intensity of the dressing field.

The possibility of the radiative transition between the states of electromagnetically dressed systems was previously predicted theoretically and later on observed in the experiments for atomic media [128, 129, 130, 131], condensed-matter structures [70, 71, 72], and superconducting circuits [132, 133, 134]. In this context the systems with broken inversion symmetry are of special interest. Formally, in such systems not only transversal (proportional to Pauli pseudospin operators σ^x and σ^y) but also longitudinal (proportional to σ^z operator characterizing popolation inversion) coupling with electromagnetic field becomes possible [135]. The latter opens radiative channel between adjacent dressed levels at Rabi frequency [136, 137, 74].

In semiconductor structures where light-matter interaction is sufficiently strong, Rabi splitting can easily reach values of several meV for moderate dressing field intensities, which can make them attractive candidates for realization of THz laser sources provided that one could find structures possessing broken inversion symmetry. Among the

promising candidates are asymmetric quantum dots (QDs) formed by semiconductor materials of wurtzite type (e.g. GaN QDs), for which giant piezoelectric effect was reported and static dipole momentum routinely appears [80, 81, 82, 83, 84, 85, 86]. The interaction of this build-in moment with external fields can lead to intriguing optical effects, such as dynamically controllable fluorescence spectra under bichromatic dressing field, found both experimentally [73] and theoretically [A5] and spontaneous emission at Rabi frequency [74, 75].

Capitalizing on our previous results on optical properties of individual QDs with broken inversion symmetry in the current paper we set a goal of construction of the dynamical theory of THz lasing in ensemble of asymmetric QDs dressed by intense optical field inside THz laser cavity. We adopt the method of creation of population inversion between dressed levels implying exploitation of spontaneous decay of an excited eigenstate of two-level system, cf. [130, 136, 131]. We also take into account the fact that systems of multiple QDs have certain problems with scalability. The main reason for that is significant inhomogeneous broadening of QD ensembles arising from imperfections of the fabrication process [138]. The values of inhomogeneous broadening can reach tens of meV what is larger than frequency of emitted THz radiation. This situation leads to the qualitative difference of our system and conventional lasers operating at optical frequencies. The presence of inhomogeneous broadening will certainly challenge the ability of practical realization of THz laser source based of asymmetric QDs. However, the performed numerical calculations let us conclude, that the proposed laser can still operate under realistic system parameters.

3.2. The model

We consider the system of N asymmetrical QDs placed in the planar THz cavity (Fig. 3.1(a)). The system is irradiated by intensive classical CW laser field $\vec{E}\cos(\omega_d t)$ with frequency ω_d close to the interband transition in considered QDs. Up-to-date technologies allow deposition of QDs with inter-dot separation about 30 nm (corresponds to surface density $\sim 10^{11}$ cm^{-2}) which is at least several times larger than the typical value of individual QD lateral size. Thus we treat each QD as an individual two level system with ground state $|g\rangle_\nu$ having all electrons in the valence band, and upper state $|e\rangle_\nu$, corresponding to the excitation of single electron-hole pair. We denote the inter-level separation energy as $\hbar\omega_{0\nu}$ (Fig. 3.1(b)), where subscript ν numerates QDs in the ensemble. Higher excited states are supposed to lie far from the resonances with the driving field. For the sake of simplicity we suppose driving laser field $\vec{E}$ to be linearly polarized and neglect polarization and spin degrees of freedom.

The generic Hamiltonian written in the basis of QDs eigenstates is

$$H = \sum_{\nu}^{N} \frac{\hbar\omega_{0\nu}}{2}\sigma_{\nu}^{z} + \sum_{\nu}^{N} \vec{E}\vec{d}_{\nu}\cos(\omega_d t) + \hbar\Omega_c a^{\dagger}a + \sum_{\nu}^{N} \vec{d}_{\nu}\vec{e}_c\sqrt{\frac{\hbar\Omega_c}{2\varepsilon_0 V_c}}(a + a^{\dagger}). \quad (3.1)$$

The first term is the Hamiltonian of the two level QDs, the second term describes coupling with external driving mode, the third term corresponds to the quantized photons of the THz cavity and the fourth term describes the coupling between THz photons and QDs. Here $\sigma_{\nu}^{z} = |e\rangle_{\nu}\langle e|_{\nu} - |g\rangle_{\nu}\langle g|_{\nu}$ is an operator of the population inversion written in the basis of the bare states of QDs. The quantity $\vec{d}_{\nu}$ corresponds to the dipole momentum operator, with non-diagonal elements describing the interband transition rates. They are determined by the material properties, and thus are equal for all QDs: $\vec{d}_{eg\nu} \equiv \vec{d}_{eg} = \vec{d}_{ge}$. The diagonal terms are absent in symmetric systems and emerge as a result of inversion symmetry breaking. In the structure we consider the asymmetry originates from giant piezoelectric effect, characteristic for III-nitride semiconductors. The latter gives rise to built-in electric field along the asymmetry axis, leading to spatial separation of an electron and a hole, and appearance of internal dipole momentum. For the ground state, when there are no free electrons in the system one can assume $\vec{d}_{gg\nu} = 0$, while for the excited state $\vec{d}_{ee\nu} \neq 0$, and depends on individual QD parameters.

The dipole operator $\vec{d}_{\nu}$ of the ν-th QD can be represented as

$$\vec{d}_{\nu} = \vec{d}_{ee\nu}\left(\mathbb{I}_{\nu} + \sigma_{\nu}^{z}\right)/2 + \vec{d}_{ge\nu}\left(\sigma_{\nu}^{+} + \sigma_{\nu}^{-}\right). \quad (3.2)$$

The Pauli raising and lowering operators acting in the space of ground and excited states of the individual dots read: $\sigma_{\nu}^{+} = |g\rangle_{\nu}\langle e|_{\nu}$ and $\sigma_{\nu}^{-} = |e\rangle_{\nu}\langle g|_{\nu}$, and $\mathbb{I}_{\nu} = |e\rangle_{\nu}\langle e|_{\nu} + |g\rangle_{\nu}\langle g|_{\nu}$ is a unitary operator.

The parameter Ω_c in the third term in Eq.(3.1) is resonant frequency of the THz cavity, V_c in the last term is cavity mode volume, ε_0 – is dielectric constant and $\vec{e}_c$ is polarization vector of the THz cavity mode. In order to achieve efficient THz lasing one should maximize interaction strength between QDs and THz photons and minimize the losses. Appropriate candidates which comply with both of these requirements are planar photonic crystal slabs, schematically depicted in Fig. 3.1(a). Such cavities possess both high Q-factors (up to 10^4 in the best samples [139]) and allow tight confinement of THz field. The mode volume in this case can be approximated by $V_c \sim (\lambda_c/2)^3 = \pi^3 c^3/\Omega_c^3$. Another possible alternative is plasmonic THz cavities which demonstrate subwavelength confinement in one direction dramatically reducing mode volume. However this usually costs the loss of Q-factor which is at best of the order of tens in such structures [140, 141].

The Hamiltonian (3.1) contains time-dependence in an explicit form. In order to eliminate quickly oscillating terms we perform the unitary transformation $U_R = \exp(i\omega_d/2\sum_{\nu}\sigma_{\nu}^{z}\cdot t)$, corresponding to the transition to the frame rotating with driving frequency ω_d, according to $\tilde{H} = U_R H U_R^{\dagger} + i\hbar\dot{U}_R U_R^{\dagger}$. Applying the rotating wave approximation and

thus omitting quickly oscillating terms containing factors $\exp(\pm i\omega_d t)$ and $\exp(\pm 2i\omega_d t)$, we arrive at the simple stationary Hamiltonian:

$$H_{RWA} = -\sum_{\nu}^{N} \frac{\hbar\Delta_\nu}{2}\sigma_\nu^z + \sum_{\nu}^{N} \frac{\hbar\Omega}{2}\left(\sigma_\nu^+ + \sigma_\nu^-\right) + \\ + \hbar\Omega_c a^\dagger a + \sum_{\nu}^{N} \frac{\hbar\chi_\nu}{2}\left(\mathbb{1}_\nu + \sigma_\nu^z\right)\left(a + a^\dagger\right), \quad (3.3)$$

where $\Delta_\nu = \omega_d - \omega_{0\nu}$ and $\Omega = \vec{E}\vec{d}_{ge}/\hbar$ corresponds to the Rabi splitting. Note that within rotating wave approximation the latter is determined by *transversal* coupling between QD and driving field only. Additionally, the dipole matrix element $\vec{d}_{ge}$ has an induced character and in fact is always parallel to the excited field. Thus the value of Rabi splitting does not depend on the orientation of driving field polarization.

On the contrary, the strength of the interaction with THz cavity mode, $\chi_\nu = \vec{d}_{ee\nu} \cdot \vec{e}_c\sqrt{\frac{\Omega_c}{2\varepsilon_0\hbar V_c}}$, does depend on the mutual orientation of the cavity mode polarization $\vec{e}_c$ and stationary dipole moment $\vec{d}_{ee\nu}$ whose direction is determined by the symmetry of the system. Note, that if stationary dipoles of QDs in the ensemble are oriented chaotically the overall interaction with the cavity mode will be suppressed. Fortunately, modern techologies allow growing QDs along the polar [0001] axis of the wurtzite GaN structure. It guaranties that all permanent dipoles are directed perpendicular to the plane of the substrate.

Since the value of the stationary dipole moment is determined by the size of QD, the absolute values of $|\chi_\nu|$ are distributed normally around some average value. Besides the values of χ_ν should differ by phase factors. We suppose that when the macroscopic polarization of the medium is set by the lasing process (Sec. IV), all the emitters are synchronized. This assumption looks reasonable in the case when QDs ensemble is localized in the region where variation of the cavity mode intensity is negligibly small – cf. with [130].

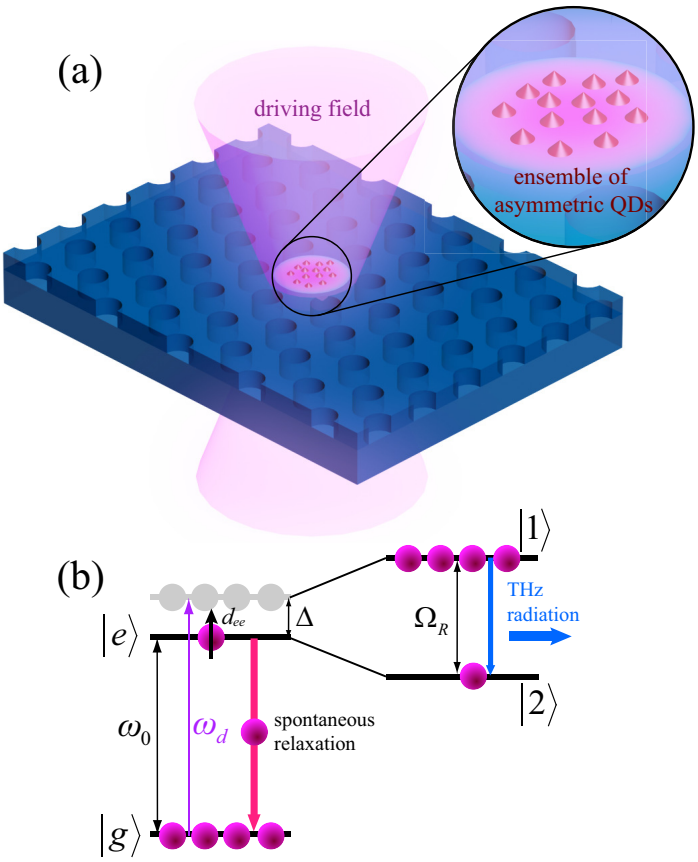

Figure 3.1: (Color online) Sketch of the system under consideration. (a) – terahertz cavity (photonic crystal slab) containing an ensemble of N asymmetric QDs. The system is interacting with the optical driving field with frequency close to the resonance with QDs interband transition. (b) – schematic illustration of (i) energy levels of an individual QD and (ii) energy states of electromagnetically dressed QD in the presence of blue detuned driving field, $\Delta > 0$, with variable intensity. The population inversion in DS basis emerges due to spontaneous relaxation processes which occur in QD eigenstate basis (see main text for details).

3.3. Maxwell-Bloch-like laser equations in the DS basis

In the presence of an intense driving field bare states of QDs become optically dressed. It leads to the formation of the Rabi doublet consisting of the energy eigenstates of the sub-system "ν-th QD + driving field" which can be denoted as upper $|1\rangle_\nu$ and lower $|2\rangle_\nu$ dressed states (DSs). The Hamiltonian of the system written in the basis of DS basis can be obtained by means of rotation in pseudospin space with unitary operator $U_d = \exp\left[i\sum_\nu \theta_\nu \sigma_\nu^y\right]$, where $\sigma_\nu^y = i(\sigma_\nu^- - \sigma_\nu^+)$ and the rotation angles are determined from the condition $\tan 2\theta_\nu = -\Omega/\Delta_\nu$. This gives:

$$H^{DS} = \sum_\nu^N \frac{\hbar\Omega_{R\nu}}{2}\sigma_\nu^z + \hbar\Omega_c a^\dagger a + (a + a^\dagger)\times \sum_\nu^N \frac{\hbar\chi_\nu}{2}\left[\not{\mathrm{K}}_\nu + \cos(2\theta_\nu)\sigma_\nu^z - \sin(2\theta_\nu)(\sigma_\nu^+ + \sigma_\nu^-)\right], \quad (3.4)$$

where $\sigma^{z,\pm}$ acts now in the space of the Rabi doublet states (see Fig. 3.1(b))

$$|1\rangle_\nu = \sin\theta_\nu|g\rangle_\nu + \cos\theta_\nu|e\rangle_\nu, \quad (3.5a)$$
$$|2\rangle_\nu = \cos\theta_\nu|g\rangle_\nu - \sin\theta_\nu|e\rangle_\nu. \quad (3.5b)$$

and $\Omega_{R\nu} = \sqrt{\Delta_\nu^2 + \Omega^2}$. It is clearly seen from the Hamiltonian (3.4) that the presence of the stationary dipole ($\chi_\nu \sim d_{ee\nu} \neq 0$) allows energy exchange between the dressed QD states and the cavity mode.

Further consideration of the THz emission needs accounting for the spontaneous processes which play crucial role in lasing and, as it will be shown later, also play role of the effective pump in the considered system. For this purpose we use master equation approach for the density matrix of the system ϱ

$$\dot{\varrho} = -\frac{i}{\hbar}[H^{DS}, \varrho] + L^R\varrho + L^C\varrho. \quad (3.6)$$

The term

$$L^R\varrho = \Gamma\sum_\nu^N \sigma_\nu^-\varrho\sigma_\nu^+ - \frac{1}{2}\left(\sigma_\nu^+\sigma_\nu^-\varrho + \varrho\sigma_\nu^+\sigma_\nu^-\right) \quad (3.7)$$

describes the radiative decay of QD excitations with rate Γ (supposed to be identical for all QDs).

The term

$$L^C\sigma = \Gamma_c\left(2a\varrho a^\dagger - a^\dagger\varrho a - \varrho a^\dagger a\right) \quad (3.8)$$

is responsible for the THz cavity mode net damping with rate Γ_c related to the cavity Q-factor, $Q = \Omega_c/2\Gamma_c$.

To analyze the dynamics of the system we use mean-field approximation, which means that all the mean values of the products of the operators are factorized into products of their mean values, $\langle AB\rangle = \langle A\rangle\langle B\rangle$. To account for the inhomogeneous broadening provided by variations in the Rabi splittings $\Omega_{R\nu}$ and couplings to THz mode χ_ν for each QD we write down individual equations for all QDs in the ensemble introducing averaged values of DS spinor operators $S_\nu = \langle\sigma_\nu^-\rangle$, $S_\nu^* = \langle\sigma_\nu^+\rangle$ and $S_{z\nu} = \langle\sigma_\nu^z\rangle$. The corresponding system of Maxwell-Bloch type equations for the ensemble of N individual QDs interacting with single THz cavity mode characterized by complex amplitude $\alpha = \langle a\rangle$ reads:

$$\dot{\alpha} = i\sum_{\nu}^{N}\kappa_\nu S_\nu - i\Omega_c\alpha - \Gamma_c\alpha, \tag{3.9a}$$

$$\dot{S}_\nu = -i\kappa_\nu S_{z\nu}\alpha - i\Omega_{R\nu}S_\nu - \Gamma_{d\nu}S_\nu, \tag{3.9b}$$

$$\dot{S}_{z\nu} = 2i\kappa_\nu(S_\nu^*\alpha - S_\nu\alpha^*) - \Gamma_{z\nu}S_{z\nu} + \Gamma_{s\nu}. \tag{3.9c}$$

Here $\kappa_\nu = \chi_\nu\Omega\,/2\Omega_{R\nu}$ is an effective strength of the coupling between THz cavity mode and ν-th dressed QD. This is key parameter determining the efficiency of THz lasing in our system. The parameter

$$\Gamma_{d\nu} = \Gamma\left(\frac{\Omega^2}{4\Omega_{R\nu}^2} + \frac{1}{2}\right) \tag{3.10}$$

in (3.9b) is effective dephasing rate responsible for the relaxation of DS polarization S_ν.

The impact of the spontaneous processes on the population inversion $S_{z\nu}$ of Rabi levels in the Eq. (3.9c) is twofold. First, it contributes to the relaxation from the excited state to the ground state with the rate

$$\Gamma_{z\nu} = \frac{\Gamma}{2}\left(1 + \frac{\Delta_\nu^2}{\Omega_{R\nu}^2}\right). \tag{3.11}$$

Besides, spontaneous transitions between bare states $|e\rangle_\nu$ and $|g\rangle_\nu$ also feed populations of both Rabi levels (see definitions (3.5)). This is reflected in the last term of (3.9c), $\Gamma_{s\nu} = \Gamma\Delta_\nu\,/\Omega_{R\nu}$, which plays a role of pumping or dissipation for DS population inversion $S_{z\nu}$ depending on which of the Rabi states, upper or lower, is pumped more efficiently.

If the amplitude of cavity mode is negligibly small ($\alpha \approx 0$) (e.g. at the start of the lasing), the populations of the Rabi levels are governed by the relaxation processes only. In this case the population inversion for ν-th QD approaches stationary level which reads:

$$S_{z\nu}^{st} = \frac{2\Delta_\nu}{\Omega_{R\nu}}\left(1 + \frac{\Delta_\nu^2}{\Omega_{R\nu}^2}\right)^{-1}. \tag{3.12}$$

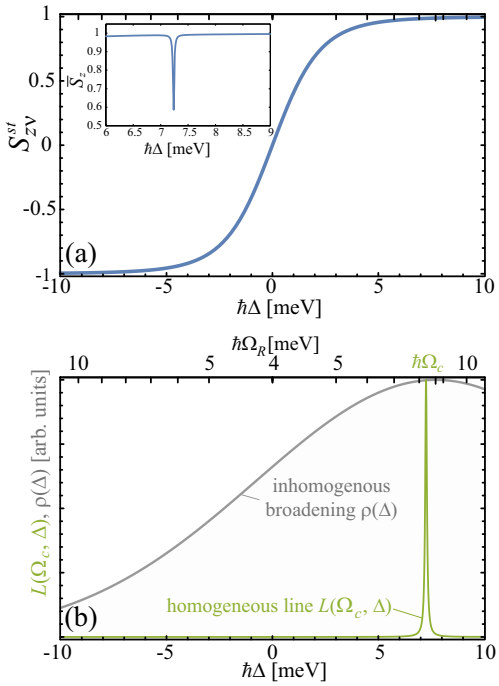

Figure 3.2: (Color online) (a) – population inversion of dressed QD in the absence of THz field ($\alpha = 0$). Blue line is determined by Eq. (3.12) for $\hbar\Omega = 4$ meV. The position of cavity frequency corresponds to $\Omega_c/2\pi = 2$ THz. In the inset the profile of spectral density of population inversion $\bar{S}_z$ in the presence of lasing is shown. The curve corresponds to the profile along vertical dashed line in Fig. 3.5(b). (b) – spectral distribution of QDs governed by spectral density $\rho(\Delta)$ (gray curve). Green curve corresponds to homogeneous line $L(\Omega_c, \Delta)$ which width was multiplied by 50 for illustrativeness. The upper axis shows the corresponding values of Rabi splitting.

From this equation it is clearly seen that when driving field is blue-detuned from the QD, i.e. $\Delta_\nu > 0$, the term $\Gamma_{s\nu}$ acts as an effective pump and the population inversion in the DS basis establishes, $S^{st}_{z\nu} > 0$ (see Fig. 3.2(b)). That is, incoherent processes of spontaneous relaxation occurring in the QD bare state basis not only deteriorate DS lasing due to the relaxation of DS polarization S_ν but also favor DS population inversion $S_{z\nu} > 0$ which is necessary prerequisite for the lasing. The sketch of this processes is shown in Fig. 3.1b. Note that the similar pumping mechanism was intensively investigated both theoretically and experimentally in atomic gases [128, 129, 130, 131] and in superconductor quantum circuits [132, 133, 134].

It is important to note that the presented analysis doesn't take into account the interaction with a phonon bath [142] which drives the system to thermodynamic equilibrium where the populations of the Rabi levels are $S_{z\nu} = -\tanh\left[\hbar\Omega_{R\nu}/2k_BT\right] < 0$ – see

[142, 143]. The discussed effect of spontaneous relaxation-induced population inversion will thus occur only if the rate of DS thermalization due to the interaction with the phonon bath is slower than $\Gamma_{s\nu}$, which is only possible if the lattice temperature T in the system is sufficiently low and excited state lifetime Γ^{-1} is short enough to overcome quick phonon assisted relaxation. In our calculations we take $\Gamma = 0.02$ ps^{-1}. Such condition can be reached in the small QDs for which the overlap integral between electron and hole wave functions is high enough. This leads to the high decay rate of the excited state [144] which allows quick gain of the DS inversion.

3.4. Terahertz lasing in dressed quantum dots ensemble

3.4.1. Inhomogeneous ensemble of QDs

Due to technical reasons it is extremely difficult to fabricate a large amount of identical QDs. In real samples QDs sizes always vary over a wide range. As a result the main parameters characterizing individual QD such as interband transition frequency $\omega_{0\nu}$ and the value of permanent dipole $d_{ee\nu}$ are distributed normally in the ensemble. This leads to the inhomogeneous broadening of the QD frequency $\omega_{0\nu}$ (and the detuning Δ_ν from driving field as a consequence). The typical values of the full width at half-maximum (FWHM) of this distribution are of the order of tens of meV [145, 146].

We attribute inhomogeneous broadening of the interband transition to the size quantization energy $\hbar\omega_{q_\nu} = \hbar\omega_{0\nu} - E_g$, where E_g denotes the semiconductor bandgap. Without loss of generality we can use the following estimate: $\hbar\omega_{q_\nu} \approx \hbar^2 / 2\mu l_\nu^2$, where $\mu \approx 0.1 m_0$, with m_0 denotes free electron mass. Here l_ν is the size of ν-th QD. Let us suppose that the values of l_ν are distributed around mean value l_0. Assuming that the inhomogeneous width is much smaller than ω_{q_ν}, which is reasonable for small QDs (l_ν of order of nanometers) we can approximate the interband transition frequency by linear function of QD size: $\omega_{q_\nu} \simeq \bar{\omega}_q(1 - 2(l_\nu - l_0)/l_0)$, where $\bar{\omega}_q = \hbar / 2\mu l_0^2$. This gives for the detunings: $\Delta_\nu = \Delta_0 + \delta_\nu$, where $\delta_\nu = 2\bar{\omega}_q (l_\nu - l_0)/l_0$ is the deviation of the interband transition frequency of ν-th QD from the corresponding ensemble averaged value Δ_0.

The magnitude of the static dipole moment $d_{ee\nu}$ is proportional to electron-hole separation can also be supposed to depend linearly on the QD size l_ν, which allows to write the following estimate for the coupling strength with THz cavity mode: (see. Eq. (3.3) and comments below it): $\chi_\nu = \chi_0(1 + (l_\nu - l_0)/l_0) = \chi_0(1 + \delta_\nu / 2\bar{\omega}_q)$, where χ_0 is ensemble averaged value. Our results demonstrate that generally effects of the broadening in the stationary dipole moments have a minor effect in comparison with inhomogeneous broadening of the interband transition. However both of them were

accounted for in the calculation.

3.4.2. The net gain from QDs ensemble

The effect of lasing occurs when regime of positive feedback establishes in the active media and amplification of the cavity field provided by ensemble of emitters exceeds the losses. In the ideal situation all emitters should be equivalent. However, even in the case when inhomogeneous broadening is present all emitters will contribute to the filling of the cavity mode although their contribution is not equivalent.

In order to derive the net gain for the THz field in the system we adiabatically eliminate variables corresponding to QDs subsystem from Eqs. (3.9). For that we use the substitution $S_\nu(t) = S_\nu e^{-i\Omega_c t}$ in Eq. (3.9b) thus supposing that the lasing occurs at eigenfrequency of THz cavity. Note, that in the general case the frequency of lasing is not exactly equal to the cavity frequency Ω_c due to the frequency pulling effect. However in the case of large inhomogeneous broadening this effect is negligible (see [147]). For the occupancy of the cavity mode we get:

$$\frac{\partial |\alpha|^2}{\partial t} = \left(\sum_\nu^N g_\nu(|\alpha|^2, \Delta_\nu) - 2\Gamma_c \right) |\alpha|^2 , \tag{3.13}$$

where the effective gain from individual ν-th QD is given by

$$g_\nu(|\alpha|^2, \Delta_\nu) = \frac{2\kappa_\nu^2 \Gamma_{s\nu}}{\Gamma_{z\nu}} \frac{L_\nu(\Omega_c)}{1 + 4\kappa_\nu^2 |\alpha|^2 L_\nu(\Omega_c)/\Gamma_{z\nu}} \tag{3.14}$$

and the homogeneous line shape of DS transition is

$$L_\nu(\omega) = \frac{\Gamma_{d\nu}}{\Gamma_{d\nu}^2 + (\Omega_{R\nu} - \omega)^2}, \tag{3.15}$$

where $\Gamma_{d\nu}$ is polarization dephasing rate.

Note that adiabatical elimination of QD's variables performed above is justified in the limit of $\Gamma_{d\nu}, \Gamma_{z\nu} \gg \Gamma_c$, when the dissipation in QD subsystem dominates over cavity loss rate [132]. In the system under consideration those QDs which effectively interact with THz field are characterized by large positive detunings Δ_ν. In this case both $\Gamma_{d\nu}$ and $\Gamma_{z\nu}$ are of order of $\Gamma/2$. Thus the adiabaticity condition is satisfied in the case of good enough THz cavity, for which $\Gamma_c \ll \Gamma$, i.e. with Q-factor about 10^3 and more for used parameters.

To derive the total gain from whole QD ensemble we assume that the number of QDs is so large and continous approximation can be done. Thus we replace summation over distinct QDs in (3.13) with integration over QD transition frequency in the rotating

frame using the substitution $\sum_\nu^N \to \int \rho(\Delta)d\Delta$, where for the spectral density $\rho(\Delta)$ of QDs we take the Gaussian distribution

$$\rho(\Delta) = \frac{N}{\sqrt{2\pi}\xi} \exp\left[-\frac{(\Delta-\Delta_0)^2}{2\xi^2}\right] \tag{3.16}$$

with FWHM equal to $2\sqrt{2\ln(2)}\xi$. For the net gain of THz field $G = \sum_\nu^N g_\nu(|\alpha|^2)$ we get this way:

$$G = \frac{N}{\sqrt{2\pi}\xi} \int_{-\infty}^{+\infty} g(|\alpha|^2, \Delta) \exp\left[-\frac{(\Delta-\Delta_0)^2}{2\xi^2}\right] d\Delta. \tag{3.17}$$

Where all parameters which were labeled with subscript ν heretofore, are now functions of the detuning Δ, i.e. $\kappa \equiv \kappa(\Delta)$, $\Omega_R \equiv \Omega_R(\Delta)$, $L_\nu(\omega) \equiv L(\omega, \Delta)$ etc.

3.4.3. DS laser conditions

The term containing THz mode occupancy $|\alpha|^2$ in the denominator of Eq. (3.14) is responsible for the saturation of DS inversion and leads to the depletion of the gain. If we aim at obtaining the amplification condition we can neglect this term as lasing starts when $|\alpha|^2 \approx 0$. So, if the condition

$$G(|\alpha|^2 = 0) > 2\Gamma_c \tag{3.18}$$

is satisfied (see Eq. (3.13)), any fluctuation of the the cavity field grows and lasing occurs. Fulfillment of this condition is determined by several independent parameters of the system.

First of all, cavity with high quality-factor Q is necessary. Second, the number of QDs effectively interacting with THz mode should be maximized. According to Eq. (3.14) the gain is substantial only for those QDs which DS splitting $\Omega_{R\nu}$ is close to THz cavity eigenfrequency Ω_c, i.e. lies within the homogeneous profile $L(\omega)$ centered around Ω_c – see green curve in Fig. 3.2b. However the number of QDs belonging to this domain is rather low because the value of inhomogeneous broadening is big. The shape of inhomogeneous broadening is shown by gray curve in Fig. 3.2b. As a result a minor part of the whole amount of QDs in the ensemble effectively contributes to amplification of the cavity field. Analogously to Eq. (3.17) we can estimate this value as $N_{\text{eff}} = \int_{-\infty}^{\infty} \Gamma_d L(\Omega_c, \Delta)\rho(\Delta)d\Delta$. For inhomogeneous broadening parameter $\hbar\xi = 5$ meV which corresponds to FWHM about 14 meV we obtain $N_{\text{eff}}/N \sim 10^{-3}$.

Hence, in order to maximize gain one needs, firstly, to engineer properly the QD ensemble (or take the cavity with the specific frequency Ω_c) in such a way that maximum of inhomogeneous distribution of Rabi splitting $\Omega_{R\nu}$ coincides with Ω_c, see Fig. 3.2b. Besides, it is necessary to use dense QDs ensembles. The value of surface density n_{qd}

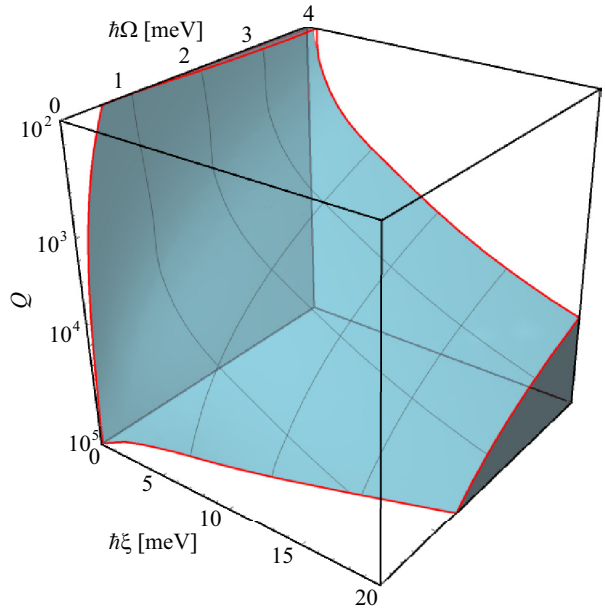

Figure 3.3: (Color online) The domain of existence of lasing in the parameter space of cavity Q-factor, inhomogeneous broadening width ξ and resonant Rabi splitting Ω. The remaining parameters are: $\Omega_c/2\pi = 2$ THz, $n_{qd} = 10^{13}$ cm^{-2}, $d_{eg} = 10$ D, $\Gamma = 0.02$ ps^{-1}, $\chi_0 = 3.16 \cdot 10^{-5}$ ps^{-1} (corresponds to the ensemble averaged value of permanent dipole moment $d_{ee} = 75$ D [85]). At the each point value of average detuning Δ_0 is chosen in such a way that the condition of resonance, $\Omega_c = \Omega_{R0} = \sqrt{\Delta_0^2 + \Omega^2}$, is hold.

of QDs fabricated by epitaxy method is limited by 10^{11} cm^{-2} [148]. We expect that consistent depositions of QDs in several vertical stacked layers (cf. with [149, 150]) can allow to increase this value by at least an order of magnitude.

Next, the key parameter, which can be easily tuned experimentally, is the intensity of driving field proportional to resonant Rabi splitting Ω. The latter explicitly determines the strength of dressed QD-cavity field interaction κ and also main parameters of the DS dynamics, such as Γ_d, Γ_s and Γ_z – see Eqs. (3.9). Consequently, driving field affects the gain properties of dressed QDs in rather nontrivial way.

In order to reveal the role of the most important parameters of the system we plot the phase diagram in the parameter space of (Q, ξ, Ω) (Fig. 3.3). The region inside the blue domain corresponds to self-amplification of THz cavity field, i.e. condition (3.18) is satisfied. One can easily recognize that lasing in strongly inhomogeneously broadened ensemble demands both high Q-factor of THz cavity (up to 10^4) and high intensity of the driving field. The first condition although represents a challenge for practical implementation, is nevertheless reachable in photonic crystal slabs [139].

The requirement of strong driving fields on the other hand involves certain practical obstacles. The analysis of the complicated dependence of the unsaturated net gain $G(|\alpha|^2 = 0)$ on the resonant Rabi splitting Ω, given by Eqs. (3.14) and (3.17), reveals that the most appropriate conditions for lasing is achieved for a high values of Ω which are close to Ω_c, see Fig. 3.4(a). This is valid for a wide range of values of inhomogeneous broadening as it is illustrated on the inset to Fig. 3.4(a) where the position of the maximum of the net gain is shown. Thus one needs to use high intensities of dressing laser to provide efficient gain of THz mode. For realistic values of ξ and Q the necessary resonant Rabi splitting $\hbar\Omega$ should be of the order of meV. For the typical value of off-diagonal dipole moment for GaN QDs, which is $d_{eg} = 10$ D [151], such splitting corresponds to the driving laser intensities in the diapason of MW/cm^2. Such intensities in the case of CW laser excitation would inevitably lead to melting of a sample. Thus pulsed excitation is the only possible way to reach THz lasing in a system under consideration.

3.4.4. Properties of DS lasing

One of the most important output characteristics of every light source is intensity, i.e. the number of emitted photons per unit time. In our case it is proportional to the occupancy of THz cavity mode $|\alpha|^2$. Let us consider first the case of quasi-CW-regime corresponding to the excitation by a rectangular pulse. In this simplest case it is possible to estimate the maximum value of $|\alpha|^2$ which achieved in the steady-state regime when saturated gain is equalized by losses, i.e. when condition

$$G\left(|\alpha|^2\right) = 2\Gamma_c \tag{3.19}$$

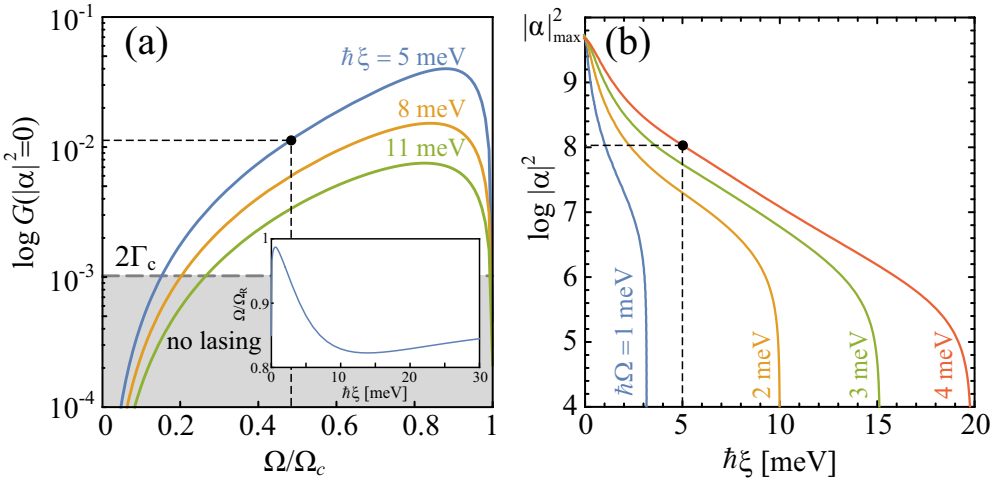

Figure 3.4: (Color online) Properties of the THz lasing. (a) – dependence of the unsaturated net gain $G(|\alpha|^2 = 0)$ on the resonant Rabi splitting for different values of inhomogeneous broadening. For all curves the maximum of spectral distribution of QDs coincides with cavity mode frequency $\Omega_c/2\pi = 2$ THz. Gray dashed line corresponds to the cavity loss rate. Below this line lasing can not occur. In the inset the value of resonant Rabi splitting corresponding of maximal gain vs inhomogeneous broadening parameter ξ is shown. (b) – dependence of the occupancy of tha THz cavity mode on the value of inhomogeneous broadening for different resonant Rabi splittings $\hbar\Omega$. For both panels $\Gamma_c = 1/2000\ ps^{-1}$. Other values are the same as for the Fig. 3.3. Black points label parameters corresponding to Fig. 3.5

is satisfied. The THz cavity occupancy can be obtained from the solutions of transcendental equation (3.19).

In the Fig. 3.4(b) dependence of the value of $|\alpha|^2$ vs the inhomogeneous broadening parameter ξ is shown for different values of resonant Rabi splitting Ω. As expected, with increase of inhomogeneous broadening the amplitude of cavity field drops since the number of QDs N_{eff} effectively participating in lasing, decreases. Evidently, the maximum possible value of THz laser intensity corresponds to idealized homogeneous system of N identical QDs with Rabi splitting Ω_R being in resonance with THz cavity mode Ω_c. This value can be obtained from the steady state solution of the full set of Eqs. (3.9), assuming that all parameters are independent on ν (cf. with [131]):

$$|\alpha|^2_{\max} = \frac{\Gamma_s}{4\Gamma_c} - \frac{\Gamma_z \Gamma_d}{4\kappa^2 N}. \tag{3.20}$$

Since the values shown in Fig. 3.4(b) correspond to the steady state regime, they are reachable if driving pulse is long enough. The necessary duration of the driving pulse

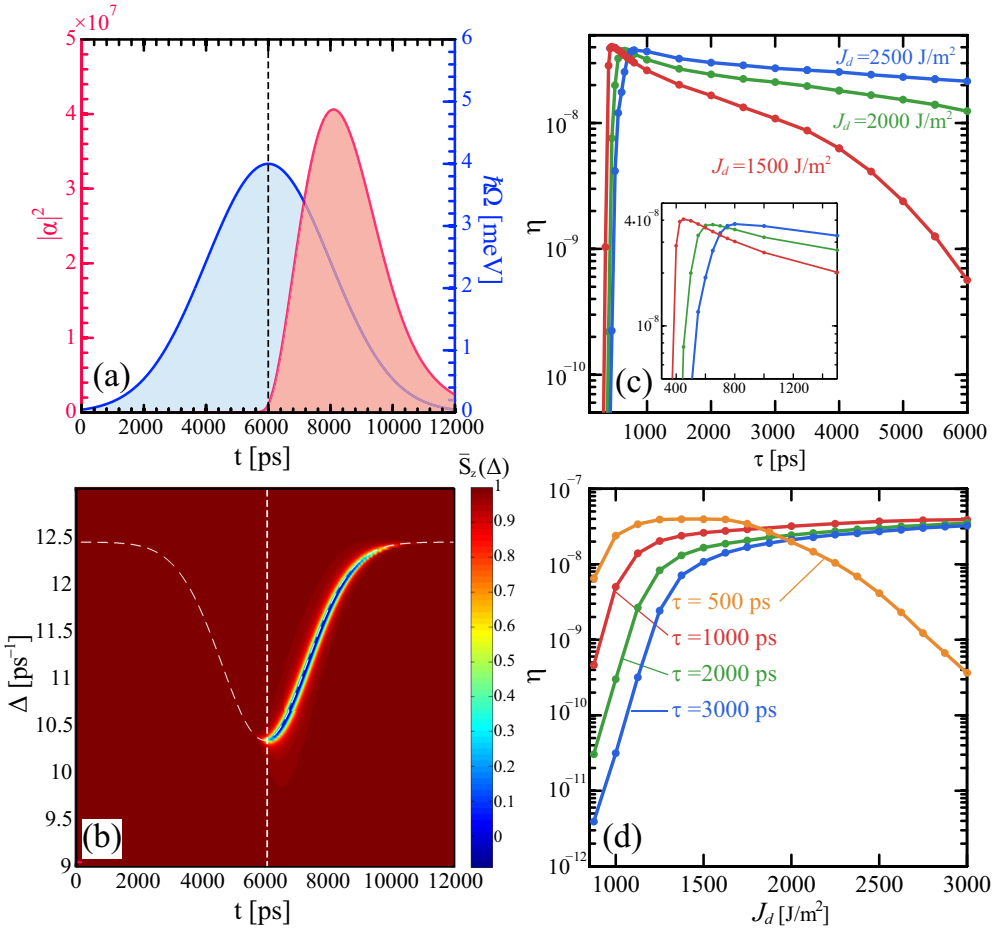

Figure 3.5: (Color online) Pulse dynamics of the THz laser. (a) – time dependence of THz photon number $|\alpha|^2$ (red curve, left axis). The magnitude of resonant Rabi splitting $\hbar\Omega(t)$ is shown with blue curve (right axis). Initial conditions: $S_{z\nu} = S^{st}_{z\nu}$, $S = 0$, population of cavity mode α corresponds to the thermal occupation under $T = 30$ K. THz cavity frequency is $\Omega_c/2\pi = 2$ THz. (b) – dynamics of the spectral density of DS population inversion $\bar{S}_z(\Delta)$. Spectral position of QDs participating in lasing being currently in resonance with THz cavity mode, $\Omega_{R\nu}(t) = \Omega_c$, is shown with white dashed curve. (c) – dependence of the quantum efficiency η on duration of the gaussian driving pulse τ for three different fixed values of total energy (per unit area) accumulated in the pulse. In the inset the domain of short pulses is magnified. (d) – the same as in panel (c) but for fixed τ and varying energy density J_d.

can be estimated from Eq. (3.13) supposing that the gain G remains unsaturated until $|\alpha|^2$ reaches its stationary value. For instance, if $\hbar\Omega = 4$ meV and $\hbar\xi = 5$ meV (black points in Fig. 3.4(a) and (b)) this rough estimate gives for pulse duration the value about 2 ns. Consequently, operation in nanosecond regime is most appropriate for the considered THz laser source.

According to Fig. 3.4(b) for every given driving field intensity some critical value of ξ exists above which lasing is impossible to achieve. The bigger is the value of Ω the wider is the region where steady-state lasing is possible. For parameters under consideration the Rabi splitting of about $\hbar\Omega = 2$ meV is enough to obtain lasing for $\hbar\xi = 5$ meV what corresponds to the typical value of FWHM of inhomogeneous broadening about 14 meV. However larger values of driving intensity yield much better output laser characteristics.

3.4.5. Generation of THz laser pulses

The mostly realistic case corresponds to the excitation of a QD ensemble by a pulse of driving field having Gaussian time profile. In this case complete information about output laser characteristics can be extracted from the numerical solution of the Eqs. (3.9).

In order to simulate dynamics of a huge number of different QDs participating in lasing we discretize spectral distribution of QDs over finite number of domains which are small enough to consider all QDs belonging to the single domain as identical and characterize them by only couple of equations (3.9b) and (3.9c). Then for summation in (3.9a) we multiply the values of S_ν by corresponding weighting coefficients which are equal to the number of QDs in ν-th domain.

We also add to the rhs of Eq (3.9a) the Langevin term $\zeta(t)$ accounting for the fluctuations due to thermal noise and necessary to switch on the lasing. We suppose that $\langle\zeta(t)\zeta^*(t')\rangle = 2\Gamma_c N_{\text{th}}\delta(t-t')$, where N_{th} is a thermal occupation of the cavity mode.

Formation of the THz laser pulse induced by the gaussian pulse of the driving field with amplitude $E = E_0 \exp\left[-(t-t_0)^2/2\tau^2\right]$ and duration $\tau = 2$ ns is shown in Fig. 3.5(a). The intensity of THz radiation emitted from the area $S = \pi\lambda_c^2/16$ is determined as $I_{\text{THz}}(t) = 8\Gamma_c|\alpha|^2\hbar\Omega_c^3/\pi^3c^2$. Thus the total energy density accumulated in the THz pulse $J_{\text{THz}} = \int I_{\text{THz}}(t)dt$ is about $9\cdot10^{-6}$ J/m^2 for the case shown in Fig. 3.5(a). At the same time the energy density in the pulse of driving field is $J_d \simeq 1.7\cdot10^3$ J/m^2. It allows to expect the typical value of the quantum efficiency (the ratio of emitted THz photons $N_{\text{THz}} = J_{\text{THz}}S/(\hbar\Omega_c)$ to number of optical photons $N_d = J_dS/(\hbar\omega_d)$ in the driving pulse) of proposed THz laser source $\eta = N_{\text{THz}}/N_d$ of the order of 10^{-5} to 10^{-6}.

The more detailed analysis demonstrates that the exact value of quantum efficiency η

is determined by the parameters of the driving pulse. Because of the purely dynamical nature of the onset of the lasing even for fixed driving energy density J_d an output THz energy J_{THz} varies with duration τ of the pulse. Multiple solution of Eqs. (3.9) for fixed J_d shows that quantum efficiency η and therefore output THz energy reduces with the increase of pulse duration – see Fig. 3.5(c).

The best values of η are possible to achieve with sub-nanosecond pulses, corresponding to large resonant Rabi splittings Ω. It confirms our conclusion that higher gain is obtained for Ω which is close (but not exactly equals) to Ω_c– see Fig. 3.4(a). However the efficiency dramatically reduces with further decrease of pulse duration (up to few hundreds of picosecond) – see inset to Fig. 3.5(c). It is because the amplitude of $\Omega(t)$ is higher than the lasing frequency for these pulses. Hence condition of resonance between QDs and the cavity is not satisfied continuously during the action of driving field and the total amplification of THz field diminishes.

The similar decline of quantum efficiency occurs for low-energy pulses (small J_d) when Ω is small and THz gain is too low – see Fig. 3.5(d). At the same time the appropriate values of driving energy densities J_d are limited by the effect described above which prevents the use of too short or too high-energy pulses [see curve corresponding to $\tau = 500$ ps in Fig. 3.5(d) which falls down for $J_d > 1500$ J/m^2]. So the optimal values of J_d are about units of kJ/m^2.

Amplification of THz mode is accompanied with reduction of DS inversion which is connected with transfer of the excitation from the sub-system of dressed QDs to the THz field. Behaviour of the QDs sub-system can be illustrated by spectral density of inversion of dressed QDs determined as:

$$\bar{S}_z(\Delta) = \frac{\int_{\Delta}^{\Delta+d\Delta} S_z(\delta)\rho(\delta)d\delta}{\int_{\Delta}^{\Delta+d\Delta} \rho(\delta)d\delta}. \tag{3.21}$$

Time dynamics of $\bar{S}_z(\Delta)$ is shown in Fig. 3.5(b). When THz field increases substantially the gap forms in the distribution of the population inversion. Corresponding spectral profile of $\bar{S}_z(\Delta)$ at the moment when driving field reaches its maximum (vertical dashed line in Fig. 3.5(b)) is shown in the inset to Fig. 3.2. This phenomenon is also known as a spectral hole burning effect. The specific shape of this hole in our case indicates that different QDs effectively contribute to the lasing in different moments. Actually, since the value of Rabi splitting $\Omega_{R\nu}$ varies with time in our case the spectral position of QDs which satisfy the condition of maximal gain, $\Omega_{R\nu} = \Omega_c$, is also changes in time – see white dashed curve in Fig. 3.5(b).

This trajectory coincides with the region of DS inversion depletion. Thus using pulses with varying intensity allows increasing the number of QDs involved in lasing in comparison with the case of quasi-cw driving field.

It is important to emphasize that the discussed mechanism of THz radiation emission can be also described in terms of inelastic scattering of an optical photon accompanied with creation of THz quantum. Actually, DS population inversion $\bar{S}_{z\nu} > 0$ implies positive detunings $\Delta_\nu > 0$ – see Eq. (3.12). According to definitions (3.5) in the case of large Δ_ν the upper DS $|1\rangle_\nu$ represents a mixture of a major part of the QD ground state $|g\rangle_\nu$ and a tiny amount of the excited state $|e\rangle_\nu$. Thus in the absence of THz photons these QDs are in the state close to ground state $|g\rangle_\nu$ since they are far detuned from driving field and can hardly absorb it.

However the increase of the THz cavity occupancy during the onset of the lasing enables absorption of the driving field by those QDs for which $\Delta_\nu > 0$. QDs switch from the upper to the lower DS emitting THz photon. In the QD eigenbasis this corresponds to the excitation of the upper level $|e\rangle_\nu$ by absorption of the driving field. However the frequency of the driving field exceeds the frequency of the interband transition of these QDs. Hence the excess of energy should be transferred to the THz mode which is not empty now and amplify such relaxation by the effect of bosonic stimulation. Note that this process becomes possible only due to the presence of the stationary dipoles of asymmetric QDs. The effect of such inelastic scattering of the driving field should always occur during interaction of light with two-level system with broken inversion symmetry [76]. However in our case its efficiency is increased by the presence of THz cavity.

3.5. Conclusion

In conclusion, we present the theoretical study of an ensemble of asymmetric QDs embedded into terahertz cavity and dressed by external electromagnetic field of optical frequency. Using mean-field approximation we model the system by set of Maxwell-Bloch equations for the dressed states taking into account inhomogeneous broadening in QDs ensemble, incoherent losses and thermal noise existing in the system. Analysing the stationary solutions of the obtained equations we obtain the conditions for the amplification of the THz cavity mode. The numerical simulation of the obtained system of stochastic equations allows us to describe the generation of terahertz pulses and estimate the power of the lasing and its quantum efficiency.

4. Adiabatic preparation of a cold exciton condensate

The following chapter is devoted to the discussion of possibility of the controllable preparation of a cold indirect exciton condensate using dipolaritonic setup with an optical pumping. Dipolaritons are bosonic quasiparticles which arise from the coupling between cavity photon (C), direct exciton (DX), and indirect exciton (IX) modes, and appear in a double quantum well embedded in a semiconductor microcavity. Controlling the detuning between modes of the system, the limiting cases of exciton-polaritons and indirect excitons can be realized. Our protocol relies on the initial preparation of an exciton polariton condensate for the far blue-detuned IX mode, with its subsequent adiabatic transformation to an indirect exciton condensate by lowering IX energy via applied electric field. The following allows for generation of a spatially localized cold exciton gas, on the contrary to currently used methods, where IX cloud appears due to diffusion of carriers from spatially separated electron- and hole-rich areas.

4.1. Introduction

Experimental observation of Bose-Einstein condensation (BEC) [152] in a cold atomic gas system represents a major breakthrough of contemporary condensed matter physics [153, 154]. However, while being a perfect testbed for studies of macroscopically coherent phenomena, the requirement of ultralow temperature (< 1 μK) of an atomic gas restricts its possible applications. Fortunately, this requirement can be removed in solid state setups, where condensation of excitons in semiconductor structures was theoretically predicted [155, 156] for considerably higher temperatures (≈ 1 K). While unambiguous evidence of exciton condensation in a bulk and monolayer semiconductor structure is still lacking due to technological difficulties [157], several modifications of conventional excitonic system have shown promising results.

For instance, exciton polaritons, being a hybrid quasiparticles of coupled excitons in semiconductor quantum well and confined cavity photon [22, 21], represent a useful setup for studies of bosonic phenomena due to large decoherence times and simplicity of experimental characterization using optical techniques. The extremely small mass of these quasiparticles allowed to rise the typical critical temperature of condensation

to tens of Kelvins range [24, 25, 158, 159], and in certain cases up to room temperature [160, 161]. With experimental advances the macroscopically coherent polariton gas is now routinely observed in numerous system, working both with incoherent optical [24, 25] and electrical [162, 163] pump. The unique properties of polaritons enabled observation of solitons [164, 165, 166], quantized vortices [167, 168], polarization effects [169, 170, 171, 172], and are considered as a platform for optical computing [173]. At the same time, their short lifetime coming from cavity photon mode leakage does not allow for proper thermalization of particles, and essentially restricts the system to driven-dissipative non-equilibrium behavior [174].

Another bosonic system where long-range coherence was observed is represented by spatially indirect excitons—composite electron-hole objects formed in a double quantum well (DQW) [37, 175, 176]. An intense research in this area revealed various phenomena, including long-range luminescence ring pattern formation [38, 177, 178] and ring fragmentation [39, 179], polarization patterns and spin currents [180, 181, 182], electrical [183, 184] and acoustic [185] routing, quantum Hall effect [186] and others [187, 188, 189]. Given the reduced spatial overlap of electron and hole wavefunctions [190], which causes long lifetime of indirect exciton ($>$ 100 ns) [191], the efficient thermalization of particles can be achieved [39]. Simultaneously, the reduced photon-exciton interaction constant complicates the optical generation and characterization of indirect exciton gas [192]. In particular, one common scheme for IX cloud preparation includes optical generation of holes in one quantum well and electrical injection of electron in the adjacent well [176]. This largely impedes the spatial control of cold exciton gas, and for instance is believed to cause a fragmentation of an indirect exciton cloud [193]. A different way of exciton gas creation is the optical pump of DQW area in both coherent and decoherent regimes, where optical source is tuned to a direct exciton transition [194, 195, 196, 197, 198, 199].

Recently, the possibility to unite the subjects of exciton-polaritons and indirect excitons was attained in the system of dipolaritons [42, 41]. Being hybrid quasiparticles consisting of cavity photon (C), direct exciton (DX), and indirect exciton (IX), they share desirable properties of both polaritons and cold excitons, including enhanced interparticle interactions, enlarged lifetime, and improved optical control. The system of dipolaritons was proposed to serve as an efficient terahertz emitter [43, 44, 45] and tunable single-photon source [200, 201].

In the current chapter we present a scheme for optical generation of a cold indirect exciton condensate using a dipolariton setup. At the first step, it requires an initial preparation of an exciton polariton condensate using the incoherent optical pump [195], with indirect exciton mode lying high in energy for zero applied electric field F. By lowering IX energy with an increase of field F, the lower dipolariton state experiences adiabatic Landau-Zener transition [202, 203], converting to indirect excitonic state with high fidelity. The following allows for generation of a spatially localized cold exciton gas, on the contrary to the method of charge separation, where IX cloud appears due to diffusion of carriers from spatially separated electron- and hole-rich

areas. Moreover, it brings an extra degree of temporal control to the optical excitation methods, and allows to tailor the coherence properties of an indirect exciton gas.

4.2. The model

The considered structure consists of two asymmetric quantum wells separated by a thin barrier, allowing electron to tunnel between the wells [42]. This double quantum well system is placed in an optical microcavity, providing the existence of a cavity photon mode strongly coupled to a direct exciton mode, while an indirect exciton mode remains decoupled from the light mode [Fig. 4.1 (a)]. An indirect exciton instead is coupled to direct exciton due to coherent tunnel coupling between the QWs. The bias is applied to the heterostructure in the growth direction, which allows to tune the energy of an indirect exciton and thus the tunneling efficiency.

The Hamiltonian of dipolariton system can be written in the general form $\hat{H} = \hat{H}_{\text{coh}} + \hat{H}_{\text{dec}}$, where coherent and decoherent processes are separated. The coherent part of Hamiltonian reads:

$$\hat{H}_{\text{coh}} = \hbar\omega_C \hat{a}^\dagger \hat{a} + \hbar\omega_{DX} \hat{b}^\dagger \hat{b} + \hbar\omega_{IX}(t) \hat{c}^\dagger \hat{c} + \frac{\hbar\Omega}{2}(\hat{a}^\dagger \hat{b} + \hat{b}^\dagger \hat{a}) - \frac{\hbar J}{2}(\hat{b}^\dagger \hat{c} + \hat{c}^\dagger \hat{b}), \quad (4.1)$$

where $\hat{a}^\dagger$, $\hat{b}^\dagger$ and $\hat{c}^\dagger$ are creation operators of cavity photons, direct excitons, and indirect excitons, respectively. First three terms in Eq. (4.1) correspond to energies of photon ($\hbar\omega_C$), direct exciton ($\hbar\omega_{DX}$) and indirect exciton ($\hbar\omega_{IX}$) modes. The next two terms describe the direct exciton-cavity photon Rabi splitting $\hbar\Omega$ and the direct-indirect exciton tunneling splitting $\hbar J$. Here, we emphasize that an indirect exciton energy is time dependent, and depends linearly on the time-varied applied electric field $F(t)$, $\hbar\omega_{IX}(t) = \hbar\omega_{IX}^{(0)} - eLF(t)$. This expression hold for narrow QW heterostructure; $\hbar\omega_{IX}^{(0)}$ is an energy of indirect exciton at zero bias; L is a distance between centers of QWs; e denotes electron charge.

For the strong coupling case where intermode couplings Ω and J overcome decay (or broadening) of the modes, the eigenstates of Hamiltonian (4.1) correspond to lower (LP), middle (MP), and upper (UP) dipolariton states, being coherent superpositions of original C, DX, and IX states. The sketch of dipolariton dispersions is shown in Fig. 4.1 (b) for largely blue-detuned indirect exciton mode, and positive detuning of cavity photon with respect to direct exciton, $\omega_C - \omega_{DX} > 0$.

The initial feeding source of the dipolariton system is represented by laser tuned to high energies [Fig. 4.1 (b)]. It excites free electrons and holes, which relax to low energies, forming excitons with large wave vectors, commonly referred as reservoir states [204]. During this fast relaxation process the initial phase of the laser is fully lost, and incoherent reservoir of the direct excitons is created. Next, the excitons from

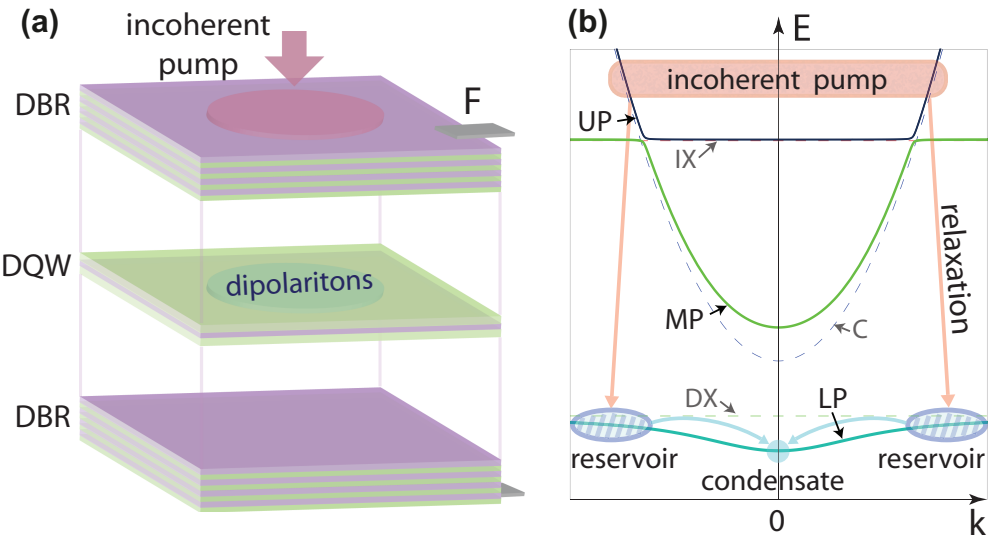

Figure 4.1: Sketch of the dipolaritonic system, representing double quantum well (DQW) structure embedded in a microcavity formed by distributed Bragg reflectors (DBRs). (b): Schematic representation of dispersion of lower (LP), middle (MP), and upper (UP) dipolaritons. Incoherent optical pump creates carriers at high energy, which relax to LP reservoir, and consequently scatter to a macroscopically coherent ground state.

reservoir can scatter due to exciton-phonon interactions towards ground state at zero wave vector of lower dipolariton mode, where they form a macroscopically occupied coherent state. The following excitation scheme is commonly used in conventional polaritonic setups [24], where nonequilibrium condensation of polaritons under incoherent pumping conditions was observed.

To describe incoherent processes related to phonon-assisted scattering of particles from reservoir to the ground state, we introduce the exciton-phonon interaction Hamiltonian $\hat{H}_{\mathrm{dec}} = \hat{H}^{+} + \hat{H}^{-}$, where

$$\hat{H}^{+} = D_{ph} \sum_{k} \hat{b}^{\dagger} \hat{r}_k \hat{d}_k^{\dagger}; \qquad \hat{H}^{-} = D_{ph} \sum_{k} \hat{b} \hat{r}_k^{\dagger} \hat{d}_k, \tag{4.2}$$

correspond to processes with emission ($\hat{d}_k^{\dagger}$) and absorption ($\hat{d}_k$) of phonons with wave vector k. $\hat{r}_k^{\dagger}$ and $\hat{r}_k$ are creation and annihilation operators for reservoir states. D_{ph} denotes exciton-phonon interaction constant.

In order to take into account the decoherence caused by a finite lifetime of the modes and interaction with reservoir, one can use the Lindblad master equation for the density

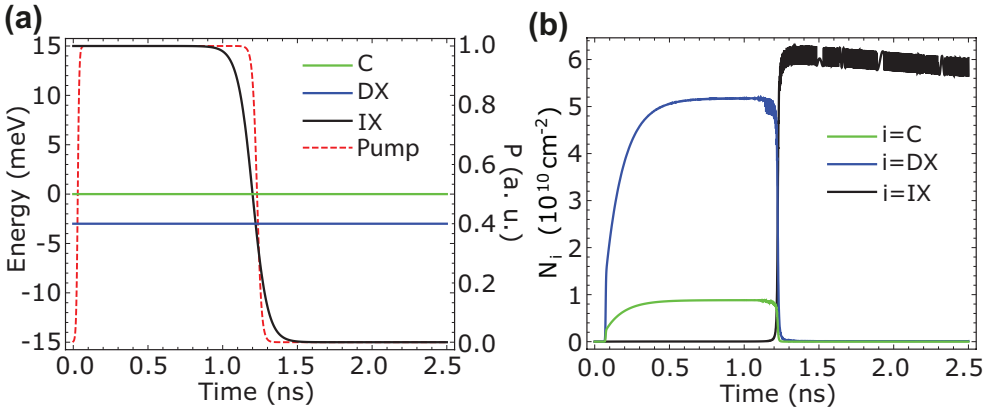

Figure 4.2: (a): Time dependence of energies of the modes. The bias applied to the system causes linear decrease of IX energy in $t = 1$ ns to $t = 1.5$ ns window, up to far red-detuned value. The dashed red line corresponds to time dependence of the pump intensity (in arbitrary units). (b): The evolution of occupations of the modes, being $N_C = |\langle\hat{a}\rangle|^2$, $N_{DX} = |\langle\hat{b}\rangle|^2$, and $N_{IX} = |\langle\hat{c}\rangle|^2$. At the first stage ($t < 1$ ns) the formation of polariton condensate takes place. Next, continuous change of an applied bias drives the system through an avoided crossing, leading to the transfer of polariton occupation to an indirect exciton mode.

matrix ρ,

$$\frac{\partial\rho}{\partial t} = \frac{i}{\hbar}[\rho, \hat{H}] + \hat{\mathcal{L}}^{(\mathrm{dis})}\rho + \hat{\mathcal{L}}^{(\mathrm{th})}\rho, \tag{4.3}$$

where $\hat{\mathcal{L}}^{(\mathrm{dis})}$ is Lindblad superoperator having the form $\hat{\mathcal{L}}^{(\mathrm{dis})}\rho = \sum_i \gamma_i(\hat{a}_i\rho\hat{a}_i^\dagger - \{\hat{a}_i^\dagger\hat{a}_i, \rho\}/2)$ with $\hat{a}_i = \hat{a}, \hat{b}, \hat{c}$ and $\gamma_j = 1/\tau_j$ $(j = C, DX, IX)$ being damping rates of the modes [43]. The term $\hat{\mathcal{L}}^{(\mathrm{th})}\rho$ corresponds to phonon-assisted processes accounted using Born-Markov approximation (see Appendix A).

Since we are interested in a large number of particles, we can apply the mean field approximation when time dynamics of the system can be defined by equations for mean fields given by $\partial\langle\hat{a}_i\rangle/\partial t = \mathrm{Tr}(\hat{a}_i\partial\rho/\partial t)$, where $\hat{a}_i = \hat{a}, \hat{b}, \hat{c}$.

Using the straightforward algebra we get equations of motions for the cavity photon, direct exciton, and indirect fields coupled to reservoir(see Appendix A for details of derivation):

$$\frac{\partial\langle\hat{a}\rangle}{\partial t} = -i\omega_C\langle\hat{a}\rangle - i\frac{\Omega}{2}\langle\hat{b}\rangle - \frac{\gamma_C}{2}\langle\hat{a}\rangle, \tag{4.4}$$

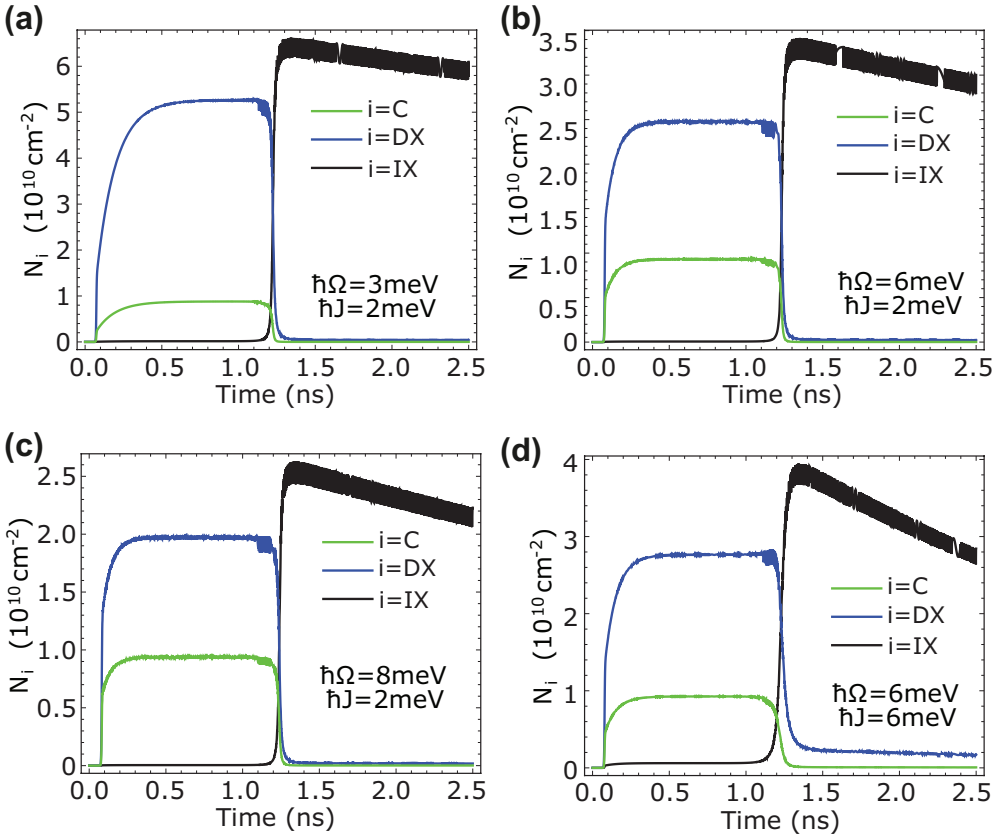

Figure 4.3: Transition dynamics shown for different coupling parameters Ω and J. (a, b, c): Tunneling coupling is fixed to $\hbar J = 2$ meV ($L_b = 8$ nm), while Rabi splitting is equal to $\hbar\Omega = 3$ meV (a), $\hbar\Omega = 6$ meV (b), and $\hbar\Omega = 8$ meV (c). (d): Occupation transfer in the system with equal couplings, $\hbar J = \hbar\Omega = 6$ meV.

$$\frac{\partial\langle\hat{b}\rangle}{\partial t} = -i\omega_{DX}\langle\hat{b}\rangle - \frac{\Omega}{2}\langle\hat{a}\rangle + i\frac{J}{2}\langle\hat{c}\rangle - \frac{\gamma_{DX}}{2}\langle\hat{b}\rangle + \frac{W}{2}\langle\hat{b}\rangle\left(N_R - N_{ph}\right), \tag{4.5}$$

$$\frac{\partial\langle\hat{c}\rangle}{\partial t} = -i\omega_{IX}(t)\langle\hat{c}\rangle + i\frac{J}{2}\langle\hat{b}\rangle - \frac{\gamma_{IX}}{2}\langle\hat{c}\rangle, \tag{4.6}$$

$$\frac{\partial N_R}{\partial t} = P(t) - \gamma_R N_R - W|\langle\hat{b}\rangle|^2\left(N_R - N_{ph}\right), \tag{4.7}$$

where $N_R = \sum_k n_k^R \equiv \sum_k \langle\hat{r}_k^\dagger \hat{r}_k\rangle$ denotes the full occupancy of the reservoir and $N_{ph} = \sum_k n_k^{ph}$ corresponds to the total number of the phonons defined by the temperature

of the sample. $W = 2\delta_R D_{ph}^2$ corresponds to the scattering rate of reservoir particles to macroscopically coherent state, where δ_R is the inverse broadening of exciton states divided by $\hbar^2$. The term $P(t)$ in Eq. (4.7) corresponds to the incoherent pump of reservoir states, which is typically given by the Lindblad type operator written in the form:

$$\hat{\mathcal{L}}^{(\mathrm{pump})}\rho = \sum_k P_k(t)\Big(\hat{r}_k\rho\hat{r}_k^\dagger + \hat{r}_k^\dagger\rho\hat{r}_k - \hat{r}_k^\dagger\hat{r}_k\rho - \rho\hat{r}_k\hat{r}_k^\dagger\Big), \tag{4.8}$$

where $|P_k(t)|^2$ denotes the intensity of incoherent pump of single reservoir state with in-plane wave vector k, and total pump is defined as $P(t) = \sum_k P_k(t)$. Writing the system of the kinetic equations we assumed large occupancy of the condensate state thus neglecting terms corresponding to spontaneous scattering. We checked numerically that these terms do not affect the obtained results.

4.3. Results and discussion

We simulate the dipolariton system based on $In_{0.1}Ga_{0.9}As/GaAs/In_{0.08}Ga_{0.92}As$ heterostructure [42]. The coupling parameters are chosen as $\hbar\Omega = 3$ meV and $\hbar J = 1$ meV. The latter corresponds to DQW with barrier width of $L_b = 10$ nm. Lifetimes of the modes are chosen as $\tau_C = 20$ ps, $\tau_{DX} = 1$ ns, $\tau_{IX} = 100$ ns. The damping rate of reservoir states $\gamma_R = 1/\tau_R$ is defined by lifetime $\tau_R = 0.1$ ns. Initially, at zero applied field energies of the modes system are tuned to $\hbar\omega_{DX} - \hbar\omega_C = -3$ meV, $\hbar\omega_{IX}^{(0)} - \hbar\omega_C = 15$ meV, and we set the reference point $\hbar\omega_C = 0$ without loss of generality [see Fig. 4.2 (a) for $t \to 0$]. The reservoir scattering rate $W = 1/\tau_{sc}$ is defined by characteristic exciton-phonon scattering time τ_{sc}, and chosen as 200 ps [124, 205]. The temperature of the sample was assumed to be $T = 0.7$ K, being typical for experiments with cold indirect excitons [175].

We start switching on incoherent pump $P(t)$ gradually [Fig. 4.2(a)], populating reservoir exciton states. Due to phonon-exciton interaction particles from reservoir thermalize and scatter to lowest energy state of lower dipolariton branch during several hundreds of picoseconds, where the steady-state is achieved approximately at 0.5 ns [Fig. 4.2 (b)]. By this moment the DX mode is highly populated, while IX mode remains empty due to large separation in energy and smallness of interaction with reservoir. The crucial idea now is to change the bias applied to the system. The IX mode energy then varies linearly up to large red-detuned value [$\hbar\omega_{IX}^{(\infty)} = -15$ meV], while direct exciton and cavity photon modes energies remain unchanged. The exact shape of IX energy dependence is plotted in Fig. 4.2 (a), and is described by formula $\hbar\omega_{IX}(t) = \left(\hbar\omega_{IX}^{(0)} - \hbar\omega_{IX}^{(\infty)}\right) / \left(1 + \exp^{[t-\tau]/\Delta\tau}\right) + \hbar\omega_{IX}^{(\infty)}$, where parameters are $\tau = 1200$ ps and $\Delta\tau = 50$ ps.

If one changes the bias slowly, the Landau-Zener type transition between bosonic

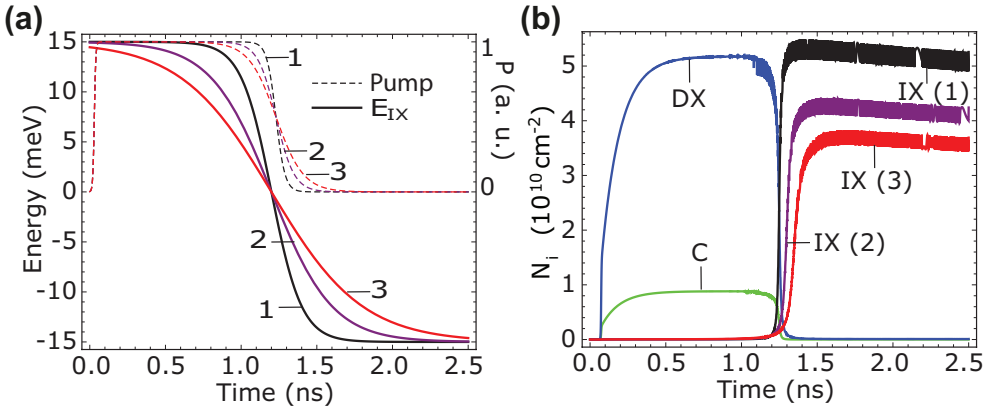

Figure 4.4: IX mode dynamics for different adiabaticity parameters. (a): Time dependence of IX mode energy (solid curves, left scale) and pump intensity (dashed curves, right scale). Three different regimes correspond to switching times $\Delta\tau_{1,2,3} = 100, 200, 300$ *ps. (b): Occupation number dynamics of the modes shown for different switching regimes. The dynamics of C and DX modes remains unchanged, while the final occupation of IX mode strongly depends on switching parameters.*

modes takes place. Namely, the system adiabatically follows the lower dipolariton branch, and at the final stage of complete swap gains 99.9% indirect exciton fraction. Alias, in the basis of bare modes the IX population largely increases due to transfer from cavity photon and direct exciton (polariton) modes, where their occupations drop to zero [Fig. 4.2 (b), after 1.3 ns]. This corresponds to conversion of macroscopically coherent polariton population to a gas of cold indirect excitons, which inherit coherence properties and demonstrate long lifetime (characteristic decay time > 10 ns for chosen parameters).

We note that successive preparation of cold exciton BEC requires simultaneous switching off the pump $P(t)$, leading to the rapid devastation of the reservoir mode. The following allows to keep high transfer fidelity, where overall particle occupation remains large during the transfer event, but prevents refilling of polaritonic states.

To characterize the system and find optimal parameters for cold exciton condensate preparation, we proceed considering different coupling parameters of dipolariton setup. In Fig. 4.3 the transition process is demonstrated for several values of Rabi frequency Ω and tunneling splitting J. First, we fix tunneling constant to $\hbar J = 2$ meV (as in Fig. 4.2) and vary the strength of light-matter interaction. We find that increase of Rabi frequency Ω causes the reduction of transition efficiency, which can be clearly observed in Figs. 4.3 (a), (b), and (c). First, this can be linked to increase of cavity photon admixture in the lower dipolariton mode, and consequent enlargement of decay. Second, the change of coupling Ω in general strongly influences Landau-Zener

transition in three-mode system.

In Fig. 4.3 (d) we show the population transfer for the case of equal couplings $\hbar J = \hbar\Omega = 6$ meV, corresponding to the sample discussed in the Ref. [46]. We observe that population transfer for these parameters is not perfect, and thus conclude that $J < \Omega$ condition shall be followed. Furthermore, we note that large values of tunneling constant J lead to stronger mixing of IX and DX modes, with consequent decrease of the lower dipolariton lifetime after switching.

Next, we study the influence of electric field switching process on the performance of population transfer. The main parameter here is a switching time τ, which also determines the switching rate $c = \Delta\tau^{-1}/4$ at which energy linearly decreases as $\sim -ct$ around transition point τ. It defines the adiabaticity of transition, and is of high importance for successive Landau-Zener transition. In particular, the optimal transfer requires slow variation of detuning, as compared to the energy distance between modes in the anticrossing point of dressed modes.

In Fig. 4.4 the time dynamics of the system is presented for different switching rates. We considered three regimes, altering both the rate of detuning switching and the front of pump switching, in order to keep density of the particles at the same level [Fig. 4.4 (a)]. We find that the voltage switching rate almost does not affect on the polariton population at steady-state condition, but strongly influences the efficiency of the transition, defining the IX mode occupation [Fig. 4.4 (b)]. For the switching time $\Delta\tau_1 = 100$ ps nearly perfect transfer was achieved. This confirms that the characteristic time corresponding to anticrossing energy distance is ~ 1 ps, and transition is adiabatic. However, decreasing the switching rate to $\Delta\tau_2 = 200$ ps and $\Delta\tau_3 = 300$ ps we revealed the reduction of transfer efficiency, signifying of an existence of an optimal rate $\Delta\tau$. The process of spoiling of transition is related to open-dissipative nature of the system under the study.

Finally, we acknowledge the presence of another bound which puts limitation on detuning switching rate. It comes from the experimental limitation of DC voltage sweep rate, which typically cannot outperform gigahertz repetition rates. While state-of-the-art devices with fast switching are currently engineered, [107] we probe the possibility to decrease the sweep rate up to 100 MHz range. In Fig. 4.5 we show that the transition can take place for switching time being in the tens of nanoseconds range [Fig. 4.5 (a)], easily achievable with current technologies. The transition efficiency in this case drops as opposed to less-than-nanosecond switching time. At the same time, a decent population of indirect exciton gas can be achieved for certain pumping conditions, which persists for tens of nanoseconds. The parameters of the system for this calculation were modified to $\hbar J = 0.6$ meV and $\hbar\Omega = 3$ meV.

Finally, let us discuss the immediate consequences of proposed scheme for cold exciton gas preparation. Being based on conversion of optically created polaritons to an indirect exciton gas, it ensures the preservation of the spatial shape of initial cloud, and

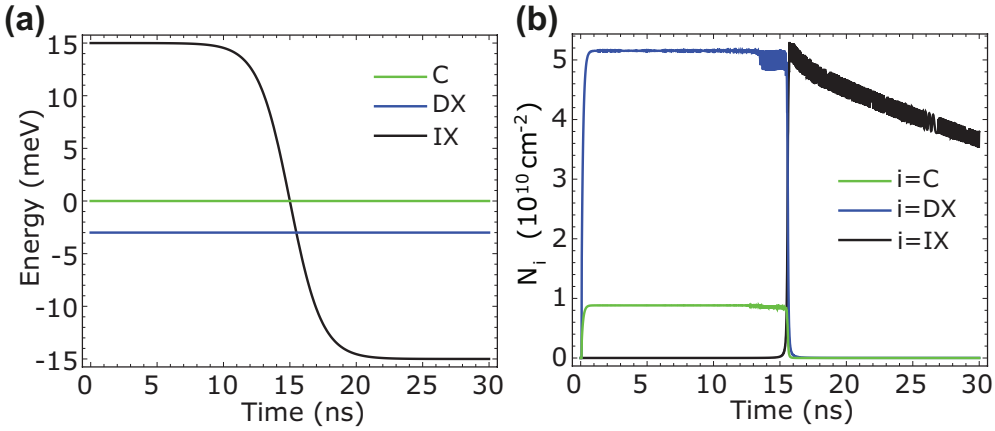

Figure 4.5: (a): Time dependence of energy of the modes for modified dipolariton system, where ultra-slow change of detuning is implemented. (b): Population transfer in dipolariton system for ultra-slow detuning change. Parameters of the calculation are: $\tau = 15$ ns, $\Delta\tau = 1.2$ ns.

does not involve separate injection of electron and hole carriers. This is in contrast to typical excitation scheme in the indirect exciton experiments, where optical generation of holes and electrical injection of electrons is used [175, 176]. The following allows to test the possible explanation of IX ring appearance based on the electrostatic reasoning [177, 178].

Moreover, we note that our proposal can be tested in first approximation even without the presence of an optical microresonator. In this case only coupled DX and IX modes are considered, and conversion of optically active direct excitons to a cloud of indirect excitons can be realized. It is interesting to note that a similar technique of simultaneous change of applied field and pump turn-off was applied for photon storage in the coupled quantum wells via DX-IX transitions [206]. However, on the contrary to the full dipolaritonic setup, no condensation effects for direct excitons are expected which can limit the efficiency of the proposed protocol.

4.4. Conclusions

In conclusion, we proposed the way for an on-demand optical preparation of a cold exciton condensate based on Landau-Zener bosonic transfer in a dipolariton system. The protocol is based on several steps. First stage corresponds to initial preparation of polariton condensate with high cavity photon and direct exciton fractions, while indirect exciton mode is located high in energy at zero external voltage. Next, applying

electric field the IX energy is lowered to far red-detuned value, where adiabatic following of the lower dipolariton mode converts particles to indirect excitons with inherited coherence properties. Finally, to reduce residual effects of cavity an optical incoherent pump of polaritonic reservoir states shall be switched off during the transfer event. We analyzed the population transfer for various sets of parameters and switching conditions, and demonstrated that adiabatic cold exciton preparation is experimentally feasible in currently existing setups.

5. Attractive Coulomb interaction of 2D Rydberg excitons

The following chapter is devoted to the theoretical study of Coulomb scattering processes of highly excited excitons in the direct bandgap semiconductor quantum wells. We find that contrary to the interaction of ground state excitons the electron and hole exchange interaction between excited excitons has an attractive character both for s- and p-type 2D excitons. Moreover, we show that similarly to the three-dimensional (3D) highly excited excitons, the direct interaction of 2D Rydberg excitons exhibits van der Waals type long-range interaction. The results predict the linear growth of the absolute value of exchange interaction strength with an exciton principal quantum number, and point the way towards enhancement of optical nonlinearity in 2D excitonic systems.

5.1. Introduction

The possibility to attain strong and tunable interparticle interactions in a many body system is indispensable for both fundamental studies of strongly correlations and practical exploitation of nonlinear effects. The vast variety of collective effects in cold atom systems [208] has profited from usage of Feshbach resonances [209]. They allow for tunability of s-wave scattering length for atomic collisions, changing the interaction character from a short-range repulsive to an attractive one. A major step forward in boosting the atomic interaction strength can be performed when atoms are excited to a large principal quantum number Rydberg state [2]. In this case the absolute value of interaction strength grows dramatically, and the interaction potential becomes of long-range nature, leading to the phenomenon of Rydberg blockade [210, 211, 212]. This facilitates numerous applications in the quantum optics domain [213], where large effective nonlinearity for photons enables efficient photon crystallization [214], creation of photonic molecules [215], ordered pattern formation [216] etc.

In the solid state physics, the studies of many body effects and nonlinear quantum optics became possible for the systems of interacting quasiparticles typically probed by light. Here, the prominent examples are indirect excitons [176, 37] and exciton polaritons [174]. The latter quasiparticles formed by the microcavity photons and

excitons in two dimensional (2D) semiconductor quantum well (QW) are especially valuable for observation of non-equilibrium condensation [24, 162], vortices [167], solitons [217, 166] and other effects characteristic to weakly nonlinear Bose gas. At the same time, the highly anticipated transition of polaritonics to quantum nonlinear regime is deferred by small and short range exciton-exciton interaction in QWs, which are dominated by *repulsive* Coulomb exchange, while direct interaction contribution is negligible [14, 15], except for the narrow energy range where the formation of bipolariton is possible. Therefore, it opens the challenge for system modification to attain strong interaction, or, alternatively, the search for optional strategies which require only weak nonlinearity [218, 200, 201].

Up to date proposals for the enhancement of nonlinearity include hybridization of polaritons with dipolar excitons (dipolaritons) [42, 41, 45] and exploitation of the biexcitonic Feshbach resonance [219, 220], though with limited capabilities. A drastic improvement was made in the system of highly excited 3D excitons, being excitonic counterpart of Rydberg atoms physics [3]. There authors reported an observation of the dipolar blockade appearing in bulk Cu_2O for giant excitons having principal quantum number up to $n = 25$ and μm diameter. The important consequence of using rather peculiar copper oxide semiconductor is selection rules which allow to optically pump excitons in the p-state, where excitons exhibit the long range interaction of dipolar and van der Waals type similarly to Rydberg atoms. At the same time, while results show the potential for strongly nonlinear optics, the requirement of 3D geometry and infeasibility of Cu_2O based microcavities hinder its application in the conventional form.

In this chapter we pose the question of possible achievement of the strong exciton-exciton interaction exploiting highly excited states of excitons in 2D semiconductor quantum wells. We show that for small transferred momenta the interaction of 2D excitons is dominated by short range exchange Coulomb interaction for both s and p exciton types, and find that for excitons with higher than ground principal quantum number ($n > 1$) the interaction constant changes the sign, leading to an *attractive* exciton-exciton potential. The absolute value of interaction strength scales linearly with n, and increases for small band gap semiconductors. At the same time, similarly to the 3D geometry, the direct interaction of 2D excitons possesses long range nature governed by van der Waals law and grows drastically with n. This suggests that 2D Rydberg exciton gas represents the nontrivial system, and can lead to emergence of hybrid repulsive-attractive bosonic mixtures.

5.2. The model

The calculation of interaction potential for 2D excitons in the ground state can be done within the Coulomb scattering formalism [14]. The theory can be extended to

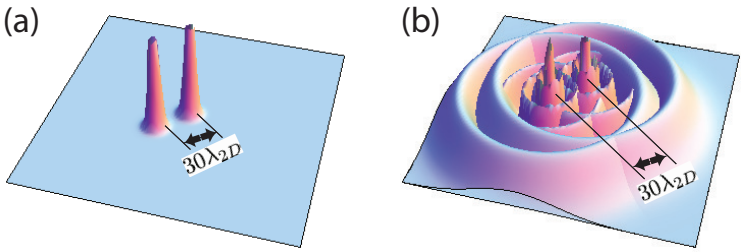

Figure 5.1: Real space distribution of exciton envelope wave functions with center-to-center separation distance of $30\lambda_{2D}$, shown for excitons in (a): 1s state, (b): 6s state.

describe the interaction of excitons in the excited states. The two dimensional exciton wave function with in-plane wave-vector $\mathbf{Q}$ in the general form reads

$$\Psi_{\mathbf{Q},n,m}(\mathbf{r}_e,\mathbf{r}_h) = \frac{1}{\sqrt{A}}\exp[i\mathbf{Q}(\beta_e\mathbf{r}_e+\beta_h\mathbf{r}_h)]\psi_{n,m}(|\mathbf{r}_e-\mathbf{r}_h|), \tag{5.1}$$

where $\mathbf{r}_e, \mathbf{r}_h$ are in-plane radius vectors of exciton and hole, respectively, and A denotes the normalization area. The coefficients β_e, β_h are defined as $\beta_{e(h)} = m_{e(h)}/(m_e+m_h)$, where $m_{e(h)}$ is the mass of an electron and a hole, respectively. The internal relative motion is described by [8]

$$\begin{aligned}\psi_{n,m}(|\mathbf{r}_e-\mathbf{r}_h|) = \quad & \frac{1}{\sqrt{2}\lambda_{2D}}\sqrt{\frac{(n-|m|-1)!}{(n-1/2)^3(n+|m|-1)!}}\left(\frac{|\mathbf{r}_e-\mathbf{r}_h|}{(n-1/2)\lambda_{2D}}\right)^{|m|} \\ & \exp\left[-\frac{|\mathbf{r}_e-\mathbf{r}_h|}{(2n-1)\lambda_{2D}}\right] L^{2|m|}_{n-|m|-1}\left[\frac{|\mathbf{r}_e-\mathbf{r}_h|}{(n-1/2)\lambda_{2D}}\right]\frac{1}{\sqrt{2\pi}}e^{im\varphi},\end{aligned} \tag{5.2}$$

where $n = 1, 2, 3, \ldots$ is the principal quantum number, $m = 0, \pm1, \ldots, \pm n \mp 1$ is the magnetic quantum number, and λ_{2D} is a variational parameter related to the two-dimensional radius of the ground state exciton. Here, $L^k_n[x]$ denotes associated Laguerre polynomial. In the following we consider the narrow quantum well limit and thus disregard exciton motion in the confinement direction.

Considering excitons with the parallel spin only, the process of Coulomb scattering in reciprocal space associated to the transfer of wave vector $\mathbf{q}$ can be described in the form:

$$(n,m,\mathbf{Q}) + (n',m,\mathbf{Q}') \to (n,m,\mathbf{Q}+\mathbf{q}) + (n',m,\mathbf{Q}'-\mathbf{q}). \tag{5.3}$$

The scattering matrix element consists of four terms:

$$H(n,n',m,\Delta\mathbf{Q},\mathbf{q},\beta_e) = \frac{e^2}{4\pi\varepsilon\varepsilon_0}\frac{\lambda_{2D}}{A}I_{\mathrm{tot}}(n,n',m,\Delta\mathbf{Q},\mathbf{q},\beta_e), \tag{5.4}$$

where

$$I_{\mathrm{tot}}(n,n',m,\Delta\mathbf{Q},\mathbf{q},\beta_e) = I_{\mathrm{dir}}(n,n',m,\mathbf{q},\beta_e) + I^{X}_{\mathrm{exch}}(n,n',m,\Delta\mathbf{Q},\mathbf{q},\beta_e) + I^{e}_{\mathrm{exch}}(n,n',m,\Delta\mathbf{Q},\mathbf{q},\beta_e) + I^{h}_{\mathrm{exch}}(n,n',m,\Delta\mathbf{Q},\mathbf{q},\beta_e). \tag{5.5}$$

Here, the first term denotes the direct interaction integral, the second corresponds to the exciton exchange interaction, and two last terms describe an electron and hole exchange integrals (see Appendix B1 for definitions and details).

Note that in the particular case where the wave vectors and principal quantum numbers of excitons coincide, $\Delta Q = |\mathbf{Q} - \mathbf{Q}'| = 0$, and $n = n'$, we have

$$I^{X}_{\mathrm{exch}}(n,n,m,0,\mathbf{q},\beta_e) = I_{\mathrm{dir}}(n,n,m,\mathbf{q},\beta_e), \tag{5.6}$$

$$I^{e}_{\mathrm{exch}}(n,n,m,0,\mathbf{q},\beta_e) = I^{h}_{\mathrm{exch}}(n,n,m,0,\mathbf{q},\beta_e), \tag{5.7}$$

and consequently,

$$I_{\mathrm{tot}}(n,m,\mathbf{q},\beta_e) = 2\big[I_{\mathrm{dir}}(n,m,\mathbf{q},\beta_e) + I^{e}_{\mathrm{exch}}(n,m,\mathbf{q},\beta_e)\big]. \tag{5.8}$$

In the following we are interested in the dependence of interaction on the scattered momentum $\mathbf{q}$, while considering equal exciton center-of-mass momenta, $\Delta Q = 0$.

To gain the qualitative understanding of interaction processes for highly excited excitons we shall look at the large n exciton wave function. In particular, Eq. (5.2) implies that the spatial distribution of exciton drastically increases with principal quantum number. Namely, the higher principal number of excitation is, the larger is a spread of wave function, providing increased overlap between excitons, and consequently leading to the enhanced exciton-exciton interaction. In Fig. 5.1(a) the real space distribution of two excitons in ground state is presented, where the interexciton distance is fixed to $30\lambda_{2\mathrm{D}}$. The peak-shaped distribution of wavefunctions determines the interaction behavior, which rapidly decreases as distance grows. Panel (b) shows the probability distribution for excitons in $6s$ state, with the same interexciton distance as before (i.e., same density of particles), revealing large overlap of wave functions.

5.3. Results

5.3.1. Interaction between s-type excitons

We examined numerically the Coulomb interaction integrals between excitons in s and p states as a function of the scattered momentum $\mathbf{q}$. The calculation was done by multidimensional Monte-Carlo integration with implemented importance sampling

algorithm, provided by the numerical integration CUBA library [221]. To be specific, we fixed the electron to exciton mass ratio to the value $\beta_e = 0.4$, which is close to GaAs quantum well effective mass ratio [222]. However, as it is shown below, the change of this parameter does not lead to significant quantitative and any qualitative changes of results. The possible choices for materials is discussed in the corresponding section.

We consider the interaction between two s-type excitons with the same ($\{n, n'\} = 11, 22, 33$) and different ($\{n, n'\} = 12, 23$) principal quantum numbers. The results of the calculation are plotted in Fig. 5.2. Panel (a) shows the direct interaction term as a function of dimensionless transferred momentum for various scattering processes. We find that direct interaction for ground state excitons and excited excitons has the same qualitative behavior, dropping to zero for small q and exhibiting maximum for intermediate momenta. The position of direct interaction peak shifts to smaller transferred wave vectors for increasing n, and its magnitude increases radically. We check that the following holds even for very large quantum numbers (up to $n = 10$; not shown). In Fig. 5.2 (b) we plot a 2D Fourier transform of $I_{\text{dir}}[q]$ interaction integral, which represents its real space dependence. The curves depict maximal but finite interaction strength for $n = n' = 1$ excitons at a small separation, which rapidly decreases with r. For excited states the $r \to 0$ peak flattens out, while total interaction range increases.

To understand the origin of interaction we examined the large separation distance behavior of the potential for excitons with quantum number in the range $n = 3..10$. The results are presented in Fig. 5.3. The analysis of interaction tail unveiled the rapid increase of interaction strength with the growth of principal quantum number, being another fingerprint of long range nature of interaction [2, 213, 3]. The corresponding numerical fit of real space interaction dependence revealed the van der Waals nature of potential ($I_{\text{dir}} \propto r^{-6}$), which was previously reported by Schindler and Zimmermann also for QW excitons in the ground state [223]. As it is expected, the distance where van der Waals behavior becomes relevant rapidly grows with the increase of the principal quantum number.

The characteristic feature of van der Waals interaction is the power dependence on the excitation number. To check this, we examined the dependence of the direct interaction strength on the excitation number for different fixed values of the separation distance. The sample of results is presented in Fig. 5.4, where the power dependence $\propto n^{\alpha}$ is clearly seen. We observe that due to small number of points the power α can lie in the 7 to 12 range, and expect it to be equal $\alpha = 11$ if large n are considered.

Next, we calculate the Coulomb exchange contribution to s-type exciton-exciton interaction. Fig. 5.5(a) illustrates the dependence of exchange integral I_{exch} as a function of $\mathbf{q}$ for different states. For the ground state scattering (inset, curve 11) the interaction is maximal in $q \to 0$ region, decreasing for large exchanged wave vectors, and has positive sign (repulsive potential). However, already for $n = n' = 2$ the sign of

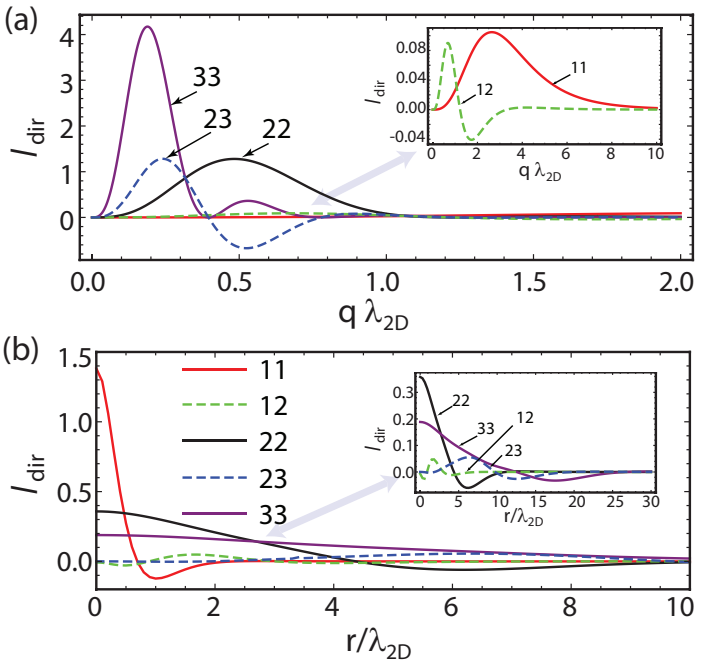

Figure 5.2: Interaction of s-excitons. (a) Dependence of direct exciton-exciton interaction on the scattered wave vector q (in terms of reverse two-dimensional exciton radius). Hereafter, the dimensionless value of the integral is presented. The solid lines correspond to interaction of excitons with the same $\{n, n\}$ principal quantum number, while dashed lines to the different $\{n, n'\}$ principal quantum numbers. (b) Real space dependence of direct interaction integral.

exciton interaction changes to *attractive* one, with maximal absolute value at small q. The same change applies to higher excited states interaction, and also to cross scattering between ground and excited state excitons. Moreover, we note that the maximal absolute value of potential grows with principal quantum number n, representing an enhancement of exchange contribution by increase of effective interaction area due to the spread of wave functions. Consequently, the real space dependence of exchange interaction has the form of an exponential decay, defined by the decrease of wave function overlap area.

Finally, we study the dependence of maximal absolute value of exchange integral as a function of principal quantum number $n = n'$, measured at $q \to 0$ point. The behavior is shown in Fig. 5.5(b) for both s and p excitons, corresponding to a linear increase of the magnitude for large principal quantum numbers, $n > 3$, where s and p interaction strengths coincide. At the same time, the clear difference in $\max\{|I^e_{\text{exch}}|\}$ for s and p states is visible at $n \leq 3$ range. This result can be explained by the fact that the radial

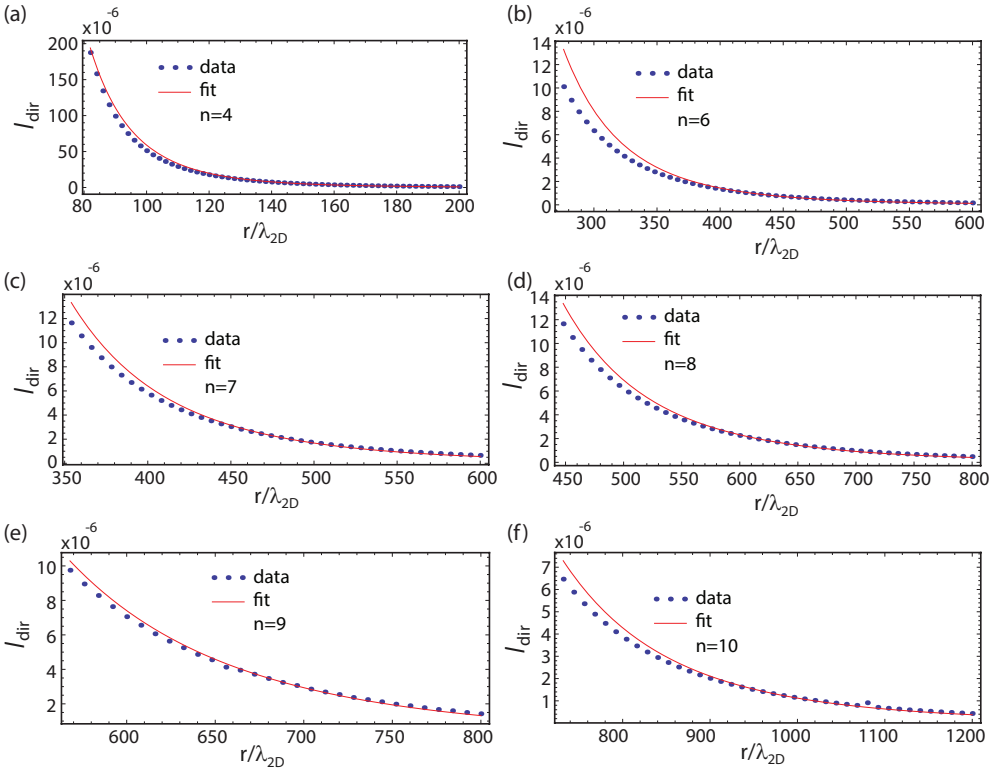

Figure 5.3: Dependence of long range direct exciton-exciton interaction on the separation distance r. The panels (a)-(f) correspond to the interaction of states with principal quantum number $n = 4, 6, 7, 8, 9, 10$, respectively. For each value of n the numerical fit shows $\propto r^{-6}$ dependence, characteristic to van der Waals interaction.

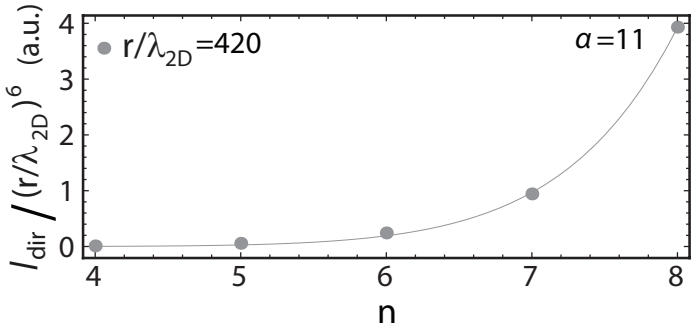

Figure 5.4: Dependence of direct Coulomb interaction on the excitation number n for fixed separation distance. The numerical fit shows $\propto n^{\alpha}$ dependence.

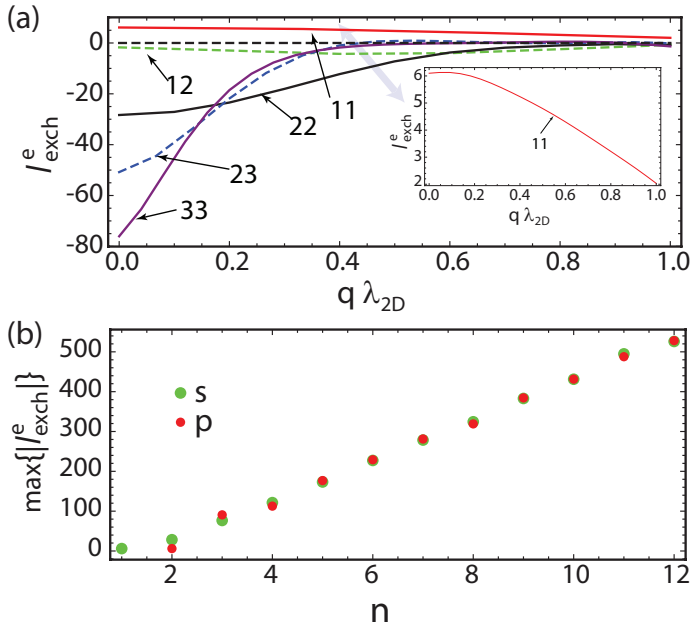

Figure 5.5: (a) Dependence of s-type exciton-exciton interaction electron exchange term on the scattered wave vector q. (b) The maximal absolute value of the exchange interaction plotted as a function of principal quantum number n for s and p states. The linear in n growth of the interaction strength is observed.

parts of wave functions of excited states have the same shape at larger radii, although being different at small r, relevant for small n excitons. As it was mentioned above, the exchange interaction between excited 2D excitonic states is strongly attractive and does not drastically depend on the electron-to-exciton mass ratio β_e. To prove this, we calculate the momentum dependence of exchange interaction of $2s$ excitons for various values of β_e. The results are presented in Fig. 5.7. As it follows from the figure, for relatively small values of transferred momenta the scattering amplitude has weak mass dependence.

The total interaction potential in the case of equal wave vectors and principal quantum numbers, represented by Eq. (5.8), is shown in Fig. 5.6 as a function of the transferred momentum $\mathbf{q}$. It reveals that for very small values of q the total interaction for excited states is fully determined by the exchange interaction, being attractive. However, for larger transferred momenta it is replaced by weak repulsion, showing the dominant contribution of the direct interaction term in large q region. Noteworthy, for higher excitation number the region with domination of repulsion is shifted to smaller transferred momenta values. This alternating sign behavior is intriguing as it can potentially lead to the formation of supersolid state [224].

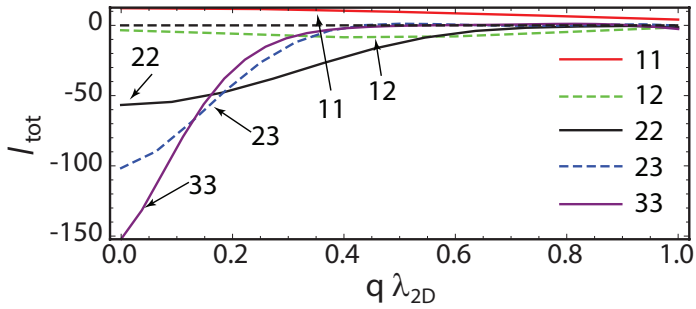

Figure 5.6: Overall interaction of s-type excitons as a function of the scattered wave vector q. For small values of q the interaction is highly attractive due to the dominant exchange interaction, while for large values the direct term prevails, leading to the repulsive character of total interaction.

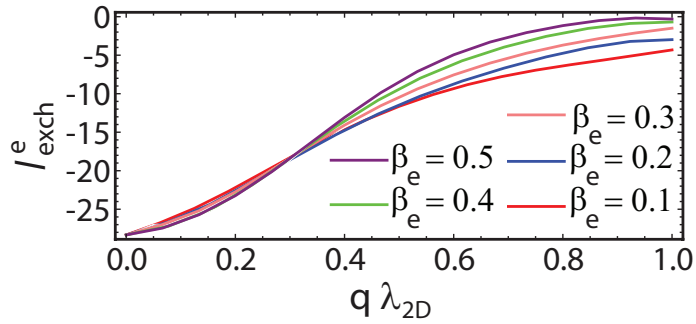

Figure 5.7: Dependence of exchange Coulomb interaction on the transferred momentum q for various fixed mass ratio $\beta_e = \{0.1, 0.2, 0.3, 0.4, 0.5\}$. We consider interaction of two 2s excitons.

5.3.2. Interaction between p-type excitons

We proceed with the discussion of direct and exchange Coulomb integrals for two *p*-type excitons. While non-zero angular momentum states are not straightforwardly accessed by optical means in direct-gap semiconductors (GaAs, GaN, ZnO etc.), one can envisage the situation when these become relevant in the low dimensional structures. As an example they can be created by two photon pumping [225]. The results of numerical integrations are presented in Fig. 5.8. Panels (a) and (b) show the direct interaction integral as a function of transferred momentum and interexciton distance for various values of the principal quantum numbers. We note that qualitatively it has the same behavior as *s*-type excitons, with minor variations of positions and heights of absolute maxima. Noteworthy, while for *p*-shells of 3D excitons the long range interaction has dipole-dipole contribution, it is absent for 2D excitons with non-zero

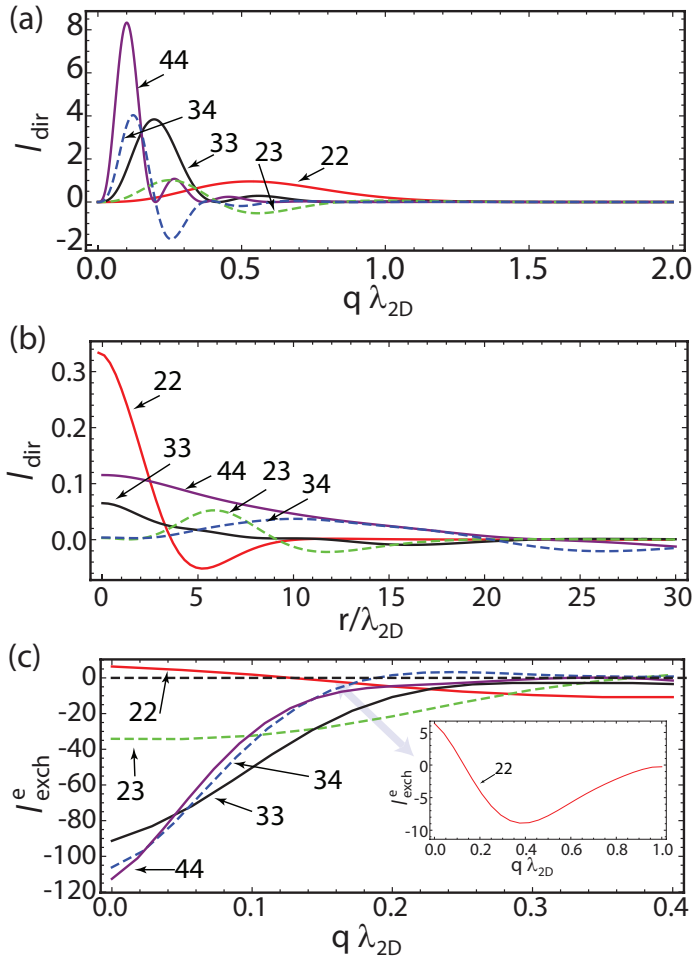

Figure 5.8: Interaction of p-excitons. (a) Dependence of direct exciton-exciton interaction on the scattered wave vector q (in terms of reverse two-dimensional Bohr radius). Here, the dimensionless value of integration is presented. (b) Real space dependence of direct interaction integral. (c) Dependence of electron exchange term on the scattered wave vector q.

angular momentum.

Finally, panel 5.8 (c) illustrates the exchange term dependence on the transferred wave vector $\mathbf{q}$. We first note that the ground state of p excitons corresponds to the value of principal quantum number $n = 2$. Hence, the exchange interaction of $2p$ excitons is repulsive and similar to the interaction of $1s$ excitons. As for excited states, it has a shape similar to one of s-type excitons with higher value of absolute maxima.

5.4. Discussion and outlook

Previously we have shown that interactions between excited excitonic states in 2D structures have different contributions, which are largely dependent on the main quantum number n and interexciton separation. While very large n excitons physics is expected to be driven by long range interactions, the relevant properties of ground state excitons are defined by short range exchange potential. Thus, we expect the cross-over between to regimes to happen in the range of intermediate $n > 1$, where strong short-range attractive interaction dominates. To increase the overall interaction even further, we consider possible semiconductor materials where Rydberg excitons can be observed. The parameters of 2D Bohr radius, binding energy Ry_{3D}, Coulomb interaction prefactor of Eq. (5.4) $\alpha_C \equiv e^2\lambda_{2\mathrm{D}}/4\pi\varepsilon\varepsilon_0$, and band gap E_g are collected in Table I for various semiconductors (data is taken from Refs. [226, 227, 228]). One can see that with increasing band gap the exciton Bohr radius decreases, consequently diminishing the interaction constant. At the same time we note that successful generation of highly excited excitonic states requires large binding energy of excitons, which allows to address separately excitonic states with large n. Therefore, an interplay between interaction strength and exciton energy separation determines the choice of materials relevant for described physics. Depending on the goal, they

	$\lambda_{2\mathrm{D}}$ (A)	Ry_{3D} (meV)	$\boldsymbol{\alpha_C}$ **($\boldsymbol{\mu}$eV$\boldsymbol{\mu m^2}$)**	E_g (eV)
InAs	184.45	1.29	**1.75**	0.354
GaSb	111.95	2.05	**1.03**	0.726
InN	36.3	6.47	**0.34**	0.78
InP	46.95	6.13	**0.54**	1.344
GaAs	93.6	4.57	**1.04**	1.424
CdTe	30.1	11.70	**0.42**	1.5
GaN	21.75	17.04	**0.32**	3.2
ZnO	10.55	40.22	**0.178**	3.37

Table 5.1: The estimation of Bohr radius of two-dimensional exciton, Coulomb interaction constant $\alpha_C \equiv e^2\lambda_{2\mathrm{D}}/4\pi\varepsilon\varepsilon_0$, and binding energy (3D) for direct band gap semiconductors. The list is sorted by increasing order of a semiconductor band gap.

may span from mid-bandgap semiconductors (e.g. GaAs) to large-bandgap materials (e. g. GaN). Additionally, we underline the possible importance of materials with the non-Rydberg excitonic spectrum, represented by transition metal dichalcogenides [229, 230, 231, 232], where the described bound can be violated.

Finally, we foresee that optical pumping of s excitonic states does not pose optical selection rules for excitons with different n, which allows the creation of $n = 1, 2, 3, ...$ exciton mixture. Given its mutually attractive and repulsive interaction, we expect an intriguing collective effects to appear in the system.

5.5. Conclusion

In summary, we studied the Coulomb interaction of excited states of excitons in direct gap semiconductors. We show that the total interaction of higher states has an attractive character due to the dominant contribution of exchange terms. The linear increase of interaction maxima with increase of the principal quantum number of excitonic state was observed. Contrary to 3D excitons, no dipolar interaction appears for large quantum number 2D excitons, and direct interaction has van der Waals behavior. The results point out an importance of Rydberg excitonic states, and may open the way towards studies of repulsive-attractive bosonic mixtures.

6. Exciton-exciton interaction in transition-metal dichalcogenide monolayers

We study theoretically the Coulomb interaction between excitons in transition metal dichalcogenide (TMD) monolayers. We calculate direct and exchange interaction for both ground and excited states of excitons. The Coulomb interaction screening, specific to monolayer structures, leads to the unique behavior of the exciton-exciton scattering for excited states, characterized by non-monotonic dependence of the interaction as a function of the transferred momentum. We find that the nontrivial screening enables the description of TMD exciton interaction strength by an approximate formula, consisting of exciton binding parameters. Furthermore, we consider exciton-electron interaction, which for excited states is governed by the dominant attractive contribution of the exchange component, which increases with the excitation number. The results provide a quantitative description of the exciton scattering in transition metal dichalcogenides, being a background for the future nonlinear optical devices based on TMD monolayers.

6.1. Introduction

The physics of excitons and associated optical phenomena were greatly influenced by recent studies of transition metal dichalcogenide (TMD) materials [233]. They typically exist in the form of a monolayer, and possess largely different properties compared to other semiconductors. Given their bandgap characterized by an optical interband transition and being atomically thin, they enjoy favourable optical properties as compared to semimetallic graphene structures, yet exhibiting flatland physics.

Extensive studies of excitonic properties of TMD monolayers started immediately after their discovery [234]. In striking contrast to bulk and quasi-2D structures, the different screening in 2D monolayer governs the deviation of the interparticle Coulomb interaction from the standard form, and ultimately leads to unusual properties of excitons in TMD structures [235, 236]. The exciton binding energies and absorption spectra in various TMD monolayers were measured experimentally [237, 238, 239, 240, 241, 242]

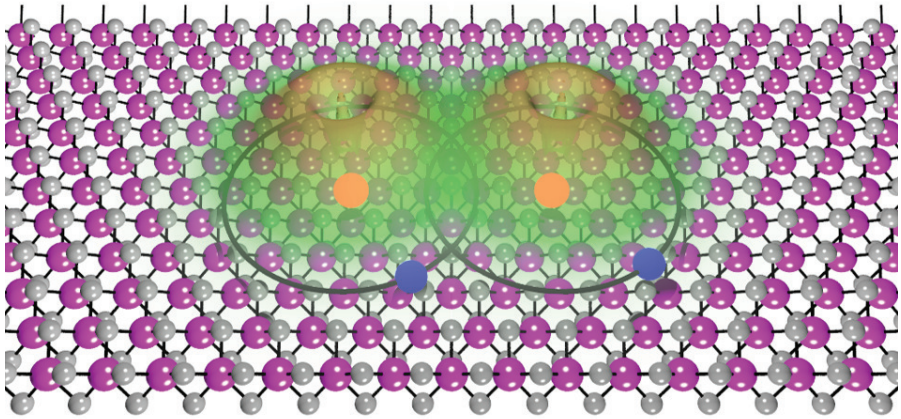

Figure 6.1: Sketch of the system. A transition metal dichalcogenide monolayer hosts excitonic quasiparticles formed by electrons (blue circles) and holes (red circles). The scattering between two excitons corresponds to the Coulomb interaction between carriers, consisting of the direct and exchange contributions. The latter is dependent on the exciton wavefunction overlap, shown in green.

and calculated from the first principles [232, 243, 244, 245, 246, 247, 248, 249]. They have shown a huge increase of the exciton binding energy (up to 1 eV) [250], as compared to conventional semiconductors, and the non-hydrogenic behavior of the excitonic series [251]. Further investigations cover measurements of exciton lifetimes and linewidths in monolayers [252, 253, 254], as well as electric field control of the excitonic properties [255, 256]. Moreover, the rich many-body physics in TMD materials was confirmed by observation of more complex particles, such as trions and biexcitons [257, 258, 259, 260] as well as interlayer excitons in bilayer structures [262, 261, 263]. Additionally, the hybrid exciton-electron systems in TMDs were considered [264].

The excellent optical properties of TMD monolayers has put them as a prominent platform for optoelectronical applications. For instance, the large binding energy of excitons allowed to study excitonic physics at elevated temperatures, and measure excitons with high principal quantum numbers [251]. The large oscillator strength allows to couple excitons strongly to an optical microcavity mode, and study strong light-matter coupling at room temperature [265, 266, 267]. The particular spin-orbit interaction for the bands leads to non-trivial valley dynamics and spin properties, also suggested to be potentially interesting for the quantum information processing [268]. Finally, χ_2 nonlinear response of TMD monolayers was predicted, making it suitable for the observation of the nonlinear quantum optical effects [269]. There are several experimental investigations of TMD monolayer properties in the strong exci-

tation regime, manifesting itself in various intriguing phenomena, including spectral peak broadening [270], exciton-exciton annihilation [271], and giant bandgap renormalization (up to 500 meV) in the vicinity of Mott transition [272, 273]. However, to the best of our knowledge, theoretical investigations of the interexciton interactions in TMD monolayers are lacking so far.

Motivated by the aforementioned advances, we consider the nonlinear properties of excitons in a TMD monolayer. The system is well-suitable for the observation of highly excited states of excitons, and similarly to bulk semiconductors [3], can allow for studying nonlinear interaction between Rydberg excitons. In the paper, we calculate the exciton-exciton interaction in TMD structures, considering both ground and excited states of excitons. We find that the interaction of excited states exhibits non-monotonic dependence on the exchange momentum and is attractive. We provide the analytical formula to quantitatively estimate the maximal exciton-exciton interaction strength, which differs from the III-V group semiconductor case. Finally, we calculate the exciton-electron matrix elements and show reciprocal space dependence of direct and exchange interactions.

6.2. Excitonic spectrum in TMD monolayer

To study the interparticle interactions in the TMD monolayers, one should take into account structural peculiarities of such materials. Namely, the atomic thickness of the layer and a discontinuity of the dielectric screening on the monolayer interface modifies the Coulomb interaction to the following form [235]:

$$V(r) = \frac{e_1 e_2}{4\pi\varepsilon_0}\frac{\pi}{2r_0}\left[H_0\left(\frac{r}{r_0}\right) - Y_0\left(\frac{r}{r_0}\right)\right], \tag{6.1}$$

where e_1, e_2 denote the charge of particles, r is the interparticle distance, and r_0 is a quantity describing the polarizability of the monolayer. H_0 and Y_0 are zeros order Struve and Bessel functions of the first kind, respectively. The modification of Coulomb interaction results into qualitative change of the excitonic spectrum [232, 251], which in this case cannot be considered as common 2D hydrogenic spectrum of the form $E_n = \mu e^4/[2(4\pi\varepsilon_0\varepsilon)^2\hbar^2(n-1/2)^2]$, where n is a principal quantum number of the exciton. Here, μ denotes a reduced mass of an exciton, ε corresponds to the static dielectric screening constant, and ε_0 is the vacuum permittivity. The excitonic states in this case correspond to the solutions of the Hamiltonian

$$\hat{H}_{exc} = -\frac{\hbar^2}{2\mu}\Delta + V(r), \tag{6.2}$$

with $V(r)$ is taken in the form of Eq. (6.1). In the first approximation one can find all solutions of the stationary Schrodinger equation for Hamiltonian (6.2) by means of

n	λ_n (nm)	E_n (meV)
1	1.7	320
2	0.65	160
3	0.45	90
4	0.35	60
5	0.3	50

Table 6.1: Spatial characteristics (λ_n) and energies of excitons (E_n) of different states n calculated for the WS_2 monolayer.

variational method, where as trial functions conventional 2D excitonic functions are used [8]:

$$\psi_{n,m}(r) = \frac{1}{\sqrt{2}\lambda_n}\sqrt{\frac{(n-|m|-1)!}{(n+|m|-1)!(n-1/2)^3}} \left(\frac{r}{(n-1/2)\lambda_n}\right)^m \exp\left[-\frac{r}{(2n-1)\lambda_n}\right] L^{2|m|}_{n-|m|-1}\left[\frac{r}{(n-1/2)\lambda_n}\right]\frac{1}{\sqrt{2\pi}}e^{im\varphi}. \tag{6.3}$$

Here $L^m_n[x]$ denotes associated Laguerre polynomial, λ_n is a variational parameter, and m is an angular momentum quantum number. Contrary to the conventional quantum well exciton, where all the states have the same radial characteristic — a two-dimensional Bohr radius, in the case of a monolayer the spatial parameter λ_n changes from state to state.

To be specific, we consider WS_2 monolayer, noting however that all the results carry general character and are applicable for the whole family of TMD monolayers. Accurate calculation of exciton series confirmed by experimental data was done in Ref. [251], where the value of polarizibility parameter r_0 was found to be equal to 7.5 nm. Here, we reproduce these results by the binding energy minimization using λ_n as a variational parameter. The corresponding values of the exciton energies and spatial characteristics λ_n are presented in the Table 1. Note that while the energies of the lower states are essentially non-hydrogenic, for the states starting from $n = 3$ the conventional n^{-2} dependence can be observed. Correspondingly, some saturation of the λ_n values can be seen for higher states.

6.3. Exciton-exciton interaction

Analyzing the asymptotic behavior of the potential given by Eq. (6.1) one can find its accurate approximated expression [236]

$$V(r) = -\frac{e_1 e_2}{4\pi\varepsilon_0}\frac{1}{r_0}\left[\ln\left(\frac{r}{r+r_0}\right) - (\gamma - \ln 2)e^{-\frac{r}{r_0}}\right], \tag{6.4}$$

which is used in further calculations. Here, γ denotes the Euler gamma constant. To calculate interactions between TMD monolayer excitons in the ground and excited states, we employ the method for calculation of the interaction between Rydberg state excitons. Recently it was applied to III-V semiconductor quantum well structures [A2], and is a generalization of the Coulomb scattering formalism for the ground state excitons in quantum wells [15, 14]. The motional state of an exciton with a wave vector $\mathbf{Q}$ can be written in the form

$$\Psi_{\mathbf{Q},n,m}(\mathbf{r}_e, \mathbf{r}_h) = \frac{1}{\sqrt{A}}\exp[i\mathbf{Q}(\beta_e \mathbf{r}_e + \beta_h \mathbf{r}_h)]\psi_{n,m}(|\mathbf{r}_e - \mathbf{r}_h|), \tag{6.5}$$

where $\mathbf{r}_e, \mathbf{r}_h$ are the radius vectors of an electron and a hole, respectively, and A denotes the normalization area. The coefficients β_e, β_h are defined as $\beta_{e(h)} = m_{e(h)}/(m_e + m_h)$, where $m_{e(h)}$ is the mass of an electron (hole). The internal motion is described by Eq. (6.3).

We consider the interaction of excitons in the same states with parallel spin projections. In this case the process of Coulomb scattering in reciprocal space with the transfer of wave vector $\mathbf{q}$ can be presented in the form

$$(n, m, \mathbf{Q}) + (n, m, \mathbf{Q}') \to (n, m, \mathbf{Q} + \mathbf{q}) + (n, m, \mathbf{Q}' - \mathbf{q}), \tag{6.6}$$

which is also shown graphically by scattering diagrams in Fig. 6.2. Using the wave function symmetrization procedure the total interaction may be presented as a linear combination of the interaction channels, including direct interaction, and electron, hole, exciton exchange terms, as schematically depicted in Fig. 6.2 (a)-(d). It was shown previously [14, 15],[A2] that in the wide region of exchange wave vectors $q \leq 1/\lambda_1$ the interaction of excitons is determined by the exchange terms, while the direct interaction in negligibly small. The latter becomes dominant for large values of $\mathbf{q}$, governing the long range behavior of the interaction. Thus, assuming the initial wave vectors being equal and setting $\mathbf{Q} = \mathbf{Q}' = 0$, for the total interaction we have (see Appendix B2 for the details and definitions):

$$V_{tot}(n, m, \mathbf{q}) = \frac{e^2}{4\pi\varepsilon_0}\frac{\lambda_1}{A} I_{\mathrm{tot}}(n, m, q\lambda_1), \tag{6.7}$$

$$I_{\mathrm{tot}}(n, m, q\lambda_1) = I_{\mathrm{dir}}(n, m, q\lambda_1) + I^X_{\mathrm{exch}}(n, m, q\lambda_1) + I^e_{\mathrm{exch}}(n, m, q\lambda_1) + I^h_{\mathrm{exch}}(n, m, q\lambda_1) \approx 2I^e_{\mathrm{exch}}(n, m, q\lambda_1), \tag{6.8}$$

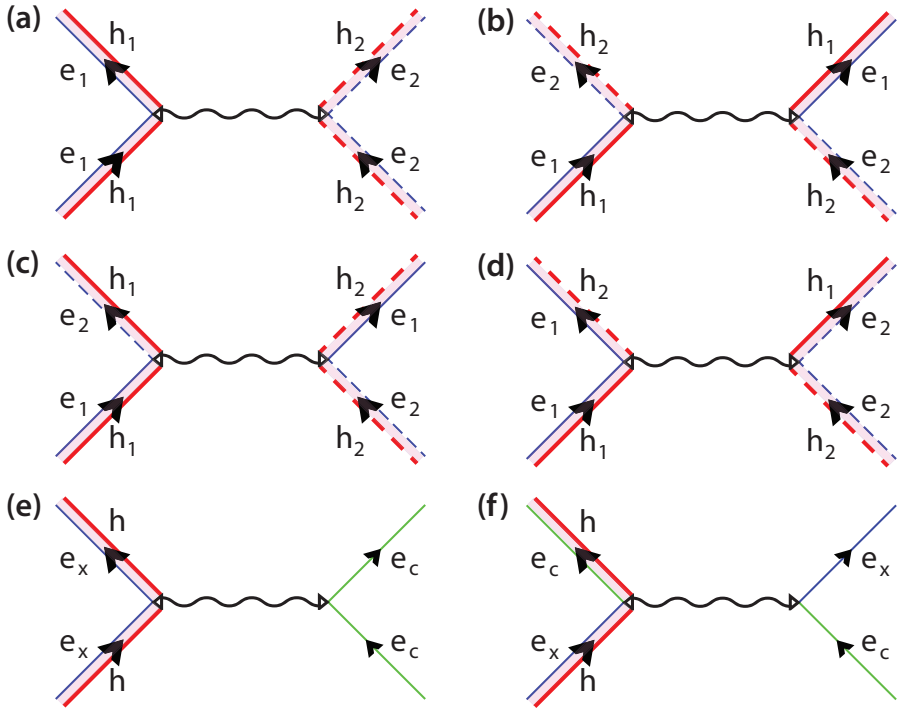

Figure 6.2: The schematic representation of the exciton-exciton scattering ***(a)-(d)****. Panels correspond to: (a) direct, (b) exciton exchange, (c) electron exchange, and (d) hole exchange interactions. Blue and red solid lines denote an electron (e_1) and a hole (h_1) of the first exciton exciton, and the dashed lines correspond to the second exciton marked with e_2 and h_2. The exciton-electron scattering diagrams are shown in panels* ***(e)-(f)****, describing the direct (e) and exchange (f) interaction. Green solid line (e_c) denotes a free electron.*

where indices e, h, X stand for the electron, hole, and exciton exchange integrals, respectively. In principle, the interaction processes between excitons with different spin projections can be accounted for. However, they involve spin-flip processes, and typically contain only direct interaction channel [40].

We calculate the direct and total interaction as a function of the scattered momentum exploiting the multidimensional Monte-Carlo integration [221]. The results of the calculation are shown in Fig. 6.3. The direct interaction as a function of the exchanged momentum is repulsive, and its peak-shaped dependence becomes narrower with the increase of the principal quantum number of scattered excitons. The total interaction is fully governed by the exchange term, which is non-zero at $q\lambda_1 \to 0$. It is repulsive for the ground state and attractive for the excited states. This behavior is qualitatively similar to quantum well exciton interaction [A2]. However, the screened nature

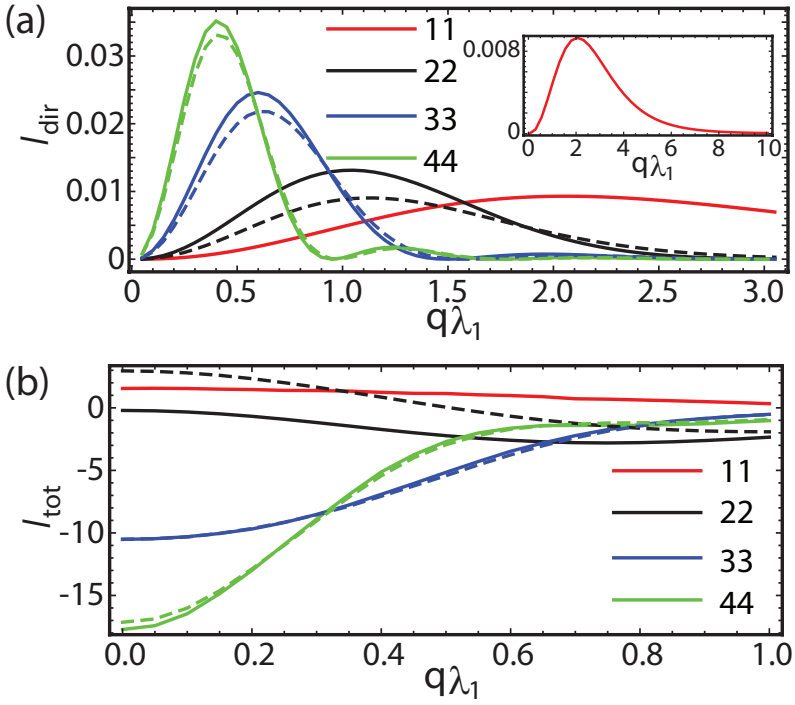

Figure 6.3: Dimensionless integrals corresponding the direct interaction matrix element (a), and total interaction energy (b) of excitons in TMD monolayer, plotted as a function of the transferred wave vector. Solid lines correspond to s states ($m = 0$), dashed lines denote p states ($m = 1$). The interaction has similar form for both type excitons, being attractive for the excited states. The difference appears for $n = 2$ state, where for s state there is an attraction with the absolute maxima at intermediate momenta, and for p state there are attraction and repulsion regions.

of Coulomb interaction imposes peculiarities in the TMD exciton-exciton interaction behavior. Namely, the crucial difference of the monolayer exciton interaction appears in the dependence of $2s$ state interactions, which demonstrate potential minima for the nonzero exchange momenta q. It should be noted, that the interaction of $2p$ excitons demonstrates similar properties, being repulsive for zero exchange momenta and having attraction peak at intermediate momenta. This non-monotonic behavior is expected to lead to different condensation processes for TMD polaritons [224].

Next, we search for the compact analytical formula to describe the exciton-exciton interaction in TMD monolayers, considering both ground and excite states scattering. Previously in was shown that the exchange interaction of GaAs quantum well ground state excitons can be described by the formula $V_{exch}^{QW} = 6E_b a_B^2/A$, where a_B and E_b denote the Bohr radius and binding energy of quantum well exciton, respectively [15].

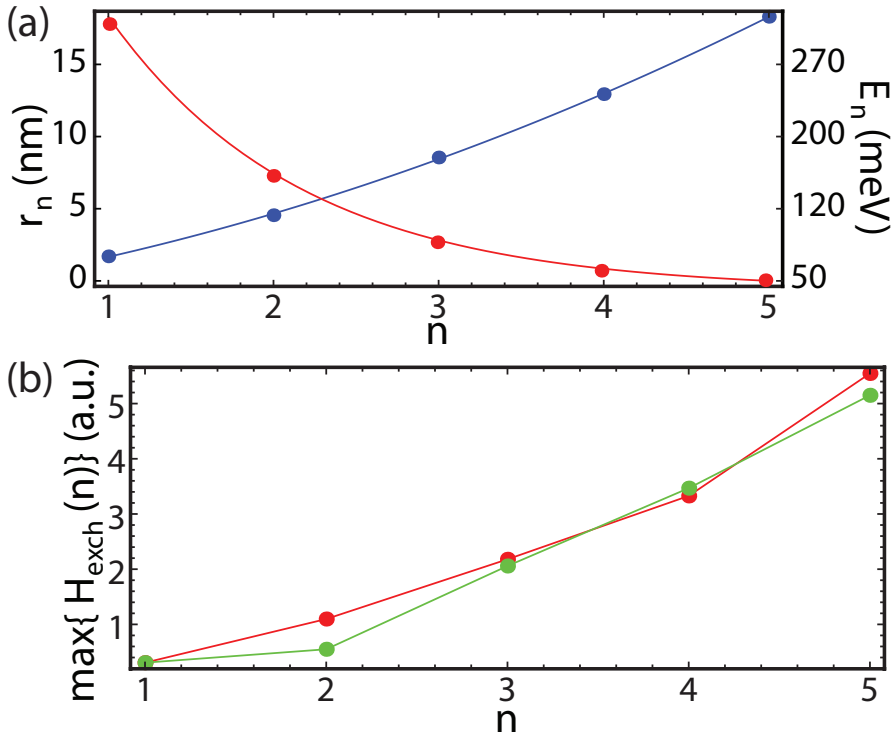

Figure 6.4: (a) Exciton radius (blue curve) and energy (red curve) dependence on the principal quantum number. (b) Exchange interaction energy as a function of the principal quantum number of a TMD exciton. The green curve corresponds to the exact numerical calculation, and the red line shows the qualitative estimate using Eq. (6.9).

Here, the numerical prefactor comes from the calculation of exchange integrals. Following the analogy, we found a similar dependence for exciton series in TMD monolayer. In particular, Fig. 6.4(a) presents the dependence of the radius and energy of exciton states on their principal quantum number. While the radius increases quadratically (as in the case of the conventional Rydberg series), the energy dependence for the first few states drops superpolynomially with n. The latter allows us to approximate the exchange interaction dependence by the formula

$$V_{exch}(n) = \alpha E_n r_n^2 / A, \tag{6.9}$$

where r_n and E_n denote the radius and energy of n-th exciton state, respectively, and α is a fitting constant. The green line in Fig. 6.4(b) denotes the dependence of the exchange interaction strength on the principal quantum number, unveiling close-to-linear dependence starting from the $n = 2$ state. The red curve shows the estimate by Eq. (6.9), where we chose the parameter $\alpha = 2.07$, which gives the exact fitting

for the ground state. It worth mentioning that despite the smaller pre-factor, for the case of quantum well with the similar material parameters the interaction would be weaker. The reason beyond this is the interaction screening, leading to the exciton effective radius value larger than for conventional Coulomb potential. Consequently, the interaction strength can be enhanced even further in the case of monolayer growth on the substrate with vacuum-like dielectric permittivity.

It should be noted, that the close agreement between the exact calculation of interaction and its qualitative estimate is possible only because of the rapid decrease of the exciton energy for the lower excitonic states in TMD monolayer. On the contrary, in semiconductor heterostructures the energy decays quadratically, $E_n \sim n^{-2}$, obeying Rydberg rule. Thus the corresponding estimate predicts quadratic growth of the interaction strength. However the exact calculation shows the linear dependence of the exchange term on quantum number for quantum well [A2], meaning that the estimate is not reasonable for that case.

6.4. Exciton-electron scattering

Next, we consider the gated TMD monolayer with an excess of free electrons, which can interact with optically injected excitons. This nonlinear process is especially relevant for modern TMD experiments [255], can contribute to the exciton line broadening [254], and determines the physics of TMD exciton-polarons [264]. We proceed with the calculation of the exciton scattering with conduction band electrons. We restrict the consideration to s states, noting that for p-type excitons the results expected to be similar. The conduction band electron wave function is given by a plane wave $f_{\mathbf{K}}(\rho) = (1/\sqrt{A})e^{i\mathbf{K}\rho}$, where $\vec{K}$ denotes an electron momentum. We consider the process of Coulomb scattering of an exciton with a conduction electron, corresponding to the momentum transfer process

$$(n, \mathbf{Q}) + (\mathbf{K}) \rightarrow (n, \mathbf{Q} + \mathbf{q}) + (\mathbf{K} - \mathbf{q}). \tag{6.10}$$

The possible interaction channels include the direct interaction and the electron exchange term, as shown in Fig. 6.2(e,f). Correspondingly, one can present the total interaction as a sum of the direct and electron exchange constituents:

$$\begin{aligned} U(n, \mathbf{Q}, \mathbf{K}, \mathbf{q}) &= U_{dir}(n, q) + U_{exch}(n, \mathbf{q}, \mathbf{K} - \beta_e \mathbf{Q}) \\ &= \frac{e^2}{4\pi\varepsilon_0}\frac{\lambda_1}{A}\left[u_{dir}(n, q\lambda_1) + u_{exch}(n, q\lambda_1, (K - \beta_e Q)\lambda_1)\right], \end{aligned} \tag{6.11}$$

where the explicit form of corresponding terms is given in Appendix B3. It should be noted that the described approach is in agreement with the method previously used to characterize the exciton-electron scattering in quantum well heterostructures [274]. We calculated the scattering of the free electron with the ground and excited state

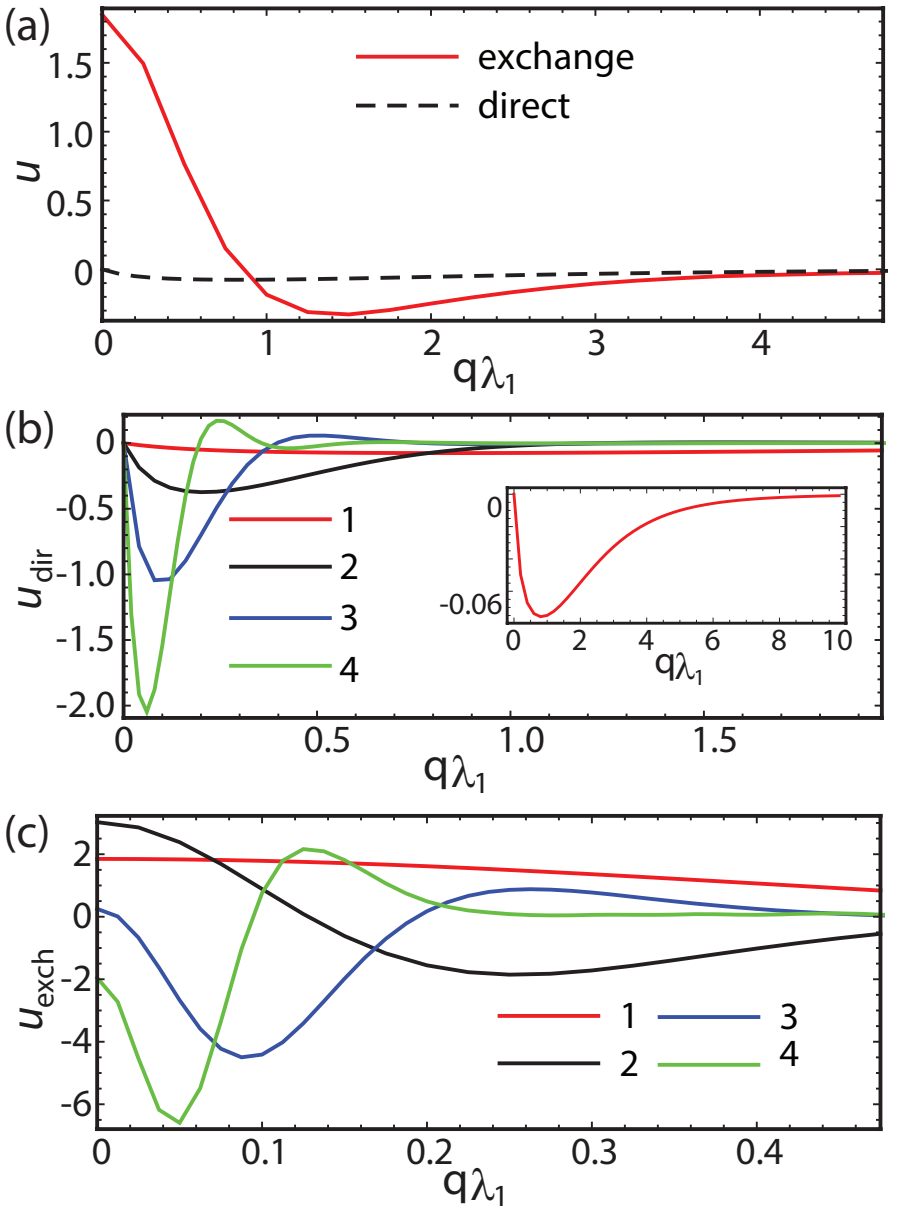

Figure 6.5: Exciton electron interaction energy as a function of transferred momentum. Ground state direct and exchange interactions (a), direct (b), and exchange(c) interaction of the excited states.

TMD excitons. Without the loss of generality, it is convenient to put the condition $\mathbf{K} - \beta_e \mathbf{Q} = 0$. Fig. 6.5(a) illustrates the direct and exchange terms of $1s$ exciton scattering with the electron. Similarly to QW heterostructure, the interaction is governed by dominant exchange contribution. Fig. 6.5(b,c) show the direct and exchange interaction of excited excitons with electron, respectively. One can see that, similarly to the exciton-exciton interaction, both components of scattering amplitudes increase with principal quantum number, conserving the domination of exchange component. An additional feature is that unlike the ground state, for the excited states the interaction is attractive and has maxima appearing at intermediate exchange momenta. Additionally, with the increase of quantum number both interaction components become more peak shaped.

6.5. Conclusion

In conclusion, we calculated the exciton-exciton and exciton-electron scattering processes in transition metal dichalcogenide monolayers. We found that unusual screening of the Coulomb interaction characteristic to monolayers leads to non-monotonic dependence of the exchange interaction on the transferred momentum. We have shown that contrary to the conventional quantum well excitons, in the considered structure the interaction can be accurately estimated by a simple analytical formula. It is proportional to a product of the exciton binding energy and the square of exciton radius, and exhibits linear growth with the principal quantum number of exciton. Additionally, we calculate the exciton-electron interaction in TMD monolayers, relevant for the system with excess of free electrons. This interaction is characterized by dominant attractive contribution of the exchange component, increasing with the excitation number. The results provide quantitative description for nonlinear effects of TMD excitons, and are of high importance for nonlinear optoelectronic devices based on monolayer semiconductor structures.

7. Conclusions

In conclusion, in the current thesis we discussed various optical phenomena in low-dimensional semiconductor structures.

The performed research can be classified into two branches. First of all, we have addressed two-level quantum systems with broken time-reversal symmetry, electromagnetically dressed by external laser field. The unique property of such systems consists in nonzero diagonal dipole matrix elements. As a two-level system, we employ III-nitride quantum dot, where the asymmetry stems from the material lattice structure. On one hand, we show that the dressing by a bichromatic field with near-resonant and off-resonant components completely rearranges the fluorescence spectra of the structure. Namely, the well-known Mollow triplet is in this case replaced by an infinite set of triplets, positions and strengths of which are very sensitive to the amplitudes and frequencies of the dressing field components, allowing a precise control of radiated emission properties.

On the other hand, we have proposed a scheme of terahertz laser on the basis of an ensemble of asymmetric quantum dots. The effect is profited by the evidence, that the electromagnetic dressing of asymmetric systems opens up optical transitions on Rabi frequency between the levels belonging to the same manifold in the ladder of dressed states. Rabi frequency in the discussed structures typically lies in terahertz range, and can be tuned by the choice of frequency detuning and amplitude of the dressing field. The amplification of emission is achieved by embedding the system into high quality cavity of the corresponding spectral range, represented by photonic crystal slab with disorder.

The second branch of the investigations is devoted to collective effects for excitons in quantum wells. We first address the phenomenon of Bose-Einstein condensation. It is well known, that while the condensation of exciton-polaritons nowadays can be easily achieved, the condensation of spatially indirect excitons still remains challenging task. At the same time, the concepts of indirect excitons and exciton-polaritons has been recently merged in so-called dipolariton systems, consisting of coupled double quantum wells embedded into cavity. Here we propose the protocol of condensation of indirect excitons, consisting in two steps. In the first stage we prepare a condensate of exciton-polaritons, and then transform it to a condensate of indirect excitons by coherent population transfer. The process is governed by tuning the strength of external bias applied to the structure.

In the rest of the thesis we focus on the study of the interactions between excitons being in excited (Rydberg) states. For this purpose we modify the existing scattering theory of two-dimensional excitons in quantum wells, in order to account the excited states. Quite surprisingly, the calculations unveiled an attractive nature of interactions for excited states, while for the ground state it is repulsive. Additionally we mention the increase of the interaction strength by at least order of magnitude, as well as its linear dependence on exciton principal quantum number for higher states. The obtained results open the way for obtaining strongly nonlinear Bose gases.

Finally, we apply the above described approach to calculate the interaction between excited excitonic states in transition metal dichalcogenide monolayers. The latter represents itself ideal testbed for investigations on Rydberg excitonic states, stemming from the binding energy of several hundreds of meV. This fact allows easy optical addressing of highly excited states. An additional peculiarity of monolayers consists in unusual Coulomb interaction potential, coming from the discontinuities of dielectric permittivity on the interfaces of monolayer with substrate from one side and with surrounding media on the other side. Particularly it leads to non-monotonous dependence of the interactions on the exchange momenta, which can potentially lead to emerge of various intriguing collective phenomena, such as supersolidity.

A. Equations of motion in first order mean field theory

Here we present the derivation of equations for time dynamics of the system [Eqs. (4)-(7) in the main text].

Coherent part. The coherent part of dynamics for cavity photon occupation number $\langle\hat{a}\rangle$ can be found as

$$\left.\frac{\partial\langle\hat{a}\rangle}{\partial t}\right|_{coh} = \frac{i}{\hbar}Tr\{\hat{a}[\rho,\hat{H}_{coh}]\} = \frac{i}{\hbar}Tr\{\rho[\hat{H}_{coh},\hat{a}]\} \tag{A1}$$
$$= \frac{i}{\hbar}Tr\{\rho(-\hbar\omega_C\hat{a} - \frac{\hbar\Omega}{2}\hat{b})\} = -i\omega_C\langle\hat{a}\rangle - i\frac{\Omega}{2}\langle\hat{b}\rangle.$$

In the same fashion for expectation values of operators $\hat{b}$, $\hat{c}$ we have

$$\left.\frac{\partial\langle\hat{b}\rangle}{\partial t}\right|_{coh} = -i\omega_{DX}\langle\hat{b}\rangle - i\frac{\Omega}{2}\langle\hat{a}\rangle + i\frac{J}{2}\langle\hat{c}\rangle, \tag{A2}$$

$$\left.\frac{\partial\langle\hat{c}\rangle}{\partial t}\right|_{coh} = -i\omega_{IX}\langle\hat{c}\rangle + i\frac{J}{2}\langle\hat{b}\rangle. \tag{A3}$$

Dissipation. To describe the incoherent processes the master equation approach with dissipators written in Lindblad form can be used.[43] Particularly, the decay of cavity mod can be treated as

$$\left.\frac{\partial\langle\hat{a}\rangle}{\partial t}\right|_{dis} = Tr\{\hat{a}\hat{\mathcal{L}}_{\hat{a}}^{(dis)}\rho\} = Tr\{\hat{a}\frac{\gamma_C}{2}(2\hat{a}\rho\hat{a}^\dagger - \hat{a}^\dagger\hat{a}\rho - \rho\hat{a}^\dagger\hat{a})\}$$
$$= \frac{\gamma_C}{2}Tr\{2\rho\hat{a}^\dagger\hat{a}\hat{a} - \rho\hat{a}\hat{a}^\dagger\hat{a} - \rho\hat{a}^\dagger\hat{a}\hat{a}\} = -\frac{\gamma_C}{2}\langle\hat{a}\rangle. \tag{A4}$$

Similarly,

$$\begin{aligned}\left.\frac{\partial\langle\hat{b}\rangle}{\partial t}\right|_{dis} &= -\frac{\gamma_{DX}}{2}\langle\hat{b}\rangle,\\ \left.\frac{\partial\langle\hat{c}\rangle}{\partial t}\right|_{dis} &= -\frac{\gamma_{IX}}{2}\langle\hat{c}\rangle,\\ \left.\frac{\partial n_R}{\partial t}\right|_{dis} &= -\gamma_R n_R.\end{aligned} \tag{A5}$$

Interaction with reservoir. The dynamics of the system caused by interaction with exciton reservoir can be calculated in Born-Markov approximation as

$$\left.\frac{\partial\langle\hat{b}\rangle}{\partial t}\right|_{int} = \delta_{\Delta E}\left\{\left\langle\left[\hat{H}^-,[\hat{b},\hat{H}^+]\right]\right\rangle + \left\langle\left[\hat{H}^+,[\hat{b},\hat{H}^-]\right]\right\rangle\right\}, \tag{A6}$$

where δ_R is inverse broadening of exciton states divided by $\hbar^2$. Calculation of commutators one by one gives $[\hat{b},\hat{H}^-] = 0$, $[\hat{b},\hat{H}^+] = R_{ph}\sum_k \hat{r}_k\hat{d}_k^+$, $\left[\hat{H}^+,[\hat{b},\hat{H}^-]\right] = R_{ph}^2\sum_k(\hat{r}_k^\dagger\hat{r}_k - \hat{d}_k^\dagger\hat{d}_k)\hat{b}$. Finally,

$$\begin{aligned}\left.\frac{\partial\langle\hat{b}\rangle}{\partial t}\right|_{int} &= \delta_{\Delta E}R_{ph}^2\sum_k(n_k^R - n_k^{ph})\langle\hat{b}\rangle\\ &= \delta_{\Delta E}R_{ph}^2\left(N_R - \sum_k n_k^{ph}\right)\langle\hat{b}\rangle.\end{aligned} \tag{A7}$$

In the same way for reservoir states we get

$$\begin{aligned}\left.\frac{\partial N_R}{\partial t}\right|_{int} &= \sum_k\left.\frac{\partial n_k^R}{\partial t}\right|_{int}\\ &= \sum_k\left\{\left\langle\left[\hat{H}^-,[\hat{r}^\dagger\hat{r},\hat{H}^+]\right]\right\rangle + \left\langle\left[\hat{H}^+,[\hat{r}^\dagger\hat{r},\hat{H}^-]\right]\right\rangle\right\}\\ &= -2\delta_{\Delta E}R_{ph}^2\left(|\langle\hat{b}\rangle|^2N_R + \sum_k[(n_k^{ph}+1)n_k^R - |\langle\hat{b}\rangle|^2n_k^{ph}]\right).\end{aligned} \tag{A8}$$

Here the relevant term corresponds to the stimulated scattering between reservoir and coherent mode, while spontaneous scattering can be usually neglected.

Incoherent pump. The pump of reservoir can be introduced using the Lindblad superoperator for incoherent pumping of each reservoir state with momentum q, and is

given by:[207]

$$\left.\frac{\partial n_q^R}{\partial t}\right|_{pump} = Tr\left\{\hat{r}_q^\dagger \hat{r}_q \sum_k P_k(t)\left(\hat{r}_k \rho \hat{r}_k^\dagger + \hat{r}_k^\dagger \rho \hat{r}_k - \hat{r}_k^\dagger \hat{r}_k \rho\right.\right. \tag{A9}$$
$$\left.\left. -\rho \hat{r}_k \hat{r}_k^\dagger\right)\right\} = P_q(t),$$

where $P_q(t)$ corresponds to an incoherent pumping rate of a single reservoir state. Considering identical reservoir states, we can write equation for the total reservoir occupation as

$$\left.\frac{\partial N_R}{\partial t}\right|_{pump} = \sum_q \left.\frac{\partial n_q^R}{\partial t}\right|_{pump} = \sum_q P_q(t) \equiv P(t), \tag{A10}$$

where we defined the total incoherent pumping rate $P(t)$ as a sum of single state pumps.

Combining the all contributions, for the time dynamics we come to the system of coupled equations (4)-(7).

B. Matrix elements for Coulomb scattering of Rydberg excitons

B.1. Quantum well excitons

A two-dimensional exciton in nl state with center of mass wave vector $\mathbf{Q}$ is described by the wavefunctions (1) and (2) of the main text, corresponding to center of mass and internal motions, respectively. The spin degree of freedom can be introduced in the following way. The total angular momentum projection of conduction electron on the growth axis is $s_e = \pm 1/2$. In the current work we restrict ourselves with the consideration of heavy-hole exctions. The angular momentum projection of heavy holes is $j_h = \pm 3/2$. Correspondingly, we have four independent heavy-hole exciton states: the dipole-active states $|J_z = \pm 1\rangle = |s_e = \mp 1/2, j_h = \pm 3/2\rangle$, and the dark states $|J_z = \pm 2\rangle = |s_e = \pm 1/2, j_h = \pm 3/2\rangle$. Further, in a general case exciton state with total momentum $|S\rangle$ can be defined as $\chi_S(s_e, j_h) = \langle s_e, j_h|S\rangle$ (see e.g. Ref. [14] for a detailed description).

We proceed considering the Coloumb scattering of excitons. We are interested in the processes of elastic scattering which conserve total spin and principal quantum numbers of excitons. They correspond to scattering processed described as:

$$(nl, \mathbf{Q}, S) + (n'l, \mathbf{Q}', S) \to (nl, \mathbf{Q} + \mathbf{q}, S) + (n'l, \mathbf{Q}' - \mathbf{q}, S), \tag{B1.1}$$

where we defined a distinct exciton spin state $|S\rangle = |s, j\rangle$, yielding $\chi_S(s_e, j_h) = \langle s_e, j_h|S\rangle = \delta_{s_e,s}\delta_{j_h,j}$.

Within the Hartree-Fock approximation, the two-exciton initial state having the same

spin is described by the following wave function:

$$\begin{aligned}
&\Phi^{S}_{\mathbf{Q}\mathbf{Q}'nn'}(\mathbf{r}_e, s_e, \mathbf{r}_h, j_h, \mathbf{r}_{e'}, s_{e'}, \mathbf{r}_{h'}, j_{h'}) = \frac{1}{\sqrt{2}}\left\{\frac{1}{\sqrt{2}}\left[\Psi_{\mathbf{Q},n}(\mathbf{r}_e, \mathbf{r}_h)\chi_S(s_e, s_h)\right.\right.\\
&\left.\Psi_{\mathbf{Q}',n'}(\mathbf{r}_{e'}, \mathbf{r}_{h'})\chi_S(s_{e'}, s_{h'}) + \Psi_{\mathbf{Q},n}(\mathbf{r}_{e'}, \mathbf{r}_{h'})\chi_S(s_{e'}, s_{h'})\Psi_{\mathbf{Q}',n'}(\mathbf{r}_e, \mathbf{r}_h)\chi_S(s_e, s_h)\right]\\
&-\frac{1}{\sqrt{2}}\left[\Psi_{\mathbf{Q},n}(\mathbf{r}_{e'}, \mathbf{r}_h)\chi_S(s_{e'}, s_h)\Psi_{\mathbf{Q}',n'}(\mathbf{r}_e, \mathbf{r}_{h'})\chi_S(s_e, s_{h'})\right.\\
&\left.\left.+\Psi_{\mathbf{Q},n}(\mathbf{r}_e, \mathbf{r}_{h'})\chi_S(s_e, s_{h'})\Psi_{\mathbf{Q}',n'}(\mathbf{r}_{e'}, \mathbf{r}_h)\chi_S(s_{e'}, s_h)\right]\right\} = \delta_{s_e,s}\delta_{s_{e'},s}\delta_{j_h,j}\delta_{j_{h'},j}\\
&\left\{\frac{1}{2}\left[\Psi_{\mathbf{Q},n}(\mathbf{r}_e, \mathbf{r}_h)\Psi_{\mathbf{Q}',n'}(\mathbf{r}_{e'}, \mathbf{r}_{h'}) + \Psi_{\mathbf{Q},n}(\mathbf{r}_{e'}, \mathbf{r}_{h'})\Psi_{\mathbf{Q}',n'}(\mathbf{r}_e, \mathbf{r}_h)\right]\right.\\
&\left.-\frac{1}{2}\left[\Psi_{\mathbf{Q},n}(\mathbf{r}_{e'}, \mathbf{r}_h)\Psi_{\mathbf{Q}',n'}(\mathbf{r}_e, \mathbf{r}_{h'}) + \Psi_{\mathbf{Q},n}(\mathbf{r}_e, \mathbf{r}_{h'})\Psi_{\mathbf{Q}',n'}(\mathbf{r}_{e'}, \mathbf{r}_h)\right]\right\}.
\end{aligned} \tag{B1.2}$$

The Hamiltonian can be written in the form:

$$\hat{H} = \hat{H}_1(\mathbf{r}_e, \mathbf{r}_h) + \hat{H}_2(\mathbf{r}_{e'}, \mathbf{r}_{h'}) + V_{int}(\mathbf{r}_e, \mathbf{r}_h, \mathbf{r}_{e'}, \mathbf{r}_{h'}), \tag{B1.3}$$

where $\hat{H}_j$ corresponds to the energy of $j-$th exciton, and V_{int} denotes the Coulomb interaction potential between particles.

The intra-exciton terms read

$$\hat{H}_1(\mathbf{r}_e, \mathbf{r}_h) = -\frac{\hbar^2}{2m_e}\Delta_e - \frac{\hbar^2}{2m_h}\Delta_h - V(|\mathbf{r}_e - \mathbf{r}_h|), \tag{B1.4}$$

$$\hat{H}_2(\mathbf{r}_{e'}, \mathbf{r}_{h'}) = -\frac{\hbar^2}{2m_e}\Delta_{e'} - \frac{\hbar^2}{2m_h}\Delta_{h'} - V(|\mathbf{r}_{e'} - \mathbf{r}_{h'}|), \tag{B1.5}$$

and each consists of kinetic and potential energy contributions. $V(r) = \frac{e^2}{4\pi\varepsilon_0\varepsilon r}$ corresponds to the Coulomb interaction energy, screened by the static dielectric constant ε; ε_0 is the vacuum permittivity.

The inter-exciton interaction part can be written as

$$\begin{aligned}
V_{int}(\mathbf{r}_e, \mathbf{r}_h, \mathbf{r}_{e'}, \mathbf{r}_{h'}) = &- V(|\mathbf{r}_e - \mathbf{r}_{h'}|) - V(|\mathbf{r}_{e'} - \mathbf{r}_h|)\\
&+ V(|\mathbf{r}_e - \mathbf{r}_{e'}|) + V(|\mathbf{r}_h - \mathbf{r}_{h'}|),
\end{aligned} \tag{B1.6}$$

where four possible interactions are accounted. The scattering amplitude of the process

described by Eq. (B1.1) is given by the matrix element:

$$
\begin{aligned}
&H_{nn'mS}(\mathbf{Q},\mathbf{Q}',\mathbf{q}) = \int d^2\mathbf{r}_e \sum_{s_e} \int d^2\mathbf{r}_h \sum_{j_h} \int d^2\mathbf{r}_{e'} \sum_{s_{e'}} \int d^2\mathbf{r}_{h'} \sum_{j_{h'}} \\
&\Phi^{*S}_{\mathbf{Q}\mathbf{Q}'nn'}(\mathbf{r}_e,s_e,\mathbf{r}_h,j_h,\mathbf{r}_{e'},s_{e'},\mathbf{r}_{h'},j_{h'}) V_{int}(\mathbf{r}_e,\mathbf{r}_h,\mathbf{r}_{e'},\mathbf{r}_{h'}) \\
&\Phi^{S}_{\mathbf{Q}+\mathbf{q}\mathbf{Q}'-\mathbf{q}nn'}(\mathbf{r}_e,s_e,\mathbf{r}_h,j_h,\mathbf{r}_{e'},s_{e'},\mathbf{r}_{h'},j_{h'}) = \frac{1}{4}\delta_{s_e,s}\delta_{s_{e'},s}\delta_{j_h,j}\delta_{j_{h'},j} \\
&\Big[4\int d^2\mathbf{r}_e d^2\mathbf{r}_h d^2\mathbf{r}_{e'} d^2\mathbf{r}_{h'} \Psi^*_{\mathbf{Q},n}(\mathbf{r}_e,\mathbf{r}_h)\Psi^*_{\mathbf{Q}',n'}(\mathbf{r}_{e'},\mathbf{r}_{h'}) V_{int}(\mathbf{r}_e,\mathbf{r}_h,\mathbf{r}_{e'},\mathbf{r}_{h'}) \\
&\qquad\qquad \Psi_{\mathbf{Q}+\mathbf{q},n}(\mathbf{r}_e,\mathbf{r}_h)\Psi_{\mathbf{Q}'-\mathbf{q},n'}(\mathbf{r}_{e'},\mathbf{r}_{h'}) \\
&+4\int d^2\mathbf{r}_e d^2\mathbf{r}_h d^2\mathbf{r}_{e'} d^2\mathbf{r}_{h'} \Psi^*_{\mathbf{Q},n}(\mathbf{r}_e,\mathbf{r}_h)\Psi^*_{\mathbf{Q}',n'}(\mathbf{r}_{e'},\mathbf{r}_{h'}) V_{int}(\mathbf{r}_e,\mathbf{r}_h,\mathbf{r}_{e'},\mathbf{r}_{h'}) \\
&\qquad\qquad \Psi_{\mathbf{Q}+\mathbf{q},n}(\mathbf{r}_{e'},\mathbf{r}_{h'})\Psi_{\mathbf{Q}'-\mathbf{q},n'}(\mathbf{r}_e,\mathbf{r}_h) \\
&-4\int d^2\mathbf{r}_e d^2\mathbf{r}_h d^2\mathbf{r}_{e'} d^2\mathbf{r}_{h'} \Psi^*_{\mathbf{Q},n}(\mathbf{r}_e,\mathbf{r}_h)\Psi^*_{\mathbf{Q}',n'}(\mathbf{r}_{e'},\mathbf{r}_{h'}) V_{int}(\mathbf{r}_e,\mathbf{r}_h,\mathbf{r}_{e'},\mathbf{r}_{h'}) \\
&\qquad\qquad \Psi_{\mathbf{Q}+\mathbf{q},n}(\mathbf{r}_{e'},\mathbf{r}_h)\Psi_{\mathbf{Q}'-\mathbf{q},n'}(\mathbf{r}_e,\mathbf{r}_{h'}) \\
&-4\int d^2\mathbf{r}_e d^2\mathbf{r}_h d^2\mathbf{r}_{e'} d^2\mathbf{r}_{h'} \Psi^*_{\mathbf{Q},n}(\mathbf{r}_e,\mathbf{r}_h)\Psi^*_{\mathbf{Q}',n'}(\mathbf{r}_{e'},\mathbf{r}_{h'}) V_{int}(\mathbf{r}_e,\mathbf{r}_h,\mathbf{r}_{e'},\mathbf{r}_{h'}) \\
&\qquad\qquad \Psi_{\mathbf{Q}+\mathbf{q},n}(\mathbf{r}_e,\mathbf{r}_{h'})\Psi_{\mathbf{Q}'-\mathbf{q},n'}(\mathbf{r}_{e'},\mathbf{r}_h)\Big] \\
&= \delta_{s_e,s}\delta_{s_{e'},s}\delta_{j_h,j}\delta_{j_{h'},j}\left[H_{\rm dir}(n,n',\mathbf{Q},\mathbf{Q}',\mathbf{q}) + H^X_{\rm exch}(n,n',\mathbf{Q},\mathbf{Q}',\mathbf{q})\right. \\
&\qquad\qquad \left. + H^e_{\rm exch}(n,n',\mathbf{Q},\mathbf{Q}',\mathbf{q}) + H^h_{\rm exch}(n,n',\mathbf{Q},\mathbf{Q}',\mathbf{q})\right],
\end{aligned}
\tag{B1.7}
$$

where four terms correspond to direct interaction, exciton exchange, electron exchange, and hole exchange. They can be written explicitly as:

$$
\begin{aligned}
&H_{\rm dir}(n,n',m,\mathbf{q}) = \frac{\alpha_C}{A} I_{\rm dir}(n,n',m,\mathbf{q}) \\
&= \frac{\alpha_C}{A} \frac{(n-|m|-1)!(n'-|m|-1)!}{2^4\pi^2(n-1/2)^3(n'-1/2)^3(n+|m|-1)!(n'+|m|-1)!} \frac{(2\pi)^3}{\lambda_{\rm 2D} q} \\
&\int_0^\infty\int_0^\infty [-J_0(\beta_h\lambda_{\rm 2D}qx)J_0(\beta_e\lambda_{\rm 2D}qx') - J_0(\beta_e\lambda_{\rm 2D}qx)J_0(\beta_h\lambda_{\rm 2D}qx') \\
&\qquad +J_0(\beta_h\lambda_{\rm 2D}qx)J_0(\beta_h\lambda_{\rm 2D}qx') + J_0(\beta_e\lambda_{\rm 2D}qx)J_0(\beta_e\lambda_{\rm 2D}qx')] \\
&\qquad \left[\frac{x}{n-1/2}\right]^2 e^{-\frac{x}{n-1/2}} \left[L^{2|m|}_{n-|m|-1}\left(\frac{x}{n-1/2}\right)\right]^2 x dx \\
&\qquad \left[\frac{x'}{n'-1/2}\right]^2 e^{-\frac{x'}{n'-1/2}} \left[L^{2|m|}_{n'-|m|-1}\left(\frac{x'}{n'-1/2}\right)\right]^2 x' dx',
\end{aligned}
\tag{B1.8}
$$

$$
\begin{aligned}
&H^X_{\text{exch}}(n,n',m,\Delta\mathbf{Q},\mathbf{q}) = \frac{\alpha_C}{A} I^X_{\text{exch}}(n,n',m,\Delta\mathbf{Q},\mathbf{q}) \\
&= \frac{\alpha_C}{A} \frac{(n-|m|-1)!(n'-|m|-1)!}{2^4\pi^2(n-1/2)^3(n'-1/2)^3(n+|m|-1)!(n'+|m|-1)!} \\
&\int d^2\mathbf{x} d^2\mathbf{y}_1 d^2\mathbf{y}_2 e^{i(\Delta\mathbf{Q}-\mathbf{q})\lambda_{2\text{D}}[\beta_e\mathbf{y}_1+\beta_h\mathbf{y}_2+(\beta_h-\beta_e)\mathbf{x}]} \frac{x^2|\mathbf{y}_2-\mathbf{y}_1-\mathbf{x}|^2}{(n-1/2)^2(n'-1/2)^2} \\
&e^{-(x+|\mathbf{y}_2-\mathbf{y}_1-\mathbf{x}|)\left[\frac{1}{n-1/2}+\frac{1}{n'-1/2}\right]} L^{2|m|}_{n-|m|-1}\left(\frac{x}{n-1/2}\right) L^{2|m|}_{n'-|m|-1}\left(\frac{|\mathbf{y}_2-\mathbf{y}_1-\mathbf{x}|}{n'-1/2}\right) \\
&L^{2|m|}_{n-|m|-1}\left(\frac{|\mathbf{y}_2-\mathbf{y}_1-\mathbf{x}|}{n-1/2}\right) L^{2|m|}_{n'-|m|-1}\left(\frac{x}{n'-1/2}\right)\left[-\frac{1}{y_1}-\frac{1}{y_2}+\frac{1}{|\mathbf{y}_1+\mathbf{x}|}+\frac{1}{|\mathbf{y}_2-\mathbf{x}|}\right],
\end{aligned}
\tag{B1.9}
$$

$$
\begin{aligned}
&H^e_{\text{exch}}(n,n',m,\Delta\mathbf{Q},\mathbf{q}) = \frac{\alpha_C}{A} I^e_{\text{exch}}(n,n',m,\Delta\mathbf{Q},\mathbf{q}) \\
&= -\frac{\alpha_C}{A} \frac{(n-|m|-1)!(n'-|m|-1)!}{2^4\pi^2(n-1/2)^3(n'-1/2)^3(n+|m|-1)!(n'+|m|-1)!} \int d^2\mathbf{x} \\
&d^2\mathbf{y}_1 d^2\mathbf{y}_2 e^{i\beta_e\lambda_{2\text{D}}\Delta\mathbf{Q}(\mathbf{y}_1+\mathbf{x})} e^{i\lambda_{2\text{D}}\mathbf{q}[\beta_h\mathbf{y}_2-\beta_e\mathbf{y}_1-\mathbf{x}]} \left[\frac{x}{n-1/2}\frac{|\mathbf{y}_2-\mathbf{y}_1-\mathbf{x}|}{n'-1/2}\frac{y_1}{n-1/2}\frac{y_2}{n'-1/2}\right]^{|m|} \\
&e^{-\frac{x}{2n-1}} e^{-\frac{|\mathbf{y}_2-\mathbf{y}_1-\mathbf{x}|}{2n'-1}} e^{-\frac{y_1}{2n-1}} e^{-\frac{y_2}{2n'-1}} L^{2|m|}_{n-|m|-1}\left(\frac{x}{n-\frac{1}{2}}\right) L^{2|m|}_{n'-|m|-1}\left(\frac{|\mathbf{y}_2-\mathbf{y}_1-\mathbf{x}|}{n'-\frac{1}{2}}\right) \\
&L^{2|m|}_{n-|m|-1}\left(\frac{y_1}{n-\frac{1}{2}}\right) L^{2|m|}_{n'-|m|-1}\left(\frac{y_2}{n'-\frac{1}{2}}\right)\left[-\frac{1}{y_2}-\frac{1}{y_1}+\frac{1}{|\mathbf{y}_1+\mathbf{x}|}+\frac{1}{|\mathbf{y}_2-\mathbf{x}|}\right],
\end{aligned}
\tag{B1.10}
$$

$$
\begin{aligned}
&H^h_{\text{exch}}(n,n',m,\Delta\mathbf{Q},\mathbf{q}) = \frac{\alpha_C}{A} I^h_{\text{exch}}(n,n',m,\Delta\mathbf{Q},\mathbf{q}) \\
&= -\frac{\alpha_C}{A} \frac{(n-|m|-1)!(n'-|m|-1)!}{2^4\pi^2(n-1/2)^3(n'-1/2)^3(n+|m|-1)!(n'+|m|-1)!} \int d^2\mathbf{x} \\
&d^2\mathbf{y}_1 d^2\mathbf{y}_2 e^{i\beta_e\lambda_{2\text{D}}\Delta\mathbf{Q}(\mathbf{y}_2-\mathbf{x})} e^{i\lambda_{2\text{D}}\mathbf{q}[-\beta_h\mathbf{y}_2+\beta_e\mathbf{y}_1+\mathbf{x}]} \left[\frac{x}{n-1/2}\frac{|\mathbf{y}_2-\mathbf{y}_1-\mathbf{x}|}{n'-1/2}\frac{y_1}{n-1/2}\frac{y_2}{n'-1/2}\right]^{|m|} \\
&e^{-\frac{x}{2n-1}} e^{-\frac{|\mathbf{y}_2-\mathbf{y}_1-\mathbf{x}|}{2n'-1}} e^{-\frac{y_1}{2n-1}} e^{-\frac{y_2}{2n'-1}} L^{2|m|}_{n-|m|-1}\left(\frac{x}{n-\frac{1}{2}}\right) L^{2|m|}_{n'-|m|-1}\left(\frac{|\mathbf{y}_2-\mathbf{y}_1-\mathbf{x}|}{n'-\frac{1}{2}}\right) \\
&L^{2|m|}_{n-|m|-1}\left(\frac{y_1}{n-\frac{1}{2}}\right) L^{2|m|}_{n'-|m|-1}\left(\frac{y_2}{n'-\frac{1}{2}}\right)\left[-\frac{1}{y_2}-\frac{1}{y_1}+\frac{1}{|\mathbf{y}_1+\mathbf{x}|}+\frac{1}{|\mathbf{y}_2-\mathbf{x}|}\right],
\end{aligned}
\tag{B1.11}
$$

where we defined $\alpha_C \equiv e^2\lambda_{2\text{D}}/4\pi\varepsilon\varepsilon_0$. During the derivation the following radius vector transformations were used: $\rho = \mathbf{r}_e - \mathbf{r}_h$, $\mathbf{R} = \beta_e\mathbf{r}_e + \beta_h\mathbf{r}_h$, $\rho' = \mathbf{r}_{e'} - \mathbf{r}_{h'}$, $\mathbf{R}' = \beta_e\mathbf{r}_{e'} + \beta_h\mathbf{r}_{h'}$, $\xi = \mathbf{R} - \mathbf{R}'$, $\sigma = \frac{\mathbf{R}+\mathbf{R}'}{2}$, $\Delta\mathbf{Q} = \mathbf{Q}' - \mathbf{Q}$, $\mathbf{x} = \frac{\rho}{\lambda_{2\text{D}}}$, $\mathbf{x}' = \frac{\rho'}{\lambda_{2\text{D}}}$, $\mathbf{y}_1 = \frac{\xi-\beta_e\rho-\beta_h\rho'}{\lambda_{2\text{D}}}$, $\mathbf{y}_2 = \frac{\xi+\beta_h\rho+\beta_e\rho'}{\lambda_{2\text{D}}}$.

B.2. TMD monolayer excitons

A two-dimensional exciton in nl state with the center-of-mass wave vector $\mathbf{Q}$ is described by the wavefunctions given by Eqs. (6.3) and (6.5) in the main text, corresponding to internal and center of mass dynamics, respectively. Considering the states with parallel spin only, one may construct two exciton wave function in the form

$$\begin{aligned}\Phi_{\mathbf{Q},\mathbf{Q}',n}(\mathbf{r}_e,\mathbf{r}_h,\mathbf{r}_{e'},\mathbf{r}_{h'}) = &\frac{1}{2}\left[\Psi_{\mathbf{Q},n}(\mathbf{r}_e,\mathbf{r}_h)\Psi_{\mathbf{Q}',n}(\mathbf{r}_{e'},\mathbf{r}_{h'}) + \Psi_{\mathbf{Q},n}(\mathbf{r}_{e'},\mathbf{r}_{h'})\Psi_{\mathbf{Q}',n}(\mathbf{r}_e,\mathbf{r}_h)\right] \\ &- \frac{1}{2}\left[\Psi_{\mathbf{Q},n}(\mathbf{r}_{e'},\mathbf{r}_h)\Psi_{\mathbf{Q}',n}(\mathbf{r}_e,\mathbf{r}_{h'}) + \Psi_{\mathbf{Q},n}(\mathbf{r}_e,\mathbf{r}_{h'})\Psi_{\mathbf{Q}',n}(\mathbf{r}_{e'},\mathbf{r}_h)\right],\end{aligned} \tag{B2.1}$$

where we omit the magnteic quantum number m for the sake of shortness. The exciton-exciton interaction Hamiltonian read as

$$\begin{aligned}V_{int}(\mathbf{r}_e,\mathbf{r}_h,\mathbf{r}_{e'},\mathbf{r}_{h'}) = &- V(|\mathbf{r}_e-\mathbf{r}_{h'}|) - V(|\mathbf{r}_{e'}-\mathbf{r}_h|) \\ &+ V(|\mathbf{r}_e-\mathbf{r}_{e'}|) + V(|\mathbf{r}_h-\mathbf{r}_{h'}|),\end{aligned} \tag{B2.2}$$

where all possible interparticle interactions are accounted. The scattering amplitude of the process described by Eq. (6.6) in main text is given by the matrix element

$$\begin{aligned}V_n(\mathbf{Q},\mathbf{Q}',\mathbf{q}) = &\int d^2\mathbf{r}_e d^2\mathbf{r}_h d^2\mathbf{r}_{e'} d^2\mathbf{r}_{h'} \Phi^*_{\mathbf{Q},\mathbf{Q}',n}(\mathbf{r}_e,\mathbf{r}_h,\mathbf{r}_{e'},\mathbf{r}_{h'}) \\ &\times V_{int}(\mathbf{r}_e,\mathbf{r}_h,\mathbf{r}_{e'},\mathbf{r}_{h'})\Phi_{\mathbf{Q}+\mathbf{q},\mathbf{Q}'-\mathbf{q},n}(\mathbf{r}_e,\mathbf{r}_h,\mathbf{r}_{e'},\mathbf{r}_{h'}) \\ = &\int d^2\mathbf{r}_e d^2\mathbf{r}_h d^2\mathbf{r}_{e'} d^2\mathbf{r}_{h'} \Psi^*_{\mathbf{Q},n}(\mathbf{r}_e,\mathbf{r}_h)\Psi^*_{\mathbf{Q}',n}(\mathbf{r}_{e'},\mathbf{r}_{h'})V_{int}(\mathbf{r}_e,\mathbf{r}_h,\mathbf{r}_{e'},\mathbf{r}_{h'}) \\ &\times \Psi_{\mathbf{Q}+\mathbf{q},n}(\mathbf{r}_e,\mathbf{r}_h)\Psi_{\mathbf{Q}'-\mathbf{q},n}(\mathbf{r}_{e'},\mathbf{r}_{h'}) \\ &+ \int d^2\mathbf{r}_e d^2\mathbf{r}_h d^2\mathbf{r}_{e'} d^2\mathbf{r}_{h'} \Psi^*_{\mathbf{Q},n}(\mathbf{r}_e,\mathbf{r}_h)\Psi^*_{\mathbf{Q}',n}(\mathbf{r}_{e'},\mathbf{r}_{h'})V_{int}(\mathbf{r}_e,\mathbf{r}_h,\mathbf{r}_{e'},\mathbf{r}_{h'}) \\ &\times \Psi_{\mathbf{Q}+\mathbf{q},n}(\mathbf{r}_{e'},\mathbf{r}_{h'})\Psi_{\mathbf{Q}'-\mathbf{q},n}(\mathbf{r}_e,\mathbf{r}_h) \\ &- \int d^2\mathbf{r}_e d^2\mathbf{r}_h d^2\mathbf{r}_{e'} d^2\mathbf{r}_{h'} \Psi^*_{\mathbf{Q},n}(\mathbf{r}_e,\mathbf{r}_h)\Psi^*_{\mathbf{Q}',n}(\mathbf{r}_{e'},\mathbf{r}_{h'})V_{int}(\mathbf{r}_e,\mathbf{r}_h,\mathbf{r}_{e'},\mathbf{r}_{h'}) \\ &\times \Psi_{\mathbf{Q}+\mathbf{q},n}(\mathbf{r}_{e'},\mathbf{r}_h)\Psi_{\mathbf{Q}'-\mathbf{q},n}(\mathbf{r}_e,\mathbf{r}_{h'}) \\ &- \int d^2\mathbf{r}_e d^2\mathbf{r}_h d^2\mathbf{r}_{e'} d^2\mathbf{r}_{h'} \Psi^*_{\mathbf{Q},n}(\mathbf{r}_e,\mathbf{r}_h)\Psi^*_{\mathbf{Q}',n}(\mathbf{r}_{e'},\mathbf{r}_{h'})V_{int}(\mathbf{r}_e,\mathbf{r}_h,\mathbf{r}_{e'},\mathbf{r}_{h'}) \\ &\times \Psi_{\mathbf{Q}+\mathbf{q},n}(\mathbf{r}_e,\mathbf{r}_{h'})\Psi_{\mathbf{Q}'-\mathbf{q},n}(\mathbf{r}_{e'},\mathbf{r}_h) \\ = &\, V_{\rm dir}(n,\mathbf{Q},\mathbf{Q}',\mathbf{q}) + V^X_{\rm exch}(n,\mathbf{Q},\mathbf{Q}',\mathbf{q}) + V^e_{\rm exch}(n,\mathbf{Q},\mathbf{Q}',\mathbf{q}) + V^h_{\rm exch}(n,\mathbf{Q},\mathbf{Q}',\mathbf{q}),\end{aligned} \tag{B2.3}$$

where four terms correspond to direct interaction, exciton exchange, electron exchange, and hole exchange. Before proceeding further, one can note that for the case when $\mathbf{Q} = \mathbf{Q}'$, we have

$$V^X_{\rm exch}(n, \mathbf{Q}, \mathbf{Q}, \mathbf{q}) = V_{\rm dir}(n, \mathbf{Q}, \mathbf{Q}, \mathbf{q}),$$
$$V^h_{\rm exch}(n, \mathbf{Q}, \mathbf{Q}, \mathbf{q}) = V^e_{\rm exch}(n, \mathbf{Q}, \mathbf{Q}, \mathbf{q}). \tag{B2.4}$$

Introducing dimensionless functions

$$V(r) = -\frac{e_1 e_2}{4\pi\varepsilon_0 \lambda_n} \frac{1}{r_0/\lambda_n} \left[\ln\left(\frac{r/\lambda_n}{r/\lambda_n + r_0/\lambda_n} \right) - (\gamma - \ln 2) e^{-\frac{r/\lambda_n}{r_0/\lambda_n}} \right] = \frac{e_1 e_2}{4\pi\varepsilon_0 \lambda_n} \widetilde{V}\left(\frac{r}{\lambda_n} \right), \tag{B2.5}$$

$$\psi(r) = \frac{1}{\lambda_n} \widetilde{\psi}_n \left(\frac{r}{\lambda_n} \right), \tag{B2.6}$$

one may write the direct term in the explicit form as

$$V_{\rm dir}(n, q) = \frac{e^2}{4\pi\varepsilon_0} \frac{\lambda_1}{A} I_{\rm dir}(n, q) = \frac{e^2}{4\pi\varepsilon_0} \frac{\lambda_1}{A} \lambda \int d^2\mathbf{x} d^2\mathbf{x}' d^2\xi e^{i\mathbf{q}\lambda_1\lambda\xi} \widetilde{\psi}^2_n(x) \widetilde{\psi}^2_n(x')$$
$$\left[-\widetilde{V}(|\xi + \beta_h \mathbf{x} + \beta_e \mathbf{x}'|) - \widetilde{V}(|\xi - \beta_e \mathbf{x} - \beta_h \mathbf{x}'|) + \widetilde{V}(|\xi + \beta_h(\mathbf{x} - \mathbf{x}'|) + \widetilde{V}(|\xi - \beta_e(\mathbf{x} - \mathbf{x}'|) \right], \tag{B2.7}$$

where we have introduced the notations $\mathbf{r} = \mathbf{r}_e - \mathbf{r}_h$, $\mathbf{R} = \beta_e \mathbf{r}_e + \beta_h \mathbf{r}_h$, $\mathbf{r}' = \mathbf{r}_{e'} - \mathbf{r}_{h'}$, $\mathbf{R}' = \beta_e \mathbf{r}_{e'} + \beta_h \mathbf{r}_{h'}$, $\xi = \frac{\mathbf{R} - \mathbf{R}'}{\lambda_n}$, $\mathbf{x} = \frac{\mathbf{r}}{\lambda_n}$, $\mathbf{x}' = \frac{\mathbf{r}'}{\lambda_n}$, $\lambda = \frac{\lambda_n}{\lambda_1}$. The remaining step consists in performing integrations. Considering the first term, we can rewrite integral as

$$\int d^2\mathbf{x} d^2\mathbf{x}' d^2\xi e^{i\mathbf{q}\lambda_1\lambda\xi} \widetilde{\psi}^2_n(x) \widetilde{\psi}^2_n(x') \widetilde{V}(|\xi + \beta_h \mathbf{x} + \beta_e \mathbf{x}'|)$$
$$= \int d^2\tau e^{i\mathbf{q}\lambda_1\lambda\tau} \widetilde{V}(\tau) \int d^2\mathbf{x} e^{-i\mathbf{q}\lambda_1\lambda\beta_h\mathbf{x}} \widetilde{\psi}^2_n(x) \int d^2\mathbf{x}' e^{-i\mathbf{q}\lambda_1\lambda\beta_e\mathbf{x}'} \widetilde{\psi}^2_n(x')$$
$$= (2\pi)^3 \int_0^\infty J_0(q\lambda_1\lambda\tau) \widetilde{V}(\tau) \tau d\tau \int_0^\infty J_0(q\lambda_1\lambda\beta_h x) \widetilde{\psi}_n(x) x dx \int_0^\infty J_0(q\lambda_1\lambda\beta_e x') \widetilde{\psi}_n(x') x' dx'$$
$$= (2\pi)^3 V_{q\lambda_1\lambda} g_n(\lambda\beta_h q\lambda_1) g_n(\lambda\beta_e q\lambda_1). \tag{B2.8}$$

Calculating the remaining terms in the same way, we arrive to

$$I_{\rm dir}(n, q) = \lambda(2\pi)^3 V_{\lambda\lambda_1 q} \left[g_n(\beta_h \lambda\lambda_1 q) - g_n(\beta_e \lambda\lambda_1 q) \right]^2. \tag{B2.9}$$

The electron exchange integral after some simplifications takes a form

$$V^e_{\rm exch}(n, q) = \frac{e^2}{4\pi\varepsilon_0} \frac{\lambda_1}{A} I^e_{\rm exch}(n, q) = \frac{e^2}{4\pi\varepsilon_0} \frac{\lambda_1}{A} \lambda \int d^2\mathbf{x} d^2\mathbf{y}_1 d^2\mathbf{y}_2 e^{i\mathbf{q}\lambda_1\lambda(\beta_h\mathbf{y}_1 - \beta_e\mathbf{y}_2 - \mathbf{x})} \widetilde{\psi}_n(x)$$
$$\widetilde{\psi}_n(y_1) \widetilde{\psi}_n(y_2) \widetilde{\psi}_n(|\mathbf{y}_2 - \mathbf{y}_1 - \mathbf{x}|) \left[\widetilde{V}(y_1) + \widetilde{V}(y_2) - \widetilde{V}(|\mathbf{y}_1 + \mathbf{x}|) - \widetilde{V}(|\mathbf{y}_2 - \mathbf{x}|) \right]. \tag{B2.10}$$

B.3. TMD monolayer excitons scattering with electrons

In the following section we demonstrate the derivation of the exciton-electron interaction matrix elements. The wave function of an exciton-electron pair can be written in the form

$$F_{\mathbf{Q},\mathbf{K},n}(\mathbf{r}_1,\mathbf{r}_2,\mathbf{r}_h) = \frac{1}{\sqrt{2}}\left[\psi_{\mathbf{Q},n}(\mathbf{r}_1,\mathbf{r}_h)f_{\mathbf{K}}(\mathbf{r}_2) - \psi_{\mathbf{Q},n}(\mathbf{r}_2,\mathbf{r}_h)f_{\mathbf{K}}(\mathbf{r}_1)\right] \tag{B3.1}$$

The interaction Hamiltonian is given by

$$\hat{U}_{int} = -V(|\mathbf{r}_1-\mathbf{r}_h|) - V(|\mathbf{r}_2-\mathbf{r}_h|) + V(|\mathbf{r}_1-\mathbf{r}_2|). \tag{B3.2}$$

The full scattering matrix element read as

$$\begin{aligned} U_n^{full}(\mathbf{Q},\mathbf{K},\mathbf{q}) &= \int d^2\mathbf{r}_1 d^2\mathbf{r}_2 d^2\mathbf{r}_h F^*_{\mathbf{Q},\mathbf{K},n}(\mathbf{r}_1,\mathbf{r}_2,\mathbf{r}_h)\hat{U}_{int}(\mathbf{r}_1,\mathbf{r}_2,\mathbf{r}_h)F_{\mathbf{Q}+\mathbf{q},\mathbf{K}-\mathbf{q},n}(\mathbf{r}_1,\mathbf{r}_2,\mathbf{r}_h) \\ &= \frac{1}{2A^2}\int d^2\mathbf{r}_1 d^2\mathbf{r}_2 d^2\mathbf{r}_h \hat{U}_{int}(\mathbf{r}_1,\mathbf{r}_2,\mathbf{r}_h)\Big\{e^{i\mathbf{q}(\beta_e\mathbf{r}_1+\beta_h\mathbf{r}_h-\mathbf{r}_2)}\psi_n^2(\mathbf{r}_1-\mathbf{r}_h) \\ &+ e^{i\mathbf{q}(\beta_e\mathbf{r}_2+\beta_h\mathbf{r}_h-\mathbf{r}_1)}\psi_n^2(\mathbf{r}_2-\mathbf{r}_h) - \psi_n(\mathbf{r}_1-\mathbf{r}_h)\psi_n(\mathbf{r}_2-\mathbf{r}_h) \\ &\times\left[e^{i(\alpha\mathbf{Q}-\mathbf{K})(\mathbf{r}_2-\mathbf{r}_1)}e^{i\mathbf{q}(\beta_e\mathbf{r}_1+\beta_h\mathbf{r}_h-\mathbf{r}_2)} + e^{-i(\alpha\mathbf{Q}-\mathbf{K})(\mathbf{r}_2-\mathbf{r}_1)}e^{i\mathbf{q}(\beta_e\mathbf{r}_2+\beta_h\mathbf{r}_h-\mathbf{r}_1)}\right]\Big\}. \end{aligned} \tag{B3.3}$$

Here we note that the above expression contains terms contributing to the exciton internal dynamics. For instance, the term $-V(|\mathbf{r}_1-\mathbf{r}_h|)e^{i\mathbf{q}(\beta_e\mathbf{r}_1+\beta_h\mathbf{r}_h-\mathbf{r}_2)}\psi_n^2(\mathbf{r}_1-\mathbf{r}_h)$ describes the interaction between hole and electron $\mathbf{r}_1$, forming exciton, while the second electron is not involved in the system. Hence, this term should be neglected. Analogously, excluding all the extra terms and after corresponding simplifications, one finally arrives to the sum of direct and exchange components

$$\begin{aligned} U_n(\mathbf{Q},\mathbf{K},\mathbf{q}) &= U_{dir}(n,q) + U_{exch}(n,\mathbf{q},\mathbf{K}-\beta_e\mathbf{Q}) \\ &= \frac{e^2}{4\pi\varepsilon_0}\frac{\lambda_1}{A}\left[u_{dir}(n,q\lambda_1) + u_{exch}(n,q\lambda_1,(K-\beta_eQ)\lambda_1)\right], \end{aligned} \tag{B3.4}$$

where

$$\begin{aligned} u_{dir}(n,q) &= \lambda(2\pi)^2 V_{q\lambda_1\lambda} \\ &\times\left[g_n(\lambda\beta_h q\lambda_1) - g_n(\lambda\beta_e q\lambda_1)\right], \end{aligned} \tag{B3.5}$$

and

$$u_{exch}(n,q) = \lambda\int d^2\chi d^2\mathbf{x} e^{-i\mathbf{q}\lambda_1\lambda(\alpha\chi+\mathbf{x})}e^{i(\mathbf{K}-\alpha\mathbf{Q})\lambda_1\lambda(\chi+\mathbf{x})}\left[-\widetilde{V}(\chi)+\widetilde{V}(|\chi+\mathbf{x}|)\right]\widetilde{\psi}_n(\chi)\widetilde{\psi}_n(x), \tag{B3.6}$$

with $\chi = \frac{\mathbf{R}-\mathbf{r}_2-\beta_e\mathbf{r}}{\lambda_n}$.

List of publications

(**Relevant to the current Thesis**:)

[A1] V. Shahnazaryan, O. Kyriienko, I.A. Shelykh, Adiabatic preparation of a cold exciton condensate, Physical Review B **91**, 085302 (2015).

[A2] V. Shahnazaryan, O. Kyriienko, I.A. Shelykh, Attractive Coulomb interaction of two-dimensional Rydberg excitons, Physical Review B **93**, 245302 (2016).

[A3] I.Y. Chestnov, V.A. Shakhnazaryan, I.A. Shelykh, A.P. Alodjants, Ensemble of asymmetric quantum dots in a cavity as a terahertz laser source, JETP letters **104**, 169-174 (2016).

[A4] G.Yu. Kryuchkyan, V. Shahnazaryan, O.V. Kibis, and I.A. Shelykh, Resonance fluorescence from an asymmetric quantum dot dressed by a bichromatic electromagnetic field, Phys. Rev. A **95**, 013834 (2017).

[A5] V. Shahnazaryan, I. Iorsh, I.A. Shelykh, O. Kyriienko, Exciton-exciton interaction in transition-metal dichalcogenide monolayers, Phys. Rev. B **96**, 115409 (2017).

[A6] I.Y. Chestnov, V.A. Shahnazaryan, A.P. Alodjants, I.A. Shelykh, THz Lasing in ensemble of asymmetric quantum dots (submitted to ACS Photonics, 2017).

(**Other related publications**:)

[A7] V. Shahnazaryan, S. Morina, S. Tarasenko, I.A. Shelykh, Spin currents of exciton polaritons in microcavities with (110)-oriented quantum wells, Physical Review B **92**, 155305 (2015).

Bibliography

[1] Z. I. Alferov, "The history and future of semiconductor heterostructures", Semiconductors **32**, 3 (1998).

[2] T. F. Gallagher, *Rydberg Atoms* (Cambridge University Press, New York, 1994).

[3] T. Kazimierczuk, D. Fröhlich, S. Scheel, H. Stolz and M. Bayer, "Giant Rydberg excitons in the copper oxide Cu_2O", Nature (London) **514**, 343 (2014).

[4] J. Thewes, J. Heckötter, T. Kazimierczuk, M. Aßmann, D. Fröhlich, M. Bayer, M. A. Semina, and M. M. Glazov, "Observation of High Angular Momentum Excitons in Cuprous Oxide", Phys. Rev. Lett. **115**, 027402 (2015).

[5] S. Zielinska-Raczynska, G. Czajkowski, and D. Ziemkiewicz, "Optical properties of Rydberg excitons and polaritons", Phys. Rev. B **93**, 075206 (2016).

[6] J. Heckötter, M. Freitag, D. Fröhlich, M. Aßmann, M. Bayer, M. Semina, M. Glazov, "High-resolution study of the yellow excitons in Cu_2O subject to an electric field", Phys. Rev. B **95**, 035210 (2017).

[7] J. Heckötter, M. Freitag, D. Fröhlich, M. Aßmann, M. Bayer, M. Semina, M. Glazov, "Scaling laws of Rydberg excitons", arXiv:1704.00974 (2017).

[8] D. G. W. Parfitt and M. E. Portnoi, "The two-dimensional hydrogen atom revisited", J. Math. Phys. **43**, 4681 (2002).

[9] J. Inoue, T. Brandes, and A. Shimizu, "Renormalized bosonic interaction of excitons", Phys. Rev. B **61**, 2863 (2000).

[10] S. B. de-Leon and B. Laikhtman, "Exciton-exciton interactions in quantum wells: Optical properties and energy and spin relaxation", Phys. Rev. B **63**, 125306 (2001).

[11] S. Okumura and T. Ogawa, "Boson representation of two-exciton correlations: An exact treatment of composite-particle effects", Phys. Rev. B **65**, 035105 (2001).

[12] M. Combescot, O. Betbeder-Matibet, and R. Combescot, "Exciton-exciton scattering: Composite boson versus elementary boson" Phys. Rev. B **75**, 174305 (2007).

[13] M. M. Glazov, H. Ouerdane, L. Pilozzi, G. Malpuech, A. V. Kavokin, and A. d'Andrea, "Polariton-polariton scattering in microcavities: A microscopic theory", Phys. Rev. B **80**, 155306 (2009).

[14] C. Ciuti, V. Savona, C. Piermarocchi, A. Quattropani, and P. Schwendimann, "Role of the exchange of carriers in elastic exciton-exciton scattering in quantum wells", Phys. Rev. B **58**, 7926 (1998).

[15] F. Tassone and Y. Yamamoto, "Exciton-exciton scattering dynamics in a semiconductor microcavity and stimulated scattering into polaritons", Phys. Rev. B **59**, 10830 (1999).

[16] J. Zhang, Y. Ning, X. Zhang, J. Zhang, Y. Zeng, X. Shan, L. Qin, and L. Wang, "High-peak-power vertical-cavity surface-emitting laser quasi-array realized using optimized large-aperture single emitters", Japanese Journal of Applied Physics **53**, 070303 (2014).

[17] S. I. Pekar, "Theory of electromagnetic waves in a crystal in which excitons arise", Exp. Teor. Fiz. USSR **33**, 1022 (1957).

[18] V. M. Agranovich, "On the influence of reabsorption on the decay of fluorescence in molecular crystals", Optika i Spectr. textbf3, 84 (1957).

[19] J. J. Hopfield, "Theory of the Contribution of Excitons to the Complex Dielectric Constant of Crystals", Physical Review **112**, 1556 (1958).

[20] C. Weisbuch, M. Nishioka, A. Ishikawa, and Y. Arakawa, "Observation of the coupled exciton-photon mode splitting in a semiconductor quantum microcavity", Phys. Rev. Lett. **69**, 3314 (1992).

[21] H. Deng, H. Haug, and Y. Yamamoto, "Exciton-polariton Bose-Einstein condensation", Rev. Mod. Phys. 82, 1489 (2010).

[22] A. V. Kavokin, J. J. Baumberg, G. Malpuech, and F. P. Laussy, *Microcavities* (Oxford University Press, New York, 2007).

[23] T. C. H. Liew, I. A. Shelykh, and G. Malpuech, "Polaritonic devices", Physica E **43**, 1543 (2011).

[24] J. Kasprzak, M. Richard, S. Kundermann, A. Baas, P. Jeambrun, J. M. J. Keeling, F. M. Marchetti, M. H. Szymanska, R. Andre, J. L. Staehli, V. Savona,

P. B. Littlewood, B. Deveaud, and Le Si Dang, "Bose–Einstein condensation of exciton polaritons", Nature (London) **443**, 409 (2006).

[25] R. Balili, V. Hartwell, D. Snoke, L. Pfeiffer, and K. West, "Bose-Einstein Condensation of Microcavity Polaritons in a Trap", Science **316**, 1007 (2007).

[26] A. Amo, J. Lefrére, S. Pigeon, C. Adrados, C. Ciuti, I. Carusotto, R. Houdré, E. Giacobino, and A. Bramati, "Superfluidity of polaritons in semiconductor microcavities", Nature Phys. **5**, 805 (2009).

[27] A. Amo, D. Sanvitto, F. P. Laussy, D. Ballarini, E. del Valle, M. D. Martin, A. Lemaître, J. Bloch, D. N. Krizhanovskii, M. S. Skolnick, C. Tejedor, and L. Viña, "Collective fluid dynamics of a polariton condensate in a semiconductor microcavity", Nature **457**, 291-295 (2009).

[28] Q. Duan, D. Xu, W. Liu, J. Lu, L. Zhang, J. Wang, Y. Wang, J. Gu, T. Hu, W. Xie, X. Shen, and Z. Chen, "Polariton lasing of quasi-whispering gallery modes in a ZnO microwire", Appl. Phys. Lett. **103**, 022103 (2013).

[29] F. Li, L. Orosz, O. Kamoun, S. Bouchoule, C. Brimont, P. Disseix, T. Guillet, X. Lafosse, M. Leroux, J. Leymarie, M. Mexis, M. Mihailovic, G. Patriarche, F. Reveret, D. Solnyshkov, J. Zuniga-Perez, and G. Malpuech, "From Excitonic to Photonic Polariton Condensate in a ZnO-Based Microcavity", Phys. Rev. Lett. **110**, 196406 (2013).

[30] W. Xie, H. Dong, S. Zhang, L. Sun, W. Zhou, Y. Ling, J. Lu, X. Shen, and Z. Chen, "Room-Temperature Polariton Parametric Scattering Driven by a One-Dimensional Polariton Condensate", Phys. Rev. Lett. **108**, 166401 (2012).

[31] A. Kavokin, G. Malpuech, M. Glazov, "Optical Spin Hall Effect", Phys. Rev. Lett. **95**, 136601 (2005).

[32] H. Flayac, D.D. Solnyshkov, I.A. Shelykh, and G. Malpuech, "Transmutation of skyrmions to half-solitons driven by the nonlinear optical spin hall effect", Phys. Rev. Lett. **110**, 016404 (2013).

[33] S. Morina, T. C. H. Liew, and I. A. Shelykh, "Magnetic field control of the optical spin Hall effect", Phys. Rev. B **88**, 035311 (2013).

[34] Yu. E. Lozovik and V. I. Yudson, "On the possibility of superfluidity of spatially separated electrons and holes due to their coupling: new mechanism of superfluidity", JETP Lett. **22**, 26 (1975).

[35] Yu. E. Lozovik and V. I. Yudson, "New mechanism of superconductivity: coupling between spatially separated electrons and holes", Sov. Phys. JETP **44**, 389

(1976).

[36] L. V. Butov, "Cold exciton gases in coupled quantum well structures", J. Phys.: Condens. Matter, **19**, 295202, 2007.

[37] A. A. High, J. R. Leonard, A. T. Hammack, M. M. Fogler, L. V. Butov, A. V. Kavokin, K. L. Campman, and A. C. Gossard, "Spontaneous Coherence in a Cold Exciton Gas", Nature (London) **483**, 584 (2012).

[38] D. Snoke, S. Denev, Y. Liu, L. Pfeiffer, and K. West, "Long-range transport in excitonic dark states in coupled quantum wells", Nature **418**, 754 (2002).

[39] L. V. Butov, A. C. Gossard, and D. S. Chemla, "Macroscopically ordered state in an exciton system", Nature **418**, 751 (2002).

[40] O. Kyriienko, E. B. Magnusson, and I. A. Shelykh, "Spin dynamics of cold exciton condensates", Phys. Rev. B **86**, 115324 (2012).

[41] G. Christmann, A. Askitopoulos, G. Deligeorgis, Z. Hatzopoulos, S. I. Tsintzos, P. G. Savvidis, and J. J. Baumberg, "Oriented polaritons in strongly-coupled asymmetric double quantum well microcavities", Appl. Phys. Lett. **98**, 081111 (2011).

[42] P. Cristofolini, G. Christmann, S. I. Tsintzos, G. Deligeorgis, G. Konstantinidis, Z. Hatzopoulos, P. G. Savvidis, and J. J. Baumberg, "Coupling quantum tunneling with cavity photons", Science **336**, 704 (2012).

[43] O. Kyriienko, A. V. Kavokin, and I. A. Shelykh, "Superradiant Terahertz Emission by Dipolaritons", Phys. Rev. Lett. **111**, 176401 (2013).

[44] K. Kristinsson, O. Kyriienko, T. C. H. Liew, and I. A. Shelykh, "Continuous terahertz emission from dipolaritons", Phys. Rev. B **88**, 245303 (2013).

[45] K. Kristinsson, O. Kyriienko, and I. A. Shelykh, "Terahertz laser based on dipolaritons", Phys. Rev. A **89**, 023836 (2014).

[46] C. Cohen-Tannoudji, J. Dupont-Roc, and G. Grynberg, *Atom-Photon Interactions: Basic Processes and Applications* (Wiley, Chichester, 1998).

[47] D. A. Steck, "Quantum and Atom Optics", available online at http://steck.us/teaching

[48] M. O. Scully, M. S. Zubairy, *Quantum Optics* (Cambridge University Press, Cambridge, 2001).

[49] S. H. Autler, and C. H. Townes, "Stark Effect in Rapidly Varying Fields", Phys. Rev. **100**, 703 (1955).

[50] Q. T. Vu, H. Haug, O. D. Mücke, T. Tritschler, M. Wegener, G. Khitrova, and H. M. Gibbs, "Light-Induced Gaps in Semiconductor Band-to-Band Transitions", Phys. Rev. Lett. **92**, 217403 (2004).

[51] Q. T. Vu, and H. Haug, "Detection of light-induced band gaps by ultrafast femtosecond pump and probe spectroscopy", Phys. Rev. B **71**, 035305 (2005).

[52] F. J. López-Rodríguez, and G. G. Naumis, "Analytic solution for electrons and holes in graphene under electromagnetic waves: Gap appearance and nonlinear effects", Phys. Rev. B **78**, 201406(R) (2008).

[53] O. V. Kibis, "Metal-insulator transition in graphene induced by circularly polarized photons", Phys. Rev. B **81**, 165433 (2010).

[54] O. V. Kibis, O. Kyriienko, and I. A. Shelykh, "Band gap in graphene induced by vacuum fluctuations", Phys. Rev. B **8**4, 195413 (2011).

[55] M. M. Glazov, and S. D. Ganichev, "High frequency electric field induced nonlinear effects in graphene", Phys. Rep. **535**, 101 (2014).

[56] G. Usaj, P. M. Perez-Piskunow, L. E. F. Foa Torres, and C. A. Balseiro, "Irradiated graphene as a tunable Floquet topological insulator", Phys. Rev. B **90**, 115423 (2014).

[57] A. Myzyrowicz, D. Hulin, A. Antonetti, A. Migus, W. T. Masselink, and H. Morkoç, "Dressed Excitons in a Multiple-Quantum-Well Structure: Evidence for an Optical Stark Effect with Femtosecond Response Time", Phys. Rev. Lett. **56**, 2748 (1986).

[58] M. Wagner, H. Schneider, D. Stehr, S. Winnerl, A. M. Andrews, S. Schartner, G. Strasser, and M. Helm, "Observation of the Intraexciton Autler-Townes Effect in GaAs/ AlGaAs Semiconductor Quantum Wells", Phys. Rev. Lett. **105**, 167401 (2010).

[59] O. V. Kibis, "Persistent current induced by quantum light", Phys. Rev. B **86**, 155108 (2012).

[60] M. Teich, M. Wagner, H. Schneider, and M. Helm, "Semiconductor quantum well excitons in strong, narrowband terahertz fields", New J. Phys. **15**, 065007 (2013).

[61] N. Shammah, C.C. Phillips, and S. De Liberato, "Terahertz emission from

ac Stark-split asymmetric intersubband transitions", Phys. Rev. B **89**, 235309 (2014).

[62] F. Barachati, S. De Liberato, and S. Kena-Cohen, "Generation of Rabi-frequency radiation using exciton-polaritons", Phys. Rev. A **92**, 033828 (2015).

[63] O. V. Kibis, "Dissipationless Electron Transport in Photon-Dressed Nanostructures", Phys. Rev. Lett. **107**, 106802 (2011).

[64] O. V. Kibis, O. Kyriienko, and I. A. Shelykh, "Persistent current induced by vacuum fluctuations in a quantum ring", Phys. Rev. B **87**, 245437 (2013).

[65] F. K. Joibari, Y. M. Blanter, and G. E. W. Bauer, "Light-induced spin polarizations in quantum rings", Phys. Rev. B **90**, 155301 (2014).

[66] G. Yu. Kryuchkyan, O. Kyriienko, and I. A. Shelykh, "Lamb shift of energy levels in quantum rings"J. Phys. B **48**, 025401 (2015).

[67] J. P. Reithmaier, G. Sek, A. Löffler, C. Hofmann, S. Kuhn, S. Reitzenstein, L. V. Keldysh, V. D. Kulakovskii, T. L. Reinecker, and A. Forchel, "Strong coupling in a single quantum dot–semiconductor microcavity system", Nature **432**, 197 (2004).

[68] T. Yoshie, A. Scherer, J. Heindrickson, G. Khitrova, H. M. Gibbs, G. Rupper, C. Ell, O. B. Shchekin, and D. G. Deppe, "Vacuum Rabi splitting with a single quantum dot in a photonic crystal nanocavity" Nature **432**, 200 (2004).

[69] E. Peter, P. Senellart, D. Martrou, A. Lemaitre, J. Hours, J. M. Gérard, and J. Bloch, "Exciton-Photon Strong-Coupling Regime for a Single Quantum Dot Embedded in a Microcavity", Phys. Rev. Lett. **95**, 067401 (2005).

[70] A. Muller, E. B. Flagg, P. Bianucci, X. Y. Wang, D. G. Deppe, W. Ma, J. Zhang, G. J. Salamo, M. Xiao, and C. K. Shih, "Resonance Fluorescence from a Coherently Driven Semiconductor Quantum Dot in a Cavity", Phys. Rev. Lett. **99**, 187402 (2007).

[71] S. M. Ulrich, S. Ates, S. Reitzenstein, A. Loffler, A. Forchel and P. Michler,"Dephasing of Triplet-Sideband Optical Emission of a Resonantly Driven InAs/GaAs Quantum Dot inside a Microcavity", Phys. Rev. Lett. **106**, 247402 (2011).

[72] A. Majumdar, M. Bajcsy, and J. Vuckovic, "Probing the ladder of dressed states and nonclassical light generation in quantum-dot–cavity QED", Phys. Rev. A **85**, 041801(R) (2012).

[73] Y. He, Y.-M. He, J. Liu, Y.-J. Wei, H. Y. Ramirez, M. Atature, C. Schneider, M. Kamp, S. Hofling, C.-Y. Lu, and J.-W. Pan, "Dynamically Controlled Resonance Fluorescence Spectra from a Doubly Dressed Single InGaAs Quantum Dot", Phys. Rev. Lett. **114**, 097402 (2015).

[74] O. V. Kibis, G. Ya. Slepyan, S. A. Maksimenko, and A. Hoffmann, "Matter Coupling to Strong Electromagnetic Fields in Two-Level Quantum Systems with Broken Inversion Symmetry", Phys. Rev. Lett. **102**, 023601 (2009).

[75] I. G. Savenko, O. V. Kibis, and I. A. Shelykh, "Asymmetric quantum dot in a microcavity as a nonlinear optical element", Phys. Rev. A, **85**, 053818 (2012).

[76] F. Oster, C. H. Keitel, and M. Macovei, "Generation of correlated photon pairs in different frequency ranges", Phys. Rev. A **8**5, 063814 (2012).

[77] E. Paspalakis, J. Boviatsis, S. Baskoutas, "Effects of probe field intensity in nonlinear optical processes in asymmetric semiconductor quantum dots", J. App. Phys. **1**14, 153107 (2013).

[78] Y. Masumoto, T. Takagahara *Semiconductor Quantum Dots* (Springer, Berlin, 2002).

[79] A. Tartakovskii, *Quatum Dots* (Cambridge University Press, Cambridge, 2012).

[80] F. Widmann, J. Simon, B. Daudin, G. Feuillet, J. L. Rouvière, N. T. Pelekanos, and G. Fishman, "Blue-light emission from GaN self-assembled quantum dots due to giant piezoelectric effect", Phys. Rev. B **58**, R15989 (1998).

[81] O. Moriwaki, T. Someya, K. Tachibana, S. Ishida, and Y. Arakawa, "Blue-light emission from GaN self-assembled quantum dots due to giant piezoelectric effect", Appl. Phys. Lett. **76**, 2361 (2000).

[82] D. P. Williams, A. D. Andreev, E. P. O'Reilly, and D. A. Faux, "Derivation of built-in polarization potentials in nitride-based semiconductor quantum dots", Phys. Rev. B **72**, 235318 (2005).

[83] T. Bretagnon, P. Lefebvre, P. Valvin, R. Bardoux, T. Guillet, T. Taliercio, B. Gil, N. Grandjean, F. Semond, B. Damilano, A. Dussaigne, and J. Massies, "Radiative lifetime of a single electron-hole pair in GaN/AlN quantum dots", Phys. Rev. B **73**, 113304 (2006).

[84] R. J. Warburton, C. Schulhauser, D. Haft, C. Schauflein, K. Karrai, J. M. Garcia, W. Schoenfeld, and P. M. Petroff, "Giant permanent dipole moments of excitons in semiconductor nanostructures", Phys. Rev. B **65**, 113303 (2002).

[85] I. Ostapenko, G. Honig, C. Kindel, S. Rodt, A. Strittmatter, A. Hoffmann, and D. Bimberg, "Large internal dipole moment in InGaN/GaN quantum dots", Appl. Phys. Lett. **97**, 063103 (2010).

[86] G. Honig, S. Rodt, G. Callsen, I. A. Ostapenko, T. Kure, A. Schliwa, C. Kindel, D. Bimberg, A. Hoffmann, S. Kako and Y. Arakawa, "Identification of electric dipole moments of excitonic complexes in nitride-based quantum dots", Phys. Rev. B **88**, 045309 (2013).

[87] Z. Ficek, and H. S. Freedhoff, "Fluorescence and absorption by a two-level atom in a bichromatic field with one strong and one weak component", Phys. Rev. A **53**, 4275 (1996).

[88] M. Jakob and G. Yu. Kryuchkyan, "Squeezing in the resonance fluorescence of a bichromatically driven two-level atom", Phys. Rev. A **58**, 767 (1998).

[89] G. Yu. Kryuchkyan, M. Jakob, and A. S. Sargsian, "Resonance fluorescence in a bichromatic field as a source of nonclassical light" Phys. Rev. A **57**, 2091 (1998).

[90] M. Jakob and G. Yu. Kryuchkyan, "Autler-Townes effect with mono- and bichromatic pump fields: Reservoir effects and Floquet-state treatment", Phys. Rev. A **57**, 1355 (1998).

[91] Z. Ficek, and T. Rudolph, "Quantum interference in a driven two-level atom", Phys. Rev. A **60**, R4245 (1999).

[92] G. A. Abovyan and G. Yu. Kryuchkyan, "Quasienergies and dynamics of a superconducting qubit in a time-modulated field" Phys. Rev. A **88**, 033811 (2013).

[93] H. Y. Ramirez, "Double dressing and manipulation of the photonic density of states in nanostructured qubits", RSC Adv. **3**, 24991 (2013).

[94] S. N. Shevchenko, G. Oelsner, Ya. S. Greenberg, P. Macha, D. S. Karpov, M. Grajcar, U. Hübner, A. N. Omelyanchouk, and E. Ilichev, "Amplification and attenuation of a probe signal by doubly dressed states", Phys. Rev. B **8**9, 184504 (2014).

[95] H. S. Freedhoff, and M. E. Smithers, "Radiative transitions at the doublet splitting frequency in the resonant Stark effect", J. Phys. B **8**, L209 (1975).

[96] A. S. M. Windsor, C. Wei, S. A. Holmstrom, J. P. D. Martin, and N. B. Manson, "Experimental Studies of a Strongly Driven Rabi Transition", Phys. Rev. Lett. **8**0, 3045 (1998).

[97] M. Macovei, M. Mishra, and C. H. Keitel, "Population inversion in two-level

systems possessing permanent dipoles", Phys. Rev. A **9**2, 013846 (2015).

[98] L. D. Landau, and E. M. Lifshitz, *Quantum Mechanics* (Pergamon Press, Oxford 1965).

[99] C. Cohen-Tannoudji, and S. Reynaud, "Dressed-atom description of resonance fluorescence and absorption spectra of a multi-level atom in an intense laser beam", J. Phys. B **10**, 345 (1977).

[100] G. Yu. Kryuchkyan, "Radiative corrections to the atomic levels in a strong electromagnetic field", JETP **56**, 1153 (1982).

[101] O. Kocharovskaya, S.-Y. Zhu, M. O. Scully, P. Mandel, and Y. V. Radeonychev, "Generalization of the Maxwell-Bloch equations to the case of strong atom-field coupling", Phys. Rev. A **49**, 4928 (1994).

[102] G. Yu. Kryuchkyan, "Squeezed-vacuum effects in the quasienergy structure of atoms in a laser field ", JETP **82**, 60 (1996).

[103] S. Morina, O. V. Kibis, A. A. Pervishko, and I. A. Shelykh, "Transport properties of a two-dimensional electron gas dressed by light", Phys. Rev. B **91**, 155312 (2015).

[104] K. Dini, O. V. Kibis, and I. A. Shelykh, "Magnetic properties of a two-dimensional electron gas strongly coupled to light", Phys. Rev. B **93**, 235411 (2016).

[105] O. V. Kibis, S. Morina, K. Dini, and I. A. Shelykh, "Magnetoelectronic properties of graphene dressed by a high-frequency field", Phys. Rev. B **93**, 115420 (2016).

[106] K. Kristinsson, O. V. Kibis, S. Morina, and I. A. Shelykh, "Control of electronic transport in graphene by electromagnetic dressing", Sci. Rep. **6**, 20082 (2016).

[107] M. Tonouchi, "Cutting-edge terahertz technology", Nature Photonics **1**, 97 (2007).

[108] K. Kim, A. Taylor, J. Glownia, and G. Rodriguez, "Coherent control of terahertz supercontinuum generation in ultrafast laser–gas interactions", Nature Photonics **2**, 605 - 609 (2008).

[109] H.-C. Wu, J. Meyer-ter-Vehn, and Z.-M. Sheng, "Phase-sensitive terahertz emission from gas targets irradiated by few-cycle laser pulses", New Journal of Physics **10**, 043001 (2008).

[110] A. Davoyan, M. Morozov, V. Popov, A. Satou, and T. Otsuji, "Graphene surface emitting terahertz laser: Diffusion pumping concept", Appl. Phys. Lett. **103**, 251102 (2013).

[111] V. Ryzhii, A. Dubinov, V. Aleshkin, M. Ryzhii, and T. Otsuji, "Injection terahertz laser using the resonant inter-layer radiative transitions in double-graphene-layer structure", Appl. Phys. Lett. **103**, 163507 (2013).

[112] Z. Diao, C. Bonzon, G. Scalari, M. Beck, J. Faist, and R. Houdre, "Continuous-wave vertically emitting photonic crystal terahertz laser", Laser & Photonics Reviews **7**, L45 (2013).

[113] R. Kohler, A. Tredicucci, F. Beltram, H. Beere, E. Linfield, A. Davies, D. Ritchie, R. Iotti and F. Rossi, "Terahertz semiconductor-heterostructure laser.", Nature **417**, 156-159 (2002).

[114] B. Williams, "Terahertz quantum-cascade lasers", Nature Photonics **1**, 517 - 525 (2007).

[115] N. A. Yampolsky and G. M. Fraiman, "Conversion of laser radiation to terahertz frequency waves in plasma", Physics of Plasmas **13**, 113108 (2006).

[116] A. Kavokin, T. C. H. Liew, C. Schneider and S. Hofling, "Bosonic lasers: The state of the art", Low Temp. Phys. **42**, 323 (2016).

[117] S. Christopoulos, G. Baldassarri Hoger von Hogersthal, A. J. D. Grundy, P. G. Lagoudakis, A. V. Kavokin, J. J. Baumberg, G. Christmann, R. Butte, E. Feltin, J.-F. Carlin, and N. Grandjean, "Room-Temperature Polariton Lasing in Semiconductor Microcavities", Phys. Rev. Lett. **98**, 126405 (2007).

[118] K. S. Daskalakis, P. S. Eldridge, G. Christmann, E. Trichas, R. Murray, E. Iliopoulos, E. Monroy, N. T. Pelekanos, J. J. Baumberg, and P. G. Savvidis, "All-dielectric GaN microcavity: Strong coupling and lasing at room temperature", Appl. Phys. Lett. **102**, 101113 (2013).

[119] B. Zhang, Z. Wang, S. Brodbeck, C. Schneider, M. Kamp, S. Hofling, and H. Deng, "Zero-dimensional polariton laser in a subwavelength grating-based vertical microcavity", Light: Sci. App. **3**, e135 (2014).

[120] D. Bajoni, P. Senellart, E. Wertz, I. Sagnes, A. Miard, A. Lemaitre, and J. Bloch, "Polariton Laser Using Single Micropillar GaAs-GaAlAs Semiconductor Cavities", Phys. Rev. Lett. **100**, 047401 (2008).

[121] S. Azzini, D. Gerace, M. Galli, I. Sagnes, R. Braive, A. Lemaitre, J. Bloch, and D. Bajoni, "Ultra-low threshold polariton lasing in photonic crystal cavities",

Appl. Phys. Lett. **99**, 111106 (2011).

[122] S. De Liberato, C. Ciuti, and C. C. Phillips, "Terahertz lasing from intersubband polariton-polariton scattering in asymmetric quantum wells", Phys. Rev. B **87**, 241304(R) (2013).

[123] T. C. H. Liew, M. M. Glazov, K. V. Kavokin, I. A. Shelykh, M. A. Kaliteevski, and A. V. Kavokin, "Proposal for a Bosonic Cascade Laser", Phys. Rev. Lett. **110**, 047402 (2013).

[124] S. Huppert, O. Lafont, E. Baudin, J. Tignon, and R. Ferreira, "Terahertz emission from multiple-microcavity exciton-polariton lasers", Phys. Rev. B **90**, 241302(R) (2014).

[125] K. V. Kavokin, M. A. Kaliteevski, R. A. Abram, A. V. Kavokin, S. Sharkova, and I. A. Shelykh, "Stimulated emission of terahertz radiation by exciton-polariton lasers", Appl. Phys. Lett. **97**, 201111 (2010).

[126] A. V. Kavokin, I. A. Shelykh, T. Taylor, and M. M. Glazov, "Vertical Cavity Surface Emitting Terahertz Laser", Phys. Rev. Lett. **108**, 197401 (2012).

[127] I. G. Savenko, I. A. Shelykh, and M. A. Kaliteevski, "Nonlinear Terahertz Emission in Semiconductor Microcavities", Phys. Rev. Lett. **107**, 027401 (2011).

[128] G. Khitrova, J. F. Valley, and H. M. Gibbs, "Gain-feedback approach to optical instabilities in sodium vapor", Phys. Rev. Lett. **60**, 1126 (1988).

[129] Y. Zhu, A. Lezama, and T. W. Mossberg, "Effect of optical gain on the fluorescence of two-level atoms into the modes of an optical cavity", Phys. Rev. A **39**, 2268 (1989).

[130] J. Zakrzewski, M. Lewenstein, and T.W. Mossberg, "Theory of dressed-state lasers. I. Effective Hamiltonians and stability properties", Phys. Rev. A **44**, 7717 (1991).

[131] I. Chestnov, A. Alodjants, and S. Arakelian, "Lasing and high-temperature phase transitions in atomic systems with dressed-state polaritons", Phys. Rev. A **88**, 063834 (2013).

[132] J. Hauss, A. Fedorov, S. Andre, V. Brosco, C. Hutter, R. Kothari, S. Yeshwanth, A. Shnirman and G. Schön, "Dissipation in circuit quantum electrodynamics: lasing and cooling of a low-frequency oscillator", New Journal of Physics, **10(9)**, 095018 (2008).

[133] O. Astafiev, A.M. Zagoskin, A.A. Abdumalikov Jr., Yu. A. Pashkin, T. Ya-

mamoto, K. Inomata, Y. Nakamura, J. S. Tsai, "Resonance Fluorescence of a Single Artificial Atom", Science **327**, 840 (2010).

[134] A. N. Omelyanchouk, S. N. Shevchenko, Ya. S. Greenberg, O. Astafiev, and E. Il'ichev, "Quantum behavior of a flux qubit coupled to a resonator", Low Temp. Phys. **36**, 893 (2010).

[135] Ya. S. Greenberg, "Low-frequency Rabi spectroscopy of dissipative two-level systems: Dressed-state approach", Phys. Rev. B **76**, 104520 (2007).

[136] G. Oelsner, P. Macha, O. V. Astafiev, E. Il'ichev, M. Grajcar, U. Hübner, B. I. Ivanov, P. Neilinger, and H.-G. Meyer, "Dressed-State Amplification by a Single Superconducting Qubit", Phys. Rev. Lett. **110**, 053602 (2013).

[137] P. Neilinger, M. Rehak, M. Grajcar, G. Oelsner, U. Hubner, and E. Il'ichev, "Two-photon lasing by a superconducting qubit", Phys. Rev. B 91, 104516 (2015).

[138] P. Borri, W. Langbein, S. Schneider, U. Woggon, R. L. Sellin, D. Ouyang, and D. Bimberg, "Ultralong Dephasing Time in InGaAs Quantum Dots", Phys. Rev. Lett. **87**, 157401 (2001).

[139] T. Chen, P. Liu, J. Liu, Z. Hong, "A terahertz photonic crystal cavity with high Q-factors", Appl. Phys. B **115**, 105-109 (2014).

[140] Y. Todorov, I. Sagnes, I. Abram, and C. Minot, "Purcell Enhancement of Spontaneous Emission from Quantum Cascades inside Mirror-Grating Metal Cavities at THz Frequencies", Phys. Rev. Lett. **99**, 223603 (2007).

[141] C. Feuillet-Palma, Y. Todorov, R. Steed, A. Vasanelli, G. Biasiol, L. Sorba, and C. Sirtori, "Extremely sub-wavelength THz metal-dielectric wire microcavities", Opt Express. **20**, 29121 (2012).

[142] S. Das, and M. Macovei, "Collective quantum dot inversion and amplification of photon and phonon waves", Phys. Rev. B **88**, 125306 (2013).

[143] J. H. Quilter, A. J. Brash, F. Liu, M. Glässl, A. M. Barth, V. M. Axt, A. J. Ramsay, M. S. Skolnick, and A. M. Fox, "Phonon-Assisted Population Inversion of a Single InGaAs/GaAs Quantum Dot by Pulsed Laser Excitation", Phys. Rev. Lett. **114**, 137401 (2015).

[144] S. Kako, M. Miyamura, K. Tachibana, K. Hoshino, and Y. Arakawa, "Size-dependent radiative decay time of excitons in GaN/AlN self-assembled quantum dots", Appl. Phys. Letts. **83**, 984 (2003).

[145] M. Nomura, S. Iwamoto, K. Watanabe, N. Kumagai, Y. Nakata, S. Ishida, and Y. Arakawa, "Room temperature continuous-wave lasing in photonic crystal nanocavity", Optics Express **14**, 6308 (2006).

[146] A. Sakamoto, and M. Sugawara, "Theoretical calculation of lasing spectra of quantum-dot lasers: effect of homogeneous broadening of optical gain", IEEE Photonics Technology Letters **12**, 107 (2000).

[147] O. Svelto, *Principles of lasers* (Springer, New York, 1989).

[148] M. Scheibner, T. Schmidt, L. Worschech, A. Forchel, G. Bacher, T. Passow and D. Hommel, "Superradiance of quantum dots", Nature Physics **3**, 106 (2007).

[149] T. Yoshie, J. Vučković, A. Scherer, H. Chen and D. Deppe, "High quality two-dimensional photonic crystal slab cavities", Appl. Phys. Lett. **79**, 4289 (2001).

[150] K. Hoshino, S. Kako, and Y. Arakawa, "Formation and optical properties of stacked GaN self-assembled quantum dots grown by metalorganic chemical vapor deposition", Applied Physics Letters **85**, 1262 (2004).

[151] P. Rinke, M. Winkelnkemper, A. Qteish, D. Bimberg, J. Neugebauer, and M. Scheffler, "Consistent set of band parameters for the group-III nitrides AlN, GaN, and InN", Phys. Rev. B **77**, 075202 (2008).

[152] L. Pitaevskii and S. Stringari, *Bose-Einstein Condensation* (Oxford University Press, Oxford, 2003).

[153] M. H. Anderson, J. R. Ensher, M. R. Matthews, C. E. Wieman, and E. A. Cornell, "Observation of bose-einstein condensation in a dilute atomic vapor", Science **269**, 198 (1995).

[154] K. B. Davis, M.-O. Mewes, M. R. Andrews, N. J. van Druten, D. S. Durfee, D. M. Kurn, and W. Ketterle, "Bose-Einstein Condensation in a Gas of Sodium Atoms", Phys. Rev. Lett. **75**, 3969 (1995).

[155] L. V. Keldysh and Yu. V. Kopaev, "Possible instability of semimetallic state toward coulomb interaction", Sov. Phys. Solid State **6**, 2219 (1965); L. V. Keldysh and A. N. Kozlov, "Collective properties of excitons in semiconductors", Sov. Phys. JETP **27**, 521 (1968).

[156] J. M. Blatt, K. W. Böer, and W. Brandt, "Bose-Einstein Condensation of Excitons", Phys. Rev. **126**, 1691 (1962).

[157] S. A. Moskalenko and D. W. Snoke, *Bose-Einstein Condensation of Excitons and Biexcitons* (Cambridge University Press, Cambridge, U.K., 2000).

[158] E. Wertz, L. Ferrier, D. D. Solnyshkov, R. Johne, D. Sanvitto, A. Lemaître, I. Sagnes, R. Grousson, A. V. Kavokin, P. Senellart, G. Malpuech, and J. Bloch, "Spontaneous formation and optical manipulation of extended polariton condensates", Nature Phys. **6**, 860 (2010).

[159] J. Fischer, S. Brodbeck, A. V. Chernenko, I. Lederer, A. Rahimi-Iman, M. Amthor, V. D. Kulakovskii, L. Worschech, M. Kamp, M. Durnev, C. Schneider, A. V. Kavokin, and S. Höfling, "Anomalies of a Nonequilibrium Spinor Polariton Condensate in a Magnetic Field", Phys. Rev. Lett. **112**, 093902 (2014).

[160] J. J. Baumberg, A. V. Kavokin, S. Christopoulos, A. J. D. Grundy, R. Butté, G. Christmann, D. D. Solnyshkov, G. Malpuech, G. Baldassarri Höger von Hogersthal, E. Feltin, J.-F. Carlin, and N. Grandjean, "Spontaneous Polarization Buildup in a Room-Temperature Polariton Laser", Phys. Rev. Lett. **101**, 136409 (2008).

[161] J. D. Plumhof, T. Stöferle, L. Mai, U. Scherf, and R. F. Mahrt, "Room-temperature Bose–Einstein condensation of cavity exciton–polaritons in a polymer", Nature Mater. **13**, 247 (2014).

[162] C. Schneider, A. Rahimi-Iman, Na Young Kim, J. Fischer, I. G. Savenko, M. Amthor, M. Lermer, A. Wolf, L. Worschech, V. D. Kulakovskii, I. A. Shelykh, M. Kamp, S. Reitzenstein, A. Forchel, Y. Yamamoto, and S. Hofling, "An electrically pumped polariton laser, Nature (London) **497**, 348 (2013).

[163] P. Bhattacharya, B. Xiao, A. Das, S. Bhowmick, and J. Heo, "Solid State Electrically Injected Exciton-Polariton Laser", Phys. Rev. Lett. **110**, 206403 (2013).

[164] M. Sich, D. N. Krizhanovskii, M. S. Skolnick, A. V. Gorbach, R. Hartley, D. V. Skryabin, E. A. Cerda-Méndez, K. Biermann, R. Hey, and P. V. Santos, "Observation of bright polariton solitons in a semiconductor microcavity", Nature Photon. **6**, 50 (2012).

[165] M. Sich, F. Fras, J. K. Chana, M. S. Skolnick, D. N. Krizhanovskii, A. V. Gorbach, R. Hartley, D. V. Skryabin, S. S. Gavrilov, E. A. Cerda-Méndez, K. Biermann, R. Hey, and P. V. Santos, "Effects of Spin-Dependent Interactions on Polarization of Bright Polariton Solitons", Phys. Rev. Lett. **112**, 046403 (2014).

[166] A. Amo, S. Pigeon, D. Sanvitto, V. G. Sala, R. Hivet, I. Carusotto, F. Pisanello, G. Leménager, R. Houdré, E Giacobino, C. Ciuti, and A. Bramati, "Polariton Superfluids Reveal Quantum Hydrodynamic Solitons", Science **332**, 1167 (2011).

[167] K. G. Lagoudakis, M. Wouters, M. Richard, A. Baas, I. Carusotto, R. André, Le Si Dang, and B. Deveaud-Plédran, "Quantized vortices in an exciton–polariton condensate", Nature Phys. **4**, 706 (2008).

[168] F. Manni, K. G. Lagoudakis, T. C. H Liew, R. André, V. Savona, and B. Deveaud, "Dissociation dynamics of singly charged vortices into half-quantum vortex pairs", Nature Commun. **3**, 1309 (2012).

[169] C. Leyder, M. Romanelli, J. Ph. Karr, E. Giacobino, T. C. H. Liew, M. M. Glazov, A. V. Kavokin, G. Malpuech, and A. Bramati, "Observation of the optical spin Hall effect", Nature Phys. **3**, 628 (2007).

[170] G. Tosi, F. M. Marchetti, D. Sanvitto, C. Antón, M. H. Szymańska, A. Berceanu, C. Tejedor, L. Marrucci, A. Lemaître, J. Bloch, and L. Vina, "Onset and Dynamics of Vortex-Antivortex Pairs in Polariton Optical Parametric Oscillator Superfluids", Phys. Rev. Lett. **107**, 036401 (2011).

[171] C. Adrados, A. Amo, T. C. H. Liew, R. Hivet, R. Houdré, E. Giacobino, A. V. Kavokin, and A. Bramati, "Spin Rings in Bistable Planar Semiconductor Microcavities", Phys. Rev. Lett. **105**, 216403 (2010).

[172] I. A. Shelykh, A. V. Kavokin, Y. G. Rubo, T. C. H. Liew, and G. Malpuech, "Polariton polarization-sensitive phenomena in planar semiconductor microcavities", Semicond. Sci. Technol. **25**, 013001 (2010).

[173] T. Espinosa-Ortega and T. C. H. Liew, "Complete architecture of integrated photonic circuits based on and and not logic gates of exciton polaritons in semiconductor microcavities", Phys. Rev. B **87**, 195305 (2013).

[174] I. Carusotto and C. Ciuti, "Quantum fluids of light", Rev. Mod. Phys. **85**, 299 (2013).

[175] L. V. Butov, "Condensation and pattern formation in cold exciton gases in coupled quantum wells", J. Phys.: Condens. Matter **16**, R1577 (2004).

[176] L. V. Butov, "Cold exciton gases in coupled quantum well structures", J. Phys. Condens. Matter **19**, 295202 (2007).

[177] L. V. Butov, L. S. Levitov, A. V. Mintsev, B. D. Simons, A. C. Gossard, and D. S. Chemla, "Formation Mechanism and Low-Temperature Instability of Exciton Rings", Phys. Rev. Lett. **92**, 117404 (2004).

[178] R. Rapaport, Gang Chen, D. Snoke, Steven H. Simon, Loren Pfeiffer, Ken West, Y. Liu, and S. Denev, "Charge Separation of Dense Two-Dimensional Electron-Hole Gases: Mechanism for Exciton Ring Pattern Formation", Phys. Rev. Lett. **92**, 117405 (2004).

[179] M. Alloing, D. Fuster, Y. González, L. González, and F. Dubin, "Observation of macroscopic coherence in self-organized dipolar excitons", arXiv:1210.3176

(2012).

[180] A. A. High, A. T. Hammack, J. R. Leonard, Sen Yang, L. V. Butov, T. Ostatnický, M. Vladimirova, A. V. Kavokin, T. C. H. Liew, K. L. Campman, and A. C. Gossard, "Spin Currents in a Coherent Exciton Gas", Phys. Rev. Lett. **110**, 246403 (2013).

[181] J. R. Leonard, Y. Y. Kuznetsova, Sen Yang, L. V. Butov, T. Ostatnický, A. Kavokin, and A. C. Gossard, "Spin Transport of Excitons", Nano Lett. **9**, 4204 (2009).

[182] A. Violante, R. Hey, and P. V. Santos, "Coherent transport and manipulation of spins in indirect exciton nanostructures", Phys. Rev. B **91**, 125302 (2014).

[183] A. G. Winbow, J. R. Leonard, M. Remeika, Y. Y. Kuznetsova, A. A. High, A. T. Hammack, L. V. Butov, J. Wilkes, A. A. Guenther, A. L. Ivanov, M. Hanson, and A. C. Gossard, "Electrostatic Conveyer for Excitons", Phys. Rev. Lett. **106**, 196806 (2011).

[184] P. Andreakou, S. V. Poltavtsev, J. R. Leonard, E. V. Calman, M. Remeika, Y. Y. Kuznetsova, L. V. Butov, J. Wilkes, M. Hanson, and A. C. Gossard, "Optically Controlled Excitonic Transistor", Appl. Phys. Lett. **104**, 091101 (2014).

[185] S. Lazić, A. Violante, K. Cohen, R. Hey, R. Rapaport, and P. V. Santos, "Scalable interconnections for remote indirect exciton systems based on acoustic transport", Phys. Rev. B **89**, 085313 (2014).

[186] G. J. Schinner, J. Repp, K. Kowalik-Seidl, E. Schubert, M. P. Stallhofer, A. K. Rai, D. Reuter, A. D. Wieck, A. O. Govorov, A. W. Holleitner, and J. P. Kotthaus, "Quantum Hall signatures of dipolar Mahan excitons", Phys. Rev. B **87** 041303 (R) (2013).

[187] G. J. Schinner, J. Repp, E. Schubert, A. K. Rai, D. Reuter, A. D. Wieck, A. O. Govorov, A. W. Holleitner, and J. P. Kotthaus, "Many-body correlations of electrostatically trapped dipolar excitons", Phys. Rev. B **87**, 205302 (2013).

[188] Y. Shilo, K. Cohen, B. Laikhtman, K. West, L. Pfeiffer, R. Rapaport, "Particle correlations and evidence for dark state condensation in a cold dipolar exciton fluid", Nature Communications **4**, 2335 (2013)

[189] M. Stern, V. Umansky, I. Bar-Joseph, "Exciton Liquid in Coupled Quantum Wells", Science **343**, 55 (2014).

[190] K. Sivalertporn, L. Mouchliadis, A. L. Ivanov, R. Philp, and E. A. Muljarov, "Direct and indirect excitons in semiconductor coupled quantum wells in an

applied electric field", Phys. Rev. B **85**, 045207 (2012).

[191] L. V. Butov, A. L. Ivanov, A. Imamoglu, P. B. Littlewood, A. A. Shashkin, V. T. Dolgopolov, K. L. Campman, and A. C. Gossard, "Stimulated Scattering of Indirect Excitons in Coupled Quantum Wells: Signature of a Degenerate Bose-Gas of Excitons", Phys. Rev. Lett. **86**, 5608 (2001).

[192] A. V. Nalitov, M. Vladimirova, A. V. Kavokin, L. V. Butov, and N. A. Gippius, "Nonlinear optical probe of indirect excitons", Phys. Rev. B **89**, 155309 (2014).

[193] L.S. Levitov, B.D. Simons, and L.V. Butov, "Pattern Formation as a Signature of Quantum Degeneracy in a Cold Exciton System", Phys. Rev. Lett. **94**, 176404 (2005).

[194] G. Chen, R. Rapaport, L.N. Pffeifer, K. West, P.M. Platzman, S. Simon, Z. Voros, and D. Snoke, "Artificial Trapping of a Stable High-Density Dipolar Exciton Fluid", Phys. Rev. B **74**, 045309 (2006).

[195] R. Rapaport, and G. Chen, "Experimental methods and analysis of cold and dense dipolar exciton fluids", J. Phys.: Condens. Matter. **19**, 295207 (2007).

[196] G.J. Schinner, E. Schubert, M.P. Stallhofer, J.P. Kotthaus, D. Schuh, A.K. Rai, D. Reuter, A.D. Wieck, and A.O. Govorov, "Electrostatically trapping indirect excitons in coupled InxGa1-xAs quantum wells", Phys. Rev. B **83**, 165308 (2011).

[197] A.A. High, J.R. Leonard, M. Remeika, L.V. Butov, M. Hanson, and A.C. Gossard, "Condensation of Excitons in a Trap", Nano Lett. **12 (5)**, 2605-2609 (2012).

[198] G.J. Schinner, J. Repp, E. Schubert, A.K. Rai, D. Reuter, A.D. Wieck, A.O. Govorov, A.W. Holleitner, and J.P. Kotthaus, "Confinement and Interaction of Single Indirect Excitons in a Voltage-Controlled Trap Formed Inside Double InGaAs Quantum Wells", Phys. Rev. Lett. **110**, 127403 (2013).

[199] M. Alloing, A. Lemaitre, E. Galopin, and F. Dubin, "Optically programmable excitonic traps", Scientific reports **3** (2013).

[200] O. Kyriienko, I. A. Shelykh, and T. C. H. Liew, "Tunable single-photon emission from dipolaritons", Phys. Rev. A **90**, 033807 (2014).

[201] O. Kyriienko and T. C. H. Liew, "Triggered single-photon emitters based on stimulated parametric scattering in weakly nonlinear systems", Phys. Rev. A **90**, 063805 (2014).

[202] N. A. Sinitsyn, "Landau-Zener transitions in chains", Phys. Rev. A **87**, 032701 (2013).

[203] T. C. H. Liew and I. A. Shelykh, "Non-adiabatic population transfer in coupled bosonic systems", J. Phys. B: At. Mol. Opt. Phys. **45**, 245003 (2012).

[204] M. Wouters and I. Carusotto, "Excitations in a Nonequilibrium Bose-Einstein Condensate of Exciton Polaritons", Phys. Rev. Lett. **99**, 140402 (2007).

[205] F. Tassone, C. Piermarocchi, V. Savona, A. Quattropani, and P. Schwendimann, "Photoluminescence decay times in strong-coupling semiconductor microcavities", Phys. Rev. B **53**, R7642 (1996).

[206] A.G. Winbow, L.V. Butov, and A C. Gossard, "Photon storage with subnanosecond readout rise time in coupled quantum wells", J. Appl. Phys. **104**, 063515 (2008).

[207] O. Kyriienko, E. Ostrovskaya, O. A. Egorov, I. A. Shelykh, and T. C. H. Liew, "Bistability in microcavities with incoherent optical or electrical excitation", Phys. Rev. B **90**, 125407 (2014).

[208] I. Bloch, J. Dalibard, and W. Zwerger, "Many-body physics with ultracold gases", Rev. Mod. Phys **80**, 885 (2008).

[209] C. Chin, R. Grimm, P. Julienne, and E. Tiesinga, "Feshbach resonances in ultracold gases", Rev. Mod. Phys. **82**, 1225 (2010).

[210] M. D. Lukin, M. Fleischhauer, R. Cote, L. M. Duan, D. Jaksch, J. I. Cirac, and P. Zoller, "Dipole Blockade and Quantum Information Processing in Mesoscopic Atomic Ensembles", Phys. Rev. Lett. **87**, 037901 (2001).

[211] A. Gaëtan, Y. Miroshnychenko, T. Wilk, A. Chotia, M. Viteau, D. Comparat, P. Pillet, A. Browaeys, and Ph. Grangier, "Observation of collective excitation of two individual atoms in the Rydberg blockade regime", Nature Physics **5**, 115 (2009).

[212] E. Urban, T. A. Johnson, T. Henage, L. Isenhower, D. D. Yavuz, T. G. Walker, and M. Saffman, "Observation of Rydberg blockade between two atoms", Nature Phys. **5**, 110 (2009).

[213] M. Saffman, T. G. Walker, and K. Mølmer, "Quantum information with Rydberg atoms", Rev. Mod. Phys. **82**, 2313 (2010).

[214] T. Peyronel, O. Firstenberg, Qi-Yu Liang, S. Hofferberth, A. V. Gorshkov, T. Pohl, M. D. Lukin, and V. Vuletić, "Quantum nonlinear optics with single pho-

tons enabled by strongly interacting atoms", Nature **488**, 57 (2012).

[215] O. Firstenberg, T. Peyronel, Qi-Yu Liang, A. V. Gorshkov, M. D. Lukin, and V. Vuletić, "Attractive photons in a quantum nonlinear medium", Nature **502**, 71 (2013).

[216] P. Schauß, M. Cheneau, M. Endres, T. Fukuhara, S. Hild, A. Omran, T. Pohl, C. Gross, S. Kuhr, and I. Bloch, "Observation of spatially ordered structures in a two-dimensional Rydberg gas", Nature **491**, 87 (2012).

[217] M. Sich, D. N. Krizhanovskii, M. S. Skolnick, A. V. Gorbach, R. Hartley, D. V. Skryabin, E. A. Cerda-Méndez, K. Biermann, R. Hey, and P. V. Santos, "Observation of bright polariton solitons in a semiconductor microcavity", Nat. Photon. **6**, 50 (2012).

[218] T. C. H. Liew and V. Savona, "Single Photons from Coupled Quantum Modes", Phys. Rev. Lett. **104**, 183601 (2010).

[219] M. Wouters, "Resonant polariton-polariton scattering in semiconductor microcavities", Phys. Rev. B **76**, 045319 (2007).

[220] N. Takemura, S. Trebaol, M. Wouters, M. T. Portella-Oberli and B. Deveaud, "Polaritonic Feshbach resonance", Nature Phys. **10**, 500 (2014).

[221] T. Hahn, "CUBA multidimensional integrations", Computer Physics Communications **168**, 78 (2005).

[222] P. Pfeffer and W. Zawadzki, "Conduction electrons in GaAs: Five-level k· p theory and polaron effects", Phys. Rev. B **41**, 1561 (1990).

[223] C. Schindler and R. Zimmermann, "Analysis of the exciton-exciton interaction in semiconductor quantum wells", Phys. Rev. B **78**, 045313 (2008).

[224] M. Matuszewski, T. Taylor, and A. V. Kavokin, "Exciton Supersolidity in Hybrid Bose-Fermi Systems", Phys. Rev. Lett. **108**, 060401 (2012).

[225] G. Lemenager, F. Pisanello, J. Bloch, A. Kavokin, A. Amo, A. Lemaitre, E. Galopin, I. Sagnes, M. De Vittorio, E. Giacobino, and A. Bramati, "Two-photon injection of polaritons in semiconductor microstructures", Optics Letters, **39**, 307 (2014).

[226] T. Hanada, *"Basic Properties of ZnO, GaN, and Related Materials,"* in *Oxide and Nitride Semiconductors* 1, (T. Yao and S. Hong eds., Springer Berlin Heidelberg, 2009).

[227] J. Singh, *Physics of Semiconductors and Their Heterostructures* (McGraw-Hill, New York, 1993).

[228] A. Rubio-Ponce, D. Olguin and I. Hernandez-Calderon, "Calculation of the effective masses of II-VI semiconductor compounds", Superficies y Vacío 16, 26 (2003).

[229] A. Chernikov, T. C. Berkelbach, H. M. Hill, A. Rigosi, Y. Li, O. B. Aslan, D. R. Reichman, M. S. Hybertsen, and T. F. Heinz, "Exciton Binding Energy and Nonhydrogenic Rydberg Series in Monolayer WS_2", Phys. Rev. Lett. **113**, 076802 (2014).

[230] G. Berghauser and E. Malic, "Analytical approach to excitonic properties of MoS_2", Phys. Rev. B **89**, 125309 (2014).

[231] D. Y. Qiu, F. H. da Jornada, and St. G. Louie, "Optical Spectrum of MoS_2: Many-Body Effects and Diversity of Exciton States", Phys. Rev. Lett. **111**, 216805 (2013).

[232] T. Berkelbach, M. Hybertsen, and D. Reichman, "Theory of neutral and charged excitons in monolayer transition metal dichalcogenides", Phys. Rev. B **88**, 045318 (2013).

[233] K. S. Novoselov, A. Mishchenko, A. Carvalho, A. H. Castro Neto, "2D materials and van der Waals heterostructures", Science **353**, 9439 (2016).

[234] K. F. Mak, C. Lee, J. Hone, J. Shan, and T. F. Heinz, "Atomically Thin MoS_2: A New Direct-Gap Semiconductor", Phys. Rev. Lett. **105**, 136805 (2010).

[235] L. V. Keldysh, "Coulomb interaction in thin semiconductor and semimetal films", JETP Lett. **29**, 658 (1979).

[236] P. Cudazzo, I. V. Tokatly, and A. Rubio, "Dielectric screening in two-dimensional insulators: Implications for excitonic and impurity states in graphane", Phys. Rev. B **84**, 085406 (2011).

[237] W. Zhao, Z. Ghorannevis, L. Chu, M. Toh, C. Kloc, P.-H. Tan, and G. Eda, "Evolution of Electronic Structure in Atomically Thin Sheets of WS_2 and WSe_2", ACS Nano **7**, 791 (2013).

[238] K. He, N. Kumar, L. Zhao, Z. Wang, K. F. Mak, H. Zhao, and J. Shan, "Tightly Bound Excitons in Monolayer WSe_2", Phys. Rev. Lett. **113**, 026803 (2014).

[239] B. Zhu, X. Chen, and X. Cui, "Exciton Binding Energy of Monolayer WS_2", Sci. Rep. **5**, 9218 (2015).

[240] J. Shang, X. Shen, C. Cong, N. Peimyoo, B. Cao, M. Eginligil, and T. Yu, "Observation of Excitonic Fine Structure in a 2D Transition-Metal Dichalcogenide Semiconductor", ACS Nano **9**, 647 (2015).

[241] F. Ceballos, Q. Cui, M. Z. Bellus and H. Zhao, "Exciton formation in monolayer transition metal dichalcogenides", Nanoscale **8**, 11681 (2016).

[242] R. Schmidt, G. Berghauser, R. Schneider, M. Selig, P. Tonndorf, E. Malic, A. Knorr, S. M. de Vasconcellos, and R. Bratschitsch, "Ultrafast Coulomb-Induced Intervalley Coupling in Atomically Thin WS_2", Nano Lett. **16**, 2945 (2016).

[243] H.-P. Komsa and A. V. Krasheninnikov, "Effects of confinement and environment on the electronic structure and exciton binding energy of MoS_2 from first principles", Phys. Rev. B **86**, 241201(R) (2012).

[244] A. Ramasubramaniam, "Large excitonic effects in monolayers of molybdenum and tungsten dichalcogenides", Phys. Rev. B. **86**, 115409 (2012).

[245] T. Cheiwchanchamnangij and W. R. L. Lambrecht, "Quasiparticle band structure calculation of monolayer, bilayer, and bulk MoS_2", Phys. Rev. B. **85**, 205302 (2012).

[246] D. Y. Qiu, F. H. da Jornada, and S. G. Louie, "Optical Spectrum of MoS_2: Many-Body Effects and Diversity of Exciton States", Phys. Rev. Lett. **111**, 216805 (2013).

[247] H. Shi, H. Pan, Y.-W. Zhang, and B. I. Yakobson, Quasiparticle band structures and optical properties of strained monolayer MoS_2 and WS_2, Phys. Rev. B **87**, 155304 (2013).

[248] I. Kylanpaa and H.-P. Komsa, "Binding energies of exciton complexes in transition metal dichalcogenide monolayers and effect of dielectric environment", Phys. Rev. B **92**, 205418 (2015).

[249] D. Y. Qiu, F. H. da Jornada, and S. G. Louie, "Screening and many-body effects in two-dimensional crystals: Monolayer MoS_2", Phys. Rev. B **93**, 235435 (2016).

[250] F. A. Rasmussen and K. S. Thygesen, "Computational 2D Materials Database: Electronic Structure of Transition-Metal Dichalcogenides and Oxides", J. Phys. Chem. C **119**, 13169 (2015).

[251] A. Chernikov, T. C. Berkelbach, H. M. Hill, A. Rigosi, Y. Li, O. B. Aslan, D. R. Reichman, M. S. Hybertsen, and T. F. Heinz, "Exciton Binding Energy and Nonhydrogenic Rydberg Series in Monolayer WS_2", Phys. Rev. Lett. **113**, 076802 (2014).

[252] J. R. Schaibley, T. Karin, H. Yu, J. S. Ross, P. Rivera, A. M. Jones, M. E. Scott, J. Yan, D. G. Mandrus, W. Yao, K.-M. Fu, and X. Xu, "Population Pulsation Resonances of Excitons in Monolayer $MoSe_2$ with Sub-1 μeV Linewidths", Phys. Rev. Lett. **114**, 137402 (2015).

[253] C. Robert, D. Lagarde, F. Cadiz, G. Wang, B. Lassagne, T. Amand, A. Balocchi, P. Renucci, S. Tongay, B. Urbaszek, and X. Marie, "Exciton radiative lifetime in transition metal dichalcogenide monolayers", Phys. Rev. B **93**, 205423 (2016).

[254] M. Selig, G. Berghauser, A. Raja, P. Nagler, C. Schuller, T. F. Heinz, T. Korn, A. Chernikov, E. Malic and A. Knorr, "Excitonic linewidth and coherence lifetime in monolayer transition metal dichalcogenides", Nat. Comm. **7**, 13279 (2016).

[255] A. Chernikov, A. M. van der Zande, H. M. Hill, A. F. Rigosi, A. Velauthapillai, J. Hone, and T. F. Heinz, "Electrical Tuning of Exciton Binding Energies in Monolayer WS_2", Phys. Rev. Lett. **115**, 126802 (2015).

[256] B. Scharf, T. Frank, M. Gmitra, J. Fabian, I. Zutic, and V. Perebeinos, "Excitonic Stark effect in MoS_2 monolayers", Phys. Rev. B **94**, 245434 (2016).

[257] Y. You, X.-X. Zhang, T. C. Berkelbach, M. S. Hybertsen, D. R. Reichman, and T. F. Heinz, "Observation of biexcitons in monolayer WSe_2", Nature Physics **11**, 477 (2015).

[258] D. K. Zhang, D. W. Kidd, and K. Varga, "Excited Biexcitons in Transition Metal Dichalcogenides", Nano Lett. **15**, 7002 (2015).

[259] E. J. Sie, A. J. Frenzel, Y.-H. Lee, J. Kong, and N. Gedik, "Intervalley biexcitons and many-body effects in monolayer MoS_2", Phys. Rev. B **92**, 125417 (2015).

[260] G. Plechinger, P. Nagler, A. Arora, R. Schmidt, A. Chernikov, A. G. del Aguila, P. C. M. Christianen, R. Bratschitsch, C. Schuller, and T. Korn, "Trion fine structure and coupled spin–valley dynamics in monolayer tungsten disulfide", Nat. Comm. **7**, 2715 (2016).

[261] F. Ceballos, M. Z. Bellus, H.-Y. Chiu, and H. Zhao, "Ultrafast Charge Separation and Indirect Exciton Formation in a MoS_2-$MoSe_2$ van der Waals Heterostructure", ACS Nano **8**, 12717 (2014).

[262] P. Rivera, J. R. Schaibley, A. M. Jones, J. S. Ross, S. Wu, G. Aivazian, P. Klement, K. Seyler, G. Clark, N. J. Ghimire, J. Yan, D. G. Mandrus, W. Yao, and X. Xu, "Observation of long-lived interlayer excitons in monolayer $MoSe_2$ – WSe_2 heterostructures", Nat. Comm. **6**, 6242 (2015).

[263] E. V. Calman, C. J. Dorow, M. M. Fogler, L. V. Butov, S. Hu, A. Mishchenko,

and A. K. Geim, "Control of excitons in multi-layer van der Waals heterostructures", Appl. Phys. Lett.**108**, 101901 (2016).

[264] M. Sidler, P. Back, O. Cotlet, A. Srivastava, T. Fink, M. Kroner, E. Demler, and A. Imamoglu, "Fermi polaron-polaritons in charge-tunable atomically thin semiconductors", Nature Phys. **13**, 255 (2017).

[265] S. Dufferwiel, S. Schwarz, F. Withers, A. A. P. Trichet, F. Li, M. Sich, O. Del Pozo-Zamudio, C. Clark, A. Nalitov, D. D. Solnyshkov, G. Malpuech, K. S. Novoselov, J. M. Smith, M. S. Skolnick, D. N. Krizhanovskii, and A. I. Tartakovskii, "Exciton–polaritons in van der Waals heterostructures embedded in tunable microcavities", Nature Comm. **6**, 8579 (2015).

[266] N. Lundt, S. Klembt, E. Cherotchenko, S. Betzold, O. Iff, A. V. Nalitov, M. Klaas, C. P. Dietrich, A. V. Kavokin, S. Höfling, and C. Schneider, "Room-temperature Tamm-plasmon exciton-polaritons with a WSe_2 monolayer", Nature Comm. **7**, 13328 (2016).

[267] N. Lundt, A. Marynski, E. Cherotchenko, A. Pant, X. Fan, S. Tongay, G. Sek, A. V. Kavokin, S. Höfling, and C. Schneider, "Monolayered $MoSe_2$: a candidate for room temperature polaritonics", 2D Materials **4**, 015006 (2017).

[268] G. Wang, X. Marie, B. L. Liu, T. Amand, C. Robert, F. Cadiz, P. Renucci, and B. Urbaszek, "Control of Exciton Valley Coherence in Transition Metal Dichalcogenide Monolayers", Phys. Rev. Lett. **117**, 187401 (2016).

[269] M. M. Glazov, L. E. Golub, G. Wang, X. Marie, T. Amand, and B. Urbaszek, "Intrinsic exciton-state mixing and nonlinear optical properties in transition metal dichalcogenide monolayers", Phys. Rev. B **95**, 035311 (2017).

[270] S. Sim, J. Park, J.-G. Song, C. In, Y.-S. Lee, H. Kim, and H. Choi, "Exciton dynamics in atomically thin MoS_2: Interexcitonic interaction and broadening kinetics", Phys. Rev. B **88**, 075434 (2013).

[271] N. Kumar, Q. Cui, F. Ceballos, D. He, Y. Wang, and H. Zhao, "Exciton-exciton annihilation in $MoSe_2$ monolayers", Phys. Rev. B **89**, 125427 (2014).

[272] A. Chernikov, C. Ruppert, H. M. Hill, A. F. Rigosi, and T. F. Heinz, "Population inversion and giant bandgap renormalization in atomically thin WS_2 layers", Nature Photonics **9**, 466 (2015).

[273] G. Aivazian, H. Yu, S. Wu, J. Yan, D. G. Mandrus, D. Cobden, W. Yao and X. Xu, "Many-body effects in nonlinear optical responses of 2D layered semiconductors", 2D Mater. **4**, 025024 (2017).

[274] G. Ramon, A. Mann, and E. Cohen, "Theory of neutral and charged exciton scattering with electrons in semiconductor quantum wells", Phys. Rev. B **67**, 045323 (2003).